Modeling the catalyst selectivity in the ethylene epoxidation reaction

A first principles study

Thesis submitted for the degree of

Doctor Philosophiæ

Candidate:
Paola Gava

Supervisors:
Prof. Stefano de Gironcoli
Dr. Anton Kokalj

October 2007

Contents

List of Tables

List of Figures

Introduction

The work presented in this thesis belongs to the research field of heterogeneous catalysis, investigated using ab-initio methods. The term catalysis refers to chemical reactions where an increase in the reaction rate is induced by the presence of a material, called catalyst, that is chemically unchanged at the end of the reaction. Heterogeneous means that catalyst and reactants are in different phases. Transition metal surfaces are among the most used catalyst in heterogeneous catalysis. For instance, the earliest commercial catalytic processes have been the ammonia synthesis from nitrogen and hydrogen catalysed by iron (Haber process), and the synthesis of hydrocarbons and their oxygen derivatives, from hydrogen and carbon monoxide, catalysed by iron and cobalt (Fischer-Tropsch synthesis). Heterogeneous catalysis is one of the major field of research in chemistry and physics, and it is also fundamental in the modern chemical industry, where the production of the most important chemicals involves catalysis.

In this work we investigate the ethylene epoxidation. Ethylene is the simplest alkene, with chemical formula C_2H_4, and it is produced in the petrochemical industry, from heavier hydrocarbons [1, 2]. In the epoxidation of ethylene, an oxygen atom is added to the molecule so as to bind with both C atoms, thus forming a ring structure. The ethylene epoxide is an important chemical, widely used in the production of plastics, and it is catalysed by silver, supported on oxides, at high temperature and pressure conditions [1, 2].

Usually, during catalytic processes, other competing reactions can take place, and therefore reactants are converted into undesired products and wasted. In the case of ethylene epoxidation, the main undesired product is acetaldehyde, leading to total combustion. The ratio between desired products and the consumed reactants is called selectivity, and it is an important

parameter which determines the quality of a catalyst in a specific chemical reaction. Silver catalysts, in presence of Cs and Cl promoters, show a selectivity toward ethylene epoxide formation up to 80% [1, 2]. Even if, from the industrial point of view, a high level of selectivity is obtained, the ethylene epoxidation reaction still attracts a lot of attention from both experimental and theoretical point of view, since the factors which determine catalyst selectivity are poorly understood. Moreover, a deeper understanding in the reaction mechanisms leading to the desired ethylene epoxide rather than to combustion products, would help to design better catalysts, and thus to improve the control on this reaction, reducing reactants waste, production costs and environmental impact.

In the study of heterogeneous catalysis, surface science experiments performed under Ultra High Vacuum conditions provide important information. In particular, these techniques allow to investigate the surface structure of the catalyst, to identify stable intermediates, formed during the overall reaction, and to measure the amount of different final products. Nevertheless, direct control of the elementary steps involved in the overall reaction, and of the mechanisms operating at atomic level is very difficult. For instance, in order for an activated elementary step to occur, the system has to overcome an energy barrier, that corresponds to pass through an unstable configuration, called transition state. According to the van't Hoff-Arrhenius law, the temperature dependence of the reaction rate is mainly determined by this energy barrier. Therefore, the identification of the transition state is an important task to understand the reaction mechanism. Since the transition state has too short life time, its experimental observation is very difficult.

In the last twenty years, numerical simulations have achieved important progresses in the modelling of matter at atomistic level. In particular, with the introduction of Density Functional Theory (DFT) [3, 4] to investigate the electronic properties of matter, together with the increase of computer resources, numerical simulations have become a useful tool to investigate complex systems, and to provide detailed data, which can be compared with experimental results. Moreover, with numerical simulations one can calculate physical properties, which are inaccessible to experiments. In other terms, numerical simulations provide complementary and additional informations to

those obtained from experiments. For instance, in the case of catalysis, from ab-initio simulations one can get in principle a picture of the full reaction pathway, and identify transition states. Therefore the interplay between experimental and computational results is very important for the study of heterogeneous catalysis. Nevertheless, it is worth to notice that a direct comparison between ab-initio simulations, surface science experiments and industrial reactions is not easy. Indeed the latter occur at high pressure, while surface science experiments are performed under UHV, and DFT calculations usually deal with highly ordered model structures, which are different from systems under realistic conditions.

In this work, the ethylene epoxidation on different transition metal surfaces has been systematically studied, by means of ab-initio methods, based on DFT. In particular, the main purpose has been to understand the mechanisms operating at atomic level, which determine the catalysts selectivity. Catalysts have been modeled by well defined metal surfaces of low Miller indices. Although real catalysts under industrial conditions are not perfect low index surfaces [5, 6, 7, 8], we have focused here on model catalysts, which allow us to gain understanding and insight into the fundamental factors that govern the catalyst selectivity at atomic scale, with reasonable computational effort.

In chapter 1, a description of heterogenous catalysis at metal surfaces is presented. In particular, basic concepts and principles, that are often used to investigate chemical reactions, are discussed. Moreover, a description of the ethylene epoxidation reaction is presented, to introduce in detail the problem we have addressed. The most important theoretical and experimental findings are reviewed.

In chapter 2, theoretical concepts used in this work are introduced. In particular, Density Functional Theory, the use of plane waves to represent the electronic wavefunctions and density, and the pseudopotential method to deal with core electrons, are discussed. A description of chemical reactions, which are thermally activated processes that involve overcoming an energy barrier, is presented. Moreover, the algorithm used to identify transition states is described.

In chapter 3, our results on ethylene epoxide and acetaldehyde forma-

tions from a common intermediate state, called OxaMetallaCycle (OMC), are collected. In particular, structural parameters of reactants, transition states and products on Ag, Cu, Au and Rh, (100) and (111) surfaces, are reported, together with activation energies. From the analysis of our data, some conclusions are drawn about why silver is a special catalyst for the ethylene epoxidation reaction.

In chapter 4, the basic principles described in chapter 2 are applied to ethylene epoxide and acetaldehyde formation from OMC. This does not give a sufficiently accurate description of the reactions, therefore a more detailed analysis of the structural characteristics of transition states leading to both products is performed. This analysis allows us to understand new important factors which characterize the two reaction pathways, and to find a simple quantity that correlates very well with selectivity. On the basis of our findings, we are able to explain why Cu and Ag/Cu alloys display higher selectivity toward EO with respect to pure Ag.

Finally, since Cl is a well known promoter in the ethylene epoxidation reaction, in chapter 5 the adsorption of Cl on Ag surfaces is investigated. In particular, Cl is often assumed to adsorb subsurface on Ag, and its role as promoter in the ethylene epoxidation has been also explained on the basis of this assumption. Nevertheless, theoretical studies on the subject mainly deal with on-surface Cl adsorption. Therefore we addressed the feasibility of Cl to move below the Ag surface. Our findings suggest that the role of subsurface Cl as promoter in the ethylene epoxidation has to be revised.

Chapter 1

Heterogeneous catalysis at metal surfaces

In this chapter a general description of heterogenous catalysis at metal surfaces is given. Chemical reactions are fully characterized by the shape of the Potential Energy Surface (PES), but since the knowledge of the whole PES is unfeasible, simple concepts and principles are usually used to understand the main properties of the reactions. In this chapter, the Hammer-Norskov chemisorption model, the Sabatier principle, the Hammond postulate and the Brønsted-Evans-Polanyi (BEP) principle are briefly described.

A detailed introduction to the ethylene epoxidation reaction is also presented, describing the most important findings from both theoretical and experimental point of view.

1.1 General description and basic principles

Heterogeneous catalisys is the term used to refer to catalitically activated chemical reactions, where the catalyst is in a different phase with respect to reactants. In this work we consider a chemical reaction, the ethylene epoxidation, where catalysts are metal surfaces, and reactants are in the gas-phase. Overall heterogeneous catalytic reaction is composed of several elementary steps, which are the adsorption of reactants on the surface, diffusion on the surface, reaction steps involving bond breaking and bond making, so as to

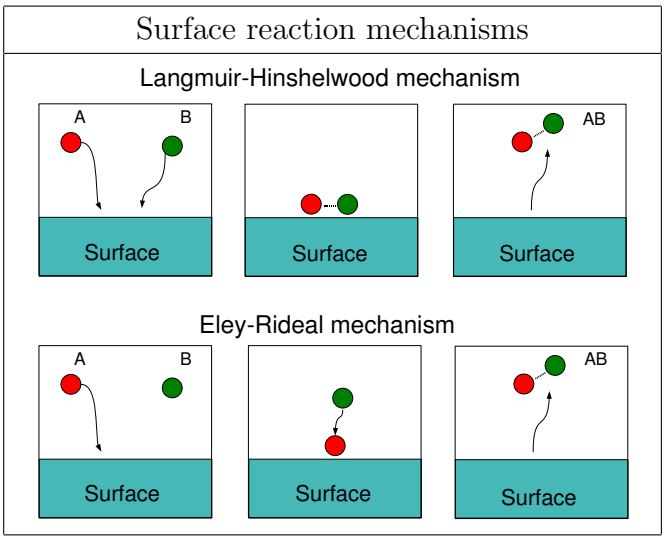

Figure 1.1: *Schematic representation of surface reaction mechanisms: Langmuir-Hinshelwood, where both molecules are adsorbed on the surface and then they undergo a chemical reaction, and Eley-Rideal, where only one molecule is adsorbed on the surface and the other one reacts directly with it, without adsorbing.*

form product molecules, and final desorption of products.

In Fig. 1.1 two kinds of mechanism through which surface reactions can proceed are schematically represented: the Langmuir-Hinshelwood (LH) and the Eley-Rideal (ER) mechanism. In the former case, both molecules are adsorbed on the surface and then they react to form products. A typical example of chemical reaction which proceeds through a LH mechanism is the carbon monoxide oxidation to form carbon dioxide on platinum catalysts. In the ER case, only one molecule is adsorbed on the surface and the other one reacts directly with it, without adsorbing. The reaction of ammonia with pre-adsordeb oxygen on platinum catalyst to form nitrogen gas is an example of reaction proceeding through an ER mechanism.

The interaction between reactants and surface can be described in terms of the electronic levels of the adsorbate and the valence states of the metal surface [9]. The typical density of states of d-metals (which have been considered in this work) shows a localized d band around the Fermi level (ϵ_{F}) and a more extended s band. From a tight binding model, it can be shown

that the band-width is proportional to the hopping integrals between nearest neighbour orbitals. The *d* bands show a small band-width, because atomic *d* states are localized and the hopping integral is small, while the contrary happens for *s* band. Therefore, metal *d* band can be approximatively considered as a molecular state and it interacts with the adsorbate, forming bonding and antibonding states. If the antibonding states of the surface-adsorbate system are empty (above ϵ_{F}) the molecule is strongly bound to the surface, while the more they are occupied (below ϵ_{F}) the more the molecule-surface interaction is destabilized. The term chemisorption is used to refer to strong interaction between surface and adsorbates, such as the covalent bond described above, where hybridization is present between adsorbates and surface states. Another possible mode of strong molecule-structure interaction may involve ionic bonds. The term physisorption is instead used to refer to a weaker interaction, dermined by dispersion forces.

The adsorption energy of reactants is an important quantity to characterize the catalytic properties of a metal surface. For instance, in dissociation reactions of diatomic molecules, such as O_2, enhancing the binding between dissociated atoms and the surface, would make the reaction easier. In particular, the more reactive is a surface the stronger is the bond with adsorbates. Therefore, it would be useful to find a quantity correlating with reactivity.

The interaction between adsorbates and transition metal surfaces is mainly determined by *d* bands of the metal, while the effect due to the interaction with *s* band is weak and can be assumed to be similar for different transition metals. As for the *d* band, an important parameter is the center of the *d* band, ϵ_{d}. In particular, the more ϵ_{d} is below ϵ_{F}, the more the antibonding states will be below ϵ_{F} and therefore occupied, and the more the interaction will be weak, and vice-versa. This is the so-called *Hammer-Norskov* chemisorption model, which states that the more ϵ_{d} is below ϵ_{F}, the less reactive will be the metal [10]. In Fig. 1.2 the reactivity behaviour of late transition metals is schematically represented. In general, going from left to right in the periodic table, the reactivity decreases for transition metals, because *d* bands are more and more filled, and they move below ϵ_{F}. Again, going from the top to the bottom of the periodic table, ϵ_{d} moves downward ϵ_{F}, and reactivity decreases. In the Hammer-Norskov model, reactivity is also described by

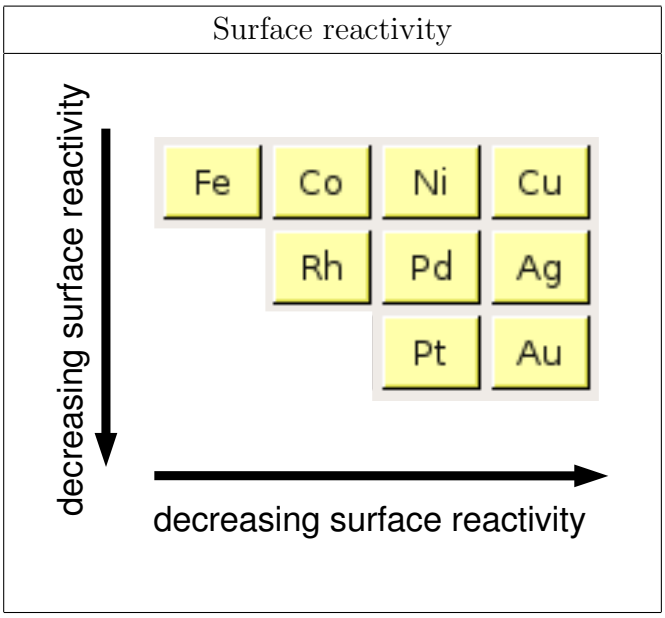

Figure 1.2: *Reactivity behaviour of late transition metals. Going form left to right, and from top to bottom in the periodic table, the reactivity decreases.*

a second parameter, proportional to the square of the coupling matrix elements between adsorbate state and metal d band, V_{ad}^2. This term accounts for the energy cost required for the orthogonalization of the adsorbate states to those of the metal. In the comparison between Ag and Au, d bands are fully occupied and changes in the position of ϵ_{d} have not significant effect on the reactivity, while the lower reactivity of Au is determined by V_{ad}^2. Indeed $5d$ orbitals are more extended than $3d$ and $4d$, and V_{ad}^2 is larger.

The reactivity of a specific metal can be modified in different ways [9]. For instance, variations of the lattice parameter (strain) can be used to affect the electronic properties of the metal. Indeed, increasing the interatomic distance, the overlap between d states decreases, and their bandwidth accordingly. In order to keep constant the occupation of d band, ϵ_{d} moves up toward the Fermi level, and the metal reactivity is improved. The contrary happens when the lattice parameter is decreased. Moreover, the presence of surface defects, such as steps and adatoms, usually enhances the surface reactivity. Indeed, atoms forming steps and adatoms are less coordinated than surface ones. Low coordination corresponds to narrower d band, and ϵ_{d} closer to the

Fermi level.

Finally, the pre-adsorption of adsorbates on the surface may have the effect to block available adsorption sites for reactants, reducing the reactivity of the surface. Furthermore, the pre-adsorption of electronegative species can reduce the surface reactivity towards electronegative reactants, due to lateral electrostatic repulsion. On the contrary, the adsorption of electropositive species can improve the surface reactivity towards electronegative reactants, due to attractive dipole-dipole interaction.

Beside the reactivity, other important quantities to characterize a catalyst, are the activity and selectivity: the activity is defined as the percentage of reactants consumed during the reaction, while the selectivity is the percentage of consumed reactants trasformed into the desired product. The relation between reactivity, activity and selectivity is not trivial. For instance, if the interaction between catalyst and adsorbates is very strong (high reactivity), reactants would be easily decomposed in their constituents. However, also constituents would strongly interact with the surface and too much energy would be necessary to break the surface-constituents bonds, to form the desired products, and the catalyst would be poisoned (low activity). On the other side, if the interaction between catalyst and adsorbates is very weak (low reactivity), the catalyst results to be inactive in breaking bonds in reactants and the reaction cannot proceed (low activity). Futhermore, the properties of a metal surface as catalyst for an overall chemical reaction are not simply determined by its interaction with reactants and products, but also with all the intermediates formed during each elementary reaction step.

Usually the best catalyst obeys the so-called *Sabatier principle*, which states that the active sites on the surface must bind the reactants, products and key reaction intermediates with modest strenght. As a consequence of the Sabatier principle, the catalytic activity of a surface for a given elemetary reaction step usually follows the so-called *volcano curve* through the periodic table, as shown in Fig. 1.3.

A detailed description of chemical reactions and thermally activated processes is given in section 2.4. Here we anticipate that an elementary reaction step can be described as a transition between an initial state (IS) and final state (FS). Along the reaction pathway, which connects IS to FS, the con-

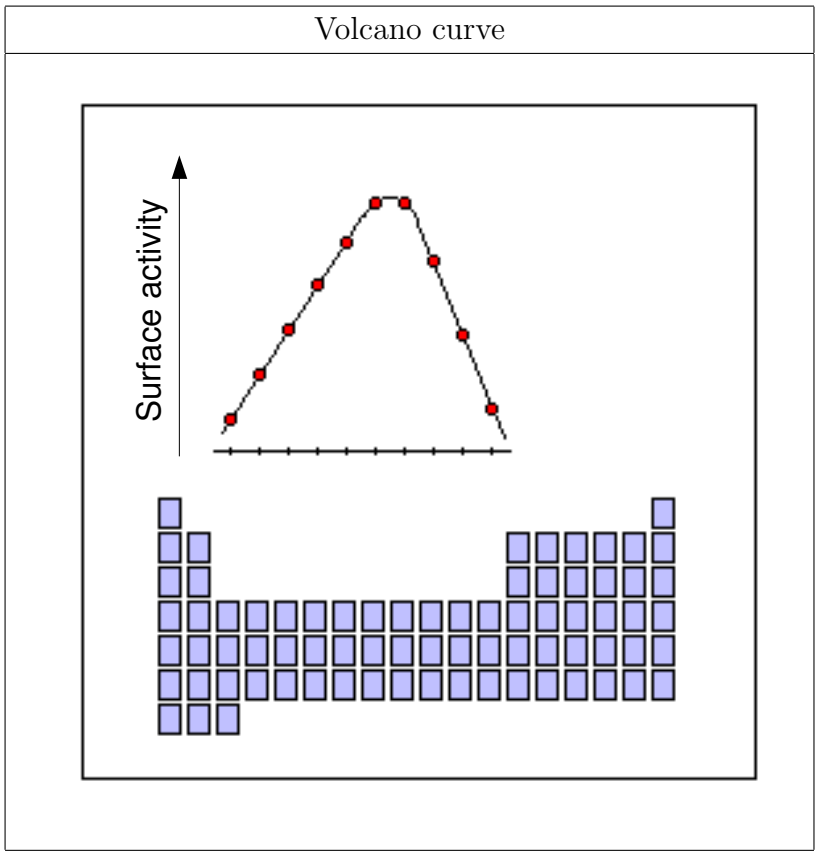

Figure 1.3: *Schematic representation of the Sabatier principle: the best catalyst for a given chemical reaction has active sites on the surface that bind reactants, products and key reaction intermediates with modest strenght. Since the transition metal reactivity decreases going from left to right in the periodic table, the catalytic activity follows the so-called volcano curve through the periodic table. The actual position of the volcano peak depends on the specific reaction.*

figuration with highest energy is called transition state (TS), and the energy difference between TS and IS is called activation energy (E^*). The TS plays an important role since the rate of the elementary reaction step depends exponentially on E^*. In particular, the smaller is the activation energy, the larger is the rate of a reaction. Transition states are usually classified in two types: early transition state (ETS) and late transition state (LTS). In the former case, the TS structure is similar to that of reactants, while in the latter

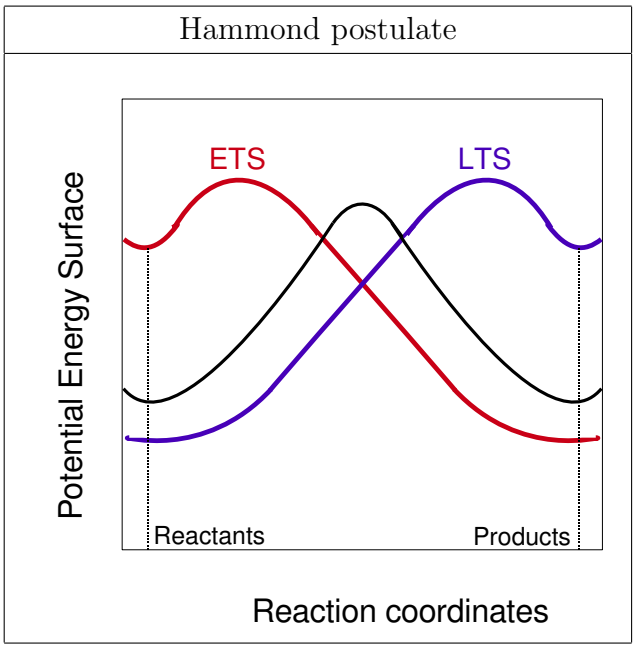

Figure 1.4: *Schematic representation of Hammond postulate: in highly exothermic reactions (red line) TS is similar to reactants (early TS), while on highly endothermic reactions (blue line) TS is similar to products (late TS). In athermic reaction (black line) TS is in between reactants and products.*

case it is similar to that of products. An indication of the reaction pathway profile and the typology of TS is given by the *Hammond* postulate [11], which states that:

if two states, for example, a transition state and an unstable intermediate, occur consecutively during a reaction process and have nearly the same energy content, their interconversion will involve only a small reorganization of the molecular structures.

The interpretation of this postulate is schematically represented in Fig. 1.4: in highly exothermic reactions TS should rensemble the reactants (ETS), while in highly endothermic reactions TS should rensemble the products (LTS). In athermic reactions, TS is in between reactants and products. As a consequence of Hammond postulate, one can guess the typology of the TS in a specific reaction step, and act on the energy of TS, modifying the adsorption of reactants and products on the surface.

Finally, it is worth to mention the *Brønsted-Evans-Polanyi (BEP)* prin-

ciple, which states that a linear relation between activation energy and enthalpy of reaction (ΔH_{r}) is sometimes observed within a series of closely related reactions:

$$E^* = a + b\Delta H_r. \tag{1.1}$$

The BEP relation is usefull, for example, when a systematic study of a given chemical reaction is performed under different environment conditions.

The concepts presented in this section represent the basic theoretical instruments people usually uses to investigate catalytic chemical reactions, and in some cases they provide satisfactory descriptions. In more complex reactions, where several molecular bonds have to be broken and formed in order for the reaction to occur, deviation from these standard principles and postulates are expected. In that case, a more detailed study is required and other important factors have to be identified to accurately describe the chemical reaction.

1.2 The ethylene epoxidation reaction: state of the art

The ethylene epoxidation reaction is one of the most important selective oxidation process based on heterogeneous metallic catalysis, together with methanol convertion into formaldehyde. The ethylene epoxide (EO) is an important chemical, used as intermediate in the production of glycols and other plastics, and it has an estimated world production of over 10^7 t per year [1]. The EO synthesis from ethylene and oxygen on silver catalysts has been discovered on 1931, and it is performed at a temperature of 500–600 K and a pressure of 1–2 MPa, on oxide supported Ag catalysts [1, 2].

Indeed silver displays unique catalytic properties in the selective oxidation of ethylene to EO, and Ag unpromoted surfaces have an initial selectivity toward EO of around 40%. The main undesired product is CO_2, resulting from total combustion. Significant progress has been achieved to explain the uniqueness of silver as a catalyst for the ethylene epoxidation. In particular, the initial selectivity of the reaction is determined by the bond strenght of oxygen adsorbed on the metal surface, and the weak ability of the catalyst

to activate the C–H bond in the ethylene. The latter factor disfavors the use of more reactive transition metals as catalysts, since they are known to activate C–H bonds.

As for the oxygen, the nature and role of various O species adsorbed on Ag surfaces has been for long time debated. In particular, O can adsorb in four different states: molecular, nucleophilic atomic, electrophilic atomic, and subsurface atomic. It is however commonly believed that electrophilic atomic oxygen takes part in the ethylene epoxidation reaction, while nucleophilic atomic oxygen is responsible for C–H bond activation [12, 13]. Therefore oxygen has to adsorb dissociatively on the surface, but the resulting O–surface bond should be not so strong that the epoxidation is excluded for thermodynamic reasons. In that respect, silver is unique since oxygen can adsorb dissociatively on it and, depending on the O coverage, it can contain weakly bound O atoms. Also atomic oxygen adsorbed subsurface seems to be an important species in this reaction, but its role is controversial. In particular, earlier theoretical calculations predict that the presence of subsurface oxygen atoms reduces the bond energy between on-surface oxygen atoms and Ag surface [14]. This fact leads to more electrophilic on-surface oxygen atoms and enhances the interaction between them and adsorbed ethylene, thus making the insertion of O into the double bond of ethylene easier. At variance, more recent theoretical studies show that the presence of subsurface oxygen instead stabilizes on-surface oxygen [15, 16], and it considerably increases the chemisorption energy of the ethylene on Ag surface [17, 18].

It is worth to mention that establishing the relationship between the surface geometry of a catalyst and its catalytic performance is not trivial, since usually surface science experiments (such as XPS, Raman spectroscopy, LEED, STM[1]) focused on the analysis of the chemical composition and struc-

[1] *XPS*: X-ray Photoemission Spectroscopy. It is used to identify molecules adsorbed on a surface. The surface is exposed to an X-ray beam which induces a photoelectric ionization of the atoms. The energies of photoelectrons are characteristic of their original electronic states in the specific atom, and measuring energies it is possible to determine the species present on the surface. *Raman spectroscopy*: in this case a laser beam in the visible light is used, which interacts with phonons or other excitations in the system. The result is an energy shift of the laser photons, which gives information about the excitation modes of the system. *LEED*: Low Energy Electron Diffraction. It is used to determine the

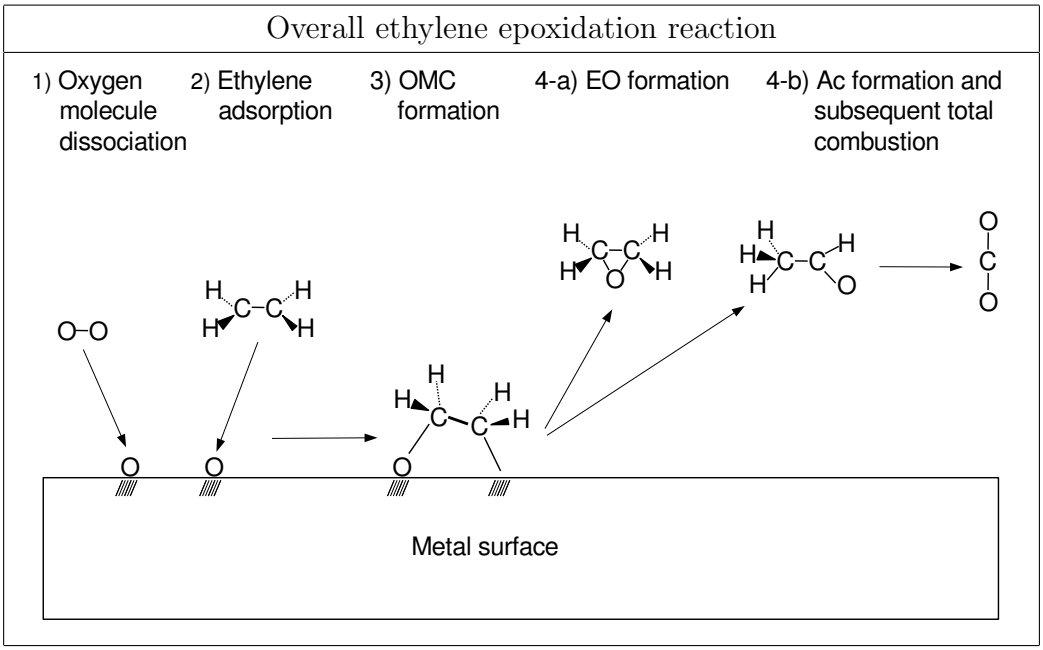

Figure 1.5: *Schematic representation of the elementary steps in the overall ethylene epoxidation reaction.*

ture of the catalyst, are performed not in presence of the gas mixture, but under Ultra High Vacuum (UHV) conditions. This fact leads to the so-called pressure gap problem in comparing UHV experiments with those obtained at high pressure conditions. There is, however, a growing evidence that ultra-thin oxide overlayers, may play an important role in the reactivity of metal catalysts under ordinary industrial conditions [5, 6, 7, 8].

The overall ethylene epoxidation reaction is schematically represented in Fig. 1.5. The elementary steps are the dissociative adsorption of oxygen, the ethylene adsorption, and an OxaMetallaCycle (OMC) intermediate formation, which then transforms either to EO or acetaldehyde (Ac), being the Ac formation the path leading to the undesired total combustion. The rate

surface structure. The surface is exposed to an electron beam, and elastically-scattered electrons contribute to the diffraction pattern. An analysis of the diffraction pattern show a symmetry in the spot positions, which reflects that of the surface. *STM*: Scanning Tunneling Microscope. It is used to direct access the atomic structure of the surface. An electrical probe is located over the surface, to detect a weak-tunneling current flowing between the tip and the surface, which is proportional to the distance between them.

limiting steps of the overall reaction are the O_2 dissociation and the recently discovered OMC formation (steps 1 and 3), while the selectivity is determined by the EO formation with respect to Ac formation (step 4).

The presence of an OMC as intermediate structure in the epoxidation of alkenes has been widely investigated, from both experimental and theoretical point of view [19, 20, 21, 22]. Experimental results on the OMC structure are obtained under UHV conditions, usually combining TPD and HREELS techniques[2], and comparison with theoretical calculations is often required to interpret these data. In particular, higher alkenes adsorb on metal surface sufficiently strongly to form, when increasing the temperature, the OMC structure, which then reacts to form the epoxide and other products. As concern the ethylene epoxidation reaction, the OMC structure on Ag surfaces have been characterized by several theoretical studies [23, 24, 25, 26, 27]. Experimentally, the UHV situation is complicated since ethylene adsorbs weakly on Ag surfaces, and this fact makes temperature-programmed experiments difficult, because the molecule desorbs before it can react to form the OMC. Instead, the OMC structure has been observed dosing EO on Ag surface [28, 29]. When EO is adsorbed on the silver surface at suffciently high temperature (around 250 K), the ring opening of EO is activated and a stable OMC is observed. A theoretical study of EO formation from an OMC intermediate predicted a similar selectivity toward EO, as reported for unpromoted Ag catalyst [25].

The use of alkalis and halogens as promoters in the epoxidation of hydrocarbons is widely used, and in the ethylene epoxidation, a significant increase, up to 80%, in selectivity toward EO formation is gained in presence of Cs and Cl atoms [1, 2, 30]. Various roles have been suggested for both species in the ethylene epoxidation. As for Cs, a recent theoretical study shows that Cs acts via dipole-dipole interaction to stabilize the TS for the formation of

[2] *TPD*: Temperature Programmed Desorption. It involves heating a sample, under UHV condition. As the temperature rises, surface reaction are activated and some adsorbed species can have enough energy to escape. Desorbed species are then detected by means of mass spectroscopy. *HREELS*: High Resolution Electron Energy Loss Spectroscopy. An electron beem incident on the surface loses energy by exciting atomic and molecular vibrations at the surface. The out-going beam shows energy loss peaks, which give information on the excited vibrations.

the epoxide, with respect to TS leading to undesired total combustion [31].

As for Cl, its influence as promoter in the ethylene epoxidation has been intensively studied, but its role still remains controversial. In industrial conditions chlorinated hydrocarbons are added to the reactant gas mixture. Experiments, performed adsorbing atomic Cl on Ag surfaces, show that selectivity toward EO increases even at low Cl coverage, while catalyst activity decreases up to zero at high Cl coverage, due to blocking of active surface sites by Cl atoms [1, 30]. The increase of selectivity has been explained in terms of competition between Cl and O atoms for metal electrons, where Cl destabilizes adsorbed electrophilic O, favoring the EO formation. Moreover, Cl is believed to adsorb subsurface, and its ability to improve selectivity has been also explained in terms of Cl replacement of the role of subsurface O atoms [2]. Finally, in a recent computational work it is suggested that Cl acts as Cs, stabilizing via dipole-dipole interaction the TS leading to EO, provided it is adsorbed subsurface [31].

Due to its importance in epoxidation reactions, Cl interaction with Ag surfaces has been studied by computer simulations and experiments. However, the computational studies deal mainly with on-surface Cl adsorption [32, 33], while experimental works have investigated both on-surface Cl adsorption [34, 35], and Cl diffusion into Ag bulk [36, 37, 38]. These experiments suggest that Cl diffusion beneath the surface and surface restructuring occur at Cl coverages in the monolayer and sub-monolayer regime, and at temperature relevant in the epoxidation processes.

Finally, recent theoretical and experimental results have suggested that Cu catalysts could be more selective than Ag in the epoxidation of higher alkenes [39, 40, 41, 42]. Also for the ethylene epoxidation, theoretical studies have shown that Cu displays higher selectivity toward EO than Ag [43, 44]. In particular, the EO formation from the OMC on Cu results to be an endothermic process while Ac formation is exothermic, requiring a short contact times to limit the decomposition of EO product. Theoretical and experimental studies have shown that also Ag/Cu alloys, with low concentration of Cu, are more selective than silver [45, 46, 47]. The higher selectivity of Cu with respect to Ag in the ethylene epoxidation has been attributed to the stronger OMC–surface interaction in copper catalyst [43].

As a conclusion of this introduction to the state of the art in the ethylene epoxidation rection, it is worth to notice that in spite of the many computational and experimental studies on the subject, where the reaction mechanism of the OMC conversion into EO and Ac has been characterized in detail, the specific surface factors which determine the selectivity of a catalyst toward EO formation remain understood to a lesser extent.

Chapter 2

Ab-initio methods for studying chemical reactions

In this chapter theoretical concepts which are the basis of ab-initio methods, used to study catalytic processes, are introduced. In particular, all quantities which allow to identify and characterize catalysts, reactants, products and the reaction pathways have been calculated in this work on the basis of Density Functional Theory, as implemented in the Quantum Espresso package.

Therefore, in this chapter the basic ideas of Born-Oppenheimer approximation and DFT are presented, together with the use of plane waves to represent electron wavefunctions and density, and ultrasoft pseudopotentials techniques needed to deal with core electrons. Finally, a description of thermally activated processes and Nudged Elastic Band (NEB) method, used to identify reaction pathways, is presented.

2.1 Born-Oppenheimer approximation

The study of a physical system made of M ions and N electrons requires the solution of the Schrödinger equation:

$$H\Psi = W\Psi, \tag{2.1}$$

with:

$$\begin{aligned} H &= \sum_{i=1}^{N} -\frac{\hbar^2}{2m_e}\nabla^2_{\mathbf{r}_i} + \sum_{j=1}^{M} -\frac{\hbar^2}{2M_j}\nabla^2_{\mathbf{R}_j} + \\ &- \sum_{i=1}^{N}\sum_{j=1}^{M} \frac{e^2 Z_j}{|\mathbf{r}_i - \mathbf{R}_j|} + \sum_{i<j} \frac{e^2}{r_{ij}} + \sum_{i<j} \frac{e^2 Z_i Z_j}{R_{ij}}, \end{aligned} \tag{2.2}$$

where W and Ψ are the total energy and the eigenstate of the full system, respectively, m_e and M_j are the electronic and ionic masses, $-e$ and eZ_j are the electronic and ionic charges, $\mathbf{r}_i$ $(i = 1, ..., N)$ and $\mathbf{R}_j$ $(j = 1, ..., M)$ are the electronic and ionic coordinates, and $R_{ij} = |\mathbf{R}_i - \mathbf{R}_j|$ and $r_{ij} = |\mathbf{r}_i - \mathbf{r}_j|$. The first two terms in eq. (2.2) are the electronic and ionic kinetic energies, respectively, while the other terms represent the electrostatic interaction between electrons and ions, electrons and electrons, and ions and ions, respectively.

The exact solution of eq. (2.2) is very complicated and some approximation is needed to find the ground state energy, W_0, and wavefunction, Ψ_0. The Born-Oppenheimer approximation allows to disentangle the ionic and electronic degrees of freedom. This approximation takes into account the fact that ionic mass is much larger than the electronic one ($m_e/M_j \leq 10^{-3}$), and therefore the time scale of ionic dynamics is much larger than the electronic one. The ionic kinetic energy can thus be neglected when studing the electronic motion, and one can first solve the problem of N interacting electrons, considering fixed ions acting as an external potential. The last term in eq. (2.2) becomes a constant at fixed ionic coordinates $\mathbf{R}_j$, and one has to solve an electronic hamiltonian, where ionic positions are present as parameters:

$$H_{el}\left(\{\mathbf{r}_i\};\{\mathbf{R}_j\}\right)\psi_n\left(\{\mathbf{r}_i\};\{\mathbf{R}_j\}\right) = E_n\left(\{\mathbf{R}_j\}\right)\psi_n\left(\{\mathbf{r}_i\};\{\mathbf{R}_j\}\right), \tag{2.3}$$

with:

$$\begin{aligned} H_{el}\left(\{\mathbf{r}_i\};\{\mathbf{R}_j\}\right) &= \sum_{i=1}^{N} -\frac{\hbar^2}{2m_e}\nabla^2_{\mathbf{r}_i} + \\ &- \sum_{i=1}^{N}\sum_{j=1}^{M} \frac{e^2 Z_j}{|\mathbf{r}_i - \mathbf{R}_j|} + \sum_{i<j}^{N} \frac{e^2}{r_{ij}} + \sum_{i<j} \frac{e^2 Z_i Z_j}{R_{ij}}, \end{aligned} \tag{2.4}$$

where ψ_n are the eigenstates of the electronic problem and the subscript n denotes the electronic quantum number. Solving eq. (2.4) as a function of ionic configurations, gives the so called adiabatic potential energy surfaces $E_n(\{\mathbf{R}_j\})$, of which the most relevant is the ground state potential energy surface $E_0(\{\mathbf{R}_j\})$. Once the electronic problem is solved, we address the full ionic and electronic problem, eq. (2.2), using the Born-Oppenheimer product for the total wavefunction $\Psi(\{\mathbf{r}_i\},\{\mathbf{R}_j\})$:

$$\Psi(\{\mathbf{r}_i\},\{\mathbf{R}_j\}) = \chi(\{\mathbf{R}_j\})\,\psi_0(\{\mathbf{r}_i\};\{\mathbf{R}_j\}), \tag{2.5}$$

where ψ_0 is the ground state solution of the electronic problem, and χ depends only on the ionic coordinates. Using the expression of eq. (2.5) corresponds to force electrons to stay in the same adiabatic potential energy surface during the ionic dynamics, and to adjust their wavefunction istantaneously to the new ionic configurations. When the full hamiltonian of eq. (2.2) is addressed using Ψ as defined in eq. (2.5) as variational wavefunction, and neglecting terms of the order of (m_e/M_j), we arrive at a Schrödinger equation for $\chi(\{\mathbf{R}_j\})$:

$$\left[\sum_{j=1}^{M} -\frac{\hbar^2}{2M_j}\nabla^2_{\mathbf{R}_j} + E_0(\{\mathbf{R}_j\})\right]\chi(\{\mathbf{R}_j\}) = W\chi(\{\mathbf{R}_j\}). \tag{2.6}$$

The ionic dynamics is so determined by the adiabatic potential energy surface, which implicitly takes into account the electronic kinetic energy, and all electrostatic interactions.

2.2 Density Functional Theory

Density Functional Theory proposes a way to simplify the solution of the electronic problem, and the basic idea has been formulated by Hohenberg and Kohn in 1964 [3]. In the study of a many-electron problem, DFT avoids the calculation of the ground state wavefunction, which depends on the $3N$ electronic coordinates, and it shows that the ground state energy of a system of N interacting electrons can be expressed as a functional of the electron

ground state density $n(\mathbf{r})$:

$$n(\mathbf{r}) = \langle \psi_0(\mathbf{r}_1, ..., \mathbf{r}_N) | \sum_{i=1}^{N} \delta(\mathbf{r} - \mathbf{r}_i) \, | \psi_0(\mathbf{r}_1, ..., \mathbf{r}_N) \rangle \, , \tag{2.7}$$

where ψ_0 is the ground state wavefunction. Dealing with the density $n(\mathbf{r})$ is simpler than ψ_0, since it is a function only of the three spatial coordinates.

Let's write the electronic hamiltonian as:

$$H = T_e + V_{ee} + V_{ext}, \tag{2.8}$$

where T_e is the electronic kinetic energy, V_{ee} is the electron-electron Coulomb interaction, and V_{ext} the external potential. Here we neglect the electrostatic interaction between ions, which is a constant at fixed ionic coordinates, and can be added to the total energy once the electronic problem is solved. Hohenberg and Kohn have demonstrated that not only the electron density in the ground state is uniquely determined by the external potential V_{ext}, but also the converse is true: the external potential V_{ext} is uniquely determined by $n(\mathbf{r})$. Since the external potential and N (which is simply the integral of the electronic density over the space) fully characterize the hamiltonian, it follows that $n(\mathbf{r})$ determines also the electron ground state wavefunction ψ_0. The total energy E of the electronic system can thus be written as:

$$E\,[n] = F\,[n] + \int v_{ext}(\mathbf{r}) \; n(\mathbf{r}) \; d\mathbf{r}. \tag{2.9}$$

$F\,[n]$ is an universal functional of $n(\mathbf{r})$, which does not depend on the external potential, and it is given by:

$$F\,[n] = \langle \psi_0\,[n] | \, T + V_{ee} \, | \psi_0\,[n] \rangle \, , \tag{2.10}$$

where $\psi_0\,[n]$ is the electron ground state wavefunction corresponding to $n(\mathbf{r})$. The last term in eq. (2.9), is the electronic interaction with the external potential V_{ext}, and its expression comes from the definition of the electron density in eq. (2.7), and the fact that V_{ext} can be written as:

$$V_{ext}\,(\mathbf{r}_1, ..., \mathbf{r}_N) = \sum_{i}^{N} \int v_{ext}(\mathbf{r}) \; \delta(\mathbf{r} - \mathbf{r}_i) d\mathbf{r}, \tag{2.11}$$

$$v_{ext}(\mathbf{r}) = -\sum_{j}^{M} \frac{e^2 Z_j}{|\mathbf{r} - \mathbf{R}_j|}. \tag{2.12}$$

The ground state density of the system is the one which minimizes $E[n]$, and it can be shown that the minimum of $E[n]$ is the ground state energy of the system. According to this theory, once the functional $F[n]$ and the expression of the external potential are known, the exact ground state energy and density can be found. Unfortunately the exact expression of $F[n]$ is not known, and approximations are nedeed. An useful approximation has been proposed by Kohn and Sham in 1965 [4] , and their idea is that one can write $F[n]$ as a sum of well known terms and a smaller term which is unknow, but hopefully easier to be approximated. In particular:

$$F[n] = T_0[n] + E_H[n] + E_{xc}[n], \tag{2.13}$$

where $T_0[n]$ is the kinetic energy of an auxiliary system of non-interacting electrons, having the same density of the real system, $E_H[n]$ is the energy due to the electrostatic interaction between electrons:

$$E_H[n] = \frac{e^2}{2} \int \frac{n(\mathbf{r})n(\mathbf{r}')}{|\mathbf{r} - \mathbf{r}'|}\, d\mathbf{r}\, d\mathbf{r}', \tag{2.14}$$

and $E_{xc}[n]$ is the exchange-correlation energy, which is the unknown part of $F[n]$.

The density of the auxiliary system of non-interacting electrons can be written in terms of one-particle orbitals ϕ_i:

$$n(\mathbf{r}) = \sum_{i=1}^{N} |\phi_i(\mathbf{r})|^2 . \tag{2.15}$$

Minimizing the total energy $E[n]$ with respect to ϕ_i, and using the Lagrange multipliers for the orthonormalization of ϕ_i:

$$\int \phi_i^*(\mathbf{r})\phi_j(\mathbf{r})\, d\mathbf{r} = \delta_{ij}. \tag{2.16}$$

we arrive to the so called Kohn and Sham one-particle equations:

$$\left[-\frac{\hbar^2}{2m_e}\nabla^2 + V^{KS}(\mathbf{r}) \right] \phi_i(\mathbf{r}) = \epsilon_i \phi_i(\mathbf{r}), \tag{2.17}$$

where the potential $V^{KS}(\mathbf{r})$ is given by:

$$V^{KS}(\mathbf{r}) = v_{ext}(\mathbf{r}) + V_H(\mathbf{r}) + V_{xc}(\mathbf{r}), \tag{2.18}$$

$$V_H(\mathbf{r}) = e^2 \int \frac{n(\mathbf{r}')}{|\mathbf{r} - \mathbf{r}'|}\, d\mathbf{r}', \tag{2.19}$$

$$V_{xc}(\mathbf{r}) = \frac{\delta E_{xc}[n]}{\delta n(\mathbf{r})}. \tag{2.20}$$

Eq. (2.17) can be numerically solved using iterative methods, since V_{xc} and V_H depend on the solutions ϕ_i. In particular, starting trial wavefunctions and potential are choosen, and at each step both are updated, until self-consistency is reached. The total energy of the system can be calculated from the Kohn and Sham eigenvalues in the following way:

$$E = \sum_{i=1}^{N} \epsilon_i - \frac{e^2}{2} \int \frac{n(\mathbf{r})n(\mathbf{r}')}{|\mathbf{r} - \mathbf{r}'|} d\mathbf{r} d\mathbf{r}' - \int V_{xc}(\mathbf{r}) n(\mathbf{r}) d\mathbf{r} + E_{xc}[n]\,. \tag{2.21}$$

Eq. (2.21) gives an exact expression for the total energy of the system. However $E_{xc}[n]$ is not known and it needs an approximation.

The simplest approximation for the exchange and correlation functional is the so called Local Density Approximation (LDA), where:

$$E_{xc}^{LDA}[n(\mathbf{r})] = \int \epsilon_{xc}^{hom}(n(\mathbf{r}))\; n(\mathbf{r})\; d\mathbf{r}. \tag{2.22}$$

In this approximation, every small volume of the system conributes to the exchange-correlation energy $\epsilon_{xc}^{hom}(n(\mathbf{r}))$ as in a homogeneous system with the same local density $n(\mathbf{r})$. The exchange-correlation potential $V_{xc}(\mathbf{r})$ as defined in eq. (2.20) becomes:

$$V_{xc}^{LDA}(\mathbf{r}) \equiv \frac{\delta E_{xc}^{LDA}[n]}{\delta n(\mathbf{r})} = \epsilon_{xc}^{hom}(n) + n\; \frac{d\epsilon_{xc}^{hom}(n)}{dn}. \tag{2.23}$$

The use of LDA approximation for the exchange-correlation functional gives good results for structural properties of systems where the electron density changes slowly, and to describe ionic, covalent and metallic bonds. However, binding energies are usually overestimated by LDA, in particular for systems where weaker bonds are present. Another class of approximations

for the exchange-correlation functional is the Generalized Gradient Approximation (GGA), where it is assumed that E_{xc} depends not only on the electron density, but also on the local gradient of the electron density:

$$E_{xc}^{GGA}\left[n, |\boldsymbol{\nabla} n|\right] = \int F_{xc}(n, |\boldsymbol{\nabla} n|)\, d\mathbf{r}. \tag{2.24}$$

All the results presented in this work are obtained with the GGA approximation proposed by Perdew, Burke and Ernzerhof (PBE) [48].

2.3 Plane waves and pseudopotentials technique

According to the DFT scheme outlined above, the eigenvalues and eigenstates of the Kohn and Sham equations (2.17) must be found. In the case of crystal lattice, $V^{KS}(\mathbf{r})$ is a periodic function of the Bravais lattice:

$$V^{KS}(\mathbf{r} + \mathbf{R}) = V^{KS}(\mathbf{r}), \tag{2.25}$$

where $\mathbf{R}$ is a vector in the Bravais lattice. According to Bloch theorem, the solutions of an hamiltonian with such potential can be written as:

$$\phi_i(\mathbf{r}) \equiv \phi_{n\mathbf{k}}(\mathbf{r}) = e^{i\mathbf{k}\cdot\mathbf{r}}\; u_{n\mathbf{k}}(\mathbf{r}), \tag{2.26}$$

where $u_{n\mathbf{k}}(\mathbf{r})$ is a function with the same periodicity of the Bravais lattice, n is the index of electronic band, and $\mathbf{k}$ is a vector in the first Brillouin zone.

Inserting the expression (2.26) into the eq. (2.17) we arrive at the following equation:

$$\left[\frac{\hbar^2}{2m_e}\left(-i\nabla + \mathbf{k}\right)^2 + V^{KS}(\mathbf{r})\right] u_{n\mathbf{k}}(\mathbf{r}) = \epsilon_{n\mathbf{k}}\; u_{n\mathbf{k}}(\mathbf{r}). \tag{2.27}$$

This equation can be solved expanding the periodic wavefunction $u_{n\mathbf{k}}(\mathbf{r})$ in plane waves:

$$u_{n\mathbf{k}}(\mathbf{r}) = \frac{1}{\sqrt{\Omega}} \sum_{\mathbf{G}} e^{i\mathbf{G}\cdot\mathbf{r}} c_{n\mathbf{k}}(\mathbf{G}), \tag{2.28}$$

where $\mathbf{G}$ are vectors in the reciprocal space, and Ω is the volume of the primitive cell. Using expression (2.28) in eq. (2.27), we obtain:

$$\sum_{\mathbf{G}'} \left[\frac{\hbar^2}{2m_e} |\mathbf{k}+\mathbf{G}|^2 \delta_{\mathbf{G},\mathbf{G}'} + V^{KS}(\mathbf{G}-\mathbf{G}') \right] c_{n\mathbf{k}}(\mathbf{G}') = \epsilon_{n\mathbf{k}}\, c_{n\mathbf{k}}(\mathbf{G}). \quad (2.29)$$

To solve eq. (2.29) a sum over an infinite number of $\mathbf{G}$ vectors should be performed. In practice, a finite set of $\mathbf{G}$ vectors is used, which is determined by the parameter E_{cut}, defined as:

$$\frac{\hbar^2}{2m} |\mathbf{k}+\mathbf{G}|^2 \leq E_{cut}, \quad (2.30)$$

which represents the maximum kinetic energy of the plane waves. Increasing E_{cut} one can improve the accuracy in the expansion of the one-electron wave functions and in the calculation of the total energy.

The ground state electron charge density $n(\mathbf{r})$ is calculated performing an integration over the first Brillouin zone, and a sum over all the occupied states:

$$n(\mathbf{r}) = \sum_{\mathbf{k}} \sum_{n} w_{\mathbf{k}} \vartheta(\epsilon_F - \epsilon_{n\mathbf{k}}) |u_{n\mathbf{k}}(\mathbf{r})|^2, \quad (2.31)$$

where ϵ_F is the Fermi energy, and $w_{\mathbf{k}}$ is the weight of $\mathbf{k}$ points in the first Brillouin zone. The charge density can be expanded in plane waves and we obtain:

$$n(\mathbf{r}) = \frac{1}{\Omega} \sum_{\mathbf{G}} e^{i\mathbf{G}\cdot\mathbf{r}} \tilde{n}(\mathbf{G}). \quad (2.32)$$

The number of $\mathbf{G}$ vectors to be used in eq. (2.32) is determined by the parameter E_{cutrho}, defined as:

$$\frac{\hbar^2}{2m} |\mathbf{G}|^2 \leq E_{cutrho}. \quad (2.33)$$

Inserting the expansion (2.28) into eq. (2.31), it can be shown that the maximim modulus of $\mathbf{G}$ vectors used in eq. (2.32) is twice the maximum modulus of $\mathbf{G}$ used in eq. (2.28). For an exact evaluation of the density, the value of E_{cutrho} is connected to E_{cut} by $E_{cutrho} = 4E_{cut}$.

In practice, when choosing E_{cut} a compromise must be found between the accuracy of the calculations and computational memory and time. Since core

electrons are very localized and valence wavefunctions, which are orthogonal to the core ones, show rapid oscillations in the core region, the number of **G** vectors to be used to describe the electron wavefunctions would be huge. A solution to this problem is provided by the pseudopotential scheme. The basic idea is to neglect core electrons, since their binding energy is much higher than the one of chemical bonds, which we are interested in, and they do not contribute directly to the chemical properties of the system. In the pseudopotential scheme, core electrons are considered together with nuclei, and the system is re-defined as composed of ions (nuclei + core electrons) and valence electrons. In the Kohn and Sham equation, $V^{KS}(\mathbf{r})$ is substituted by:

$$V^{PS}(\mathbf{r},\mathbf{r}^{'}) = V^{eff}(\mathbf{r})\delta(\mathbf{r}-\mathbf{r}^{'}) + V_{nl}(\mathbf{r},\mathbf{r}^{'}), \tag{2.34}$$

where $V^{eff}(\mathbf{r})$ is the long range local part of the pseudopotential and it takes into account the electrostatic interaction between electrons and nuclei, electrostatic and exchange-correlation interaction between valence electrons. The second part in $V^{PS}(\mathbf{r},\mathbf{r}^{'})$ is the short range non local part of the pseudopotential, and it is given by:

$$V_{nl}(\mathbf{r},\mathbf{r}^{'}) = \sum_{l=0}^{l_{max}} V_{nl,l}(\mathbf{r},\mathbf{r}^{'})P_l(\hat{\mathbf{r}},\hat{\mathbf{r}}'). \tag{2.35}$$

where $V_{nl,l}(\mathbf{r},\mathbf{r}^{'})$ depends on the angular momentum l, and $P_l(\hat{\mathbf{r}},\hat{\mathbf{r}}')$ is the projector on the angular momentum. $V_{nl,l}(\mathbf{r},\mathbf{r}^{'})$ takes into account the interaction between valence and core electrons (i.e. electrostatic and exchange-correlation interaction, and orthogonalization between core and valence electrons).

$V_{nl,l}(\mathbf{r},\mathbf{r}^{'})$ is build starting from all-electrons calculations for each atom involved in the system. In particular, for each atomic species a core radius r_c is definided, and all-electron and pseudo-wavefunctions are required to coincide for $r \geq r_c$, and eigenvalues to be equal. The pseudo-wavefunctions for $r \leq r_c$ are choosen to be smooth, nodeless and continous, together with first derivative, at r_c. The valence charge inside the core region, calculated with pseudo-wavefunctions, must be equal to the one calculated with all-electron wavefunctions, which garantees orthonormalization of pseudo-wavefunctions. These pseudopotentials are called norm-conserving [49, 50, 51].

The norm conservation requirement for the pseudo-wavefunctions can result in "hard" pseudopotentials requiring a large E_{cut} when valence electrons are very localized around nuclei. This happens, for example, for first-row elements as well as for transition metals, where d electrons are localized as core electrons, while their energies are comparable to those of valence electrons, and therefore they cannot be considered as core electrons. In this situation, using norm-conserving pseudopotentials a large number of plane waves is required to achieve a sufficient accuracy in wavefunction description. In 1990 Vanderbilt introduced a more general formalism [52], which allows to remove the norm-conservation requirement. These pseudopotentials are called ultrasoft, since by relaxing the norm-conservation condition the pseudo-wavefunctions can be smoother. Ultrasoft pseudopotentials have been used, as implemented in the `Quantum ESPRESSO` package, to obtain all the numerical results presented in this thesis. In the ultrasoft pseudopotential formalism a small number of plane waves is required to write the pseudo-wavefunctions, and the only requirements is that all-electron and pseudo-wavefunctions coincide for $r \geq r_c$, where r_c is greater than the corresponding core radius for norm-conserving peudopotentials. Furthermore, the quality of a pseudopotential is mainly determined by the transferability of the pseudopotentials, that is the ability to reproduce all-electron results in a certain range of electronic configurations and energies. The ultrasoft pseudopotentials by construction reproduce all-electron wavefunctions at different energy values, thus enhancing their transferability.

The pseudo-wavefunctions obtained with ultrasoft pseudopotentials have a different normalization with respect to the all-electron wavefunctions, and they give a different charge density in the core region. Therefore, an appropriate term, localized in the core region, must be introduced. Due to the presence of these augmentation charges, an additional test is required to check the plane waves basis set used to expand the charge density, and with ultrasoft pseudopotentials, the needed E_{cutrho} results to be higher than $4E_{cut}$. An operator $\hat{S}$ is then introduced such that the pseudo-wavefunctions obey to the following orthonormalization condition:

$$\langle \phi^{PS}_{n\mathbf{k}} | \hat{S} | \phi^{PS}_{n'\mathbf{k}} \rangle = \delta_{n,n'}. \tag{2.36}$$

Using the above normalization and minimizing the total energy of the system with respect to $\phi^{PS}_{n\mathbf{k}}$, it can be shown that the generalized Kohn and Sham equation becomes:

$$\left[-\frac{\hbar^2}{2m_e}\nabla^2 + V^{PS}\right]\left|\phi^{PS}_{n\mathbf{k}}\right\rangle = \epsilon_{n\mathbf{k}}\hat{S}\left|\phi^{PS}_{n\mathbf{k}}\right\rangle . \tag{2.37}$$

2.4 Thermally activated processes

The ethylene epoxidation reaction, which is addressed in this thesis, proceeds through three main elementary steps: dissociation of oxygen molecule, formation of the OxaMetallaCycle (OMC) intermediate from ethylene and oxygen, and transformation of the OMC into ethylene epoxide (EO) or other undesired product. Each elementary step corresponds to a transition from an initial state (IS) to a final state (FS), which are energetically stable configurations. These kinds of processes are called thermally activated, since, in order for the transition to occur, an energy barrier (E^*) must be overcome. This energy barrier is usually higher than thermal fluctuations around local minima, and therefore they occur rarely. Instead, the system spends most of the time oscillating around local minima, with a frequency of about 10^{13} s^{-1}, which depends on the curvature of the potential energy surface in the local minima. Thermally activated processes are therefore also called rare events. As described below, a statistical approah to this problem gives an estimate of the time τ the system has to wait before overcoming the barrier, which results to be proportional to the exponential of the ratio between the energy barrier and thermal energy:

$$\tau \approx \tau_{osc}\, e^{E^*/k_{\mathrm{B}}T}, \tag{2.38}$$

where τ_{osc} is the typical time scale of oscillations around the minimum, and k_{B} is the Boltzmann constant. For instance, for a chemical reaction whith $E^* = 1$ eV, at 300 K, and $\tau_{\mathrm{osc}} = 10^{-13}$s, the typical time scale to overcome the barrier is $\tau \approx 10^3 s$, which is many order of magnitude larger than the time scale of molecular vibrations.

Rare events cannot be studied directly by means of molecular dynamics (MD) simulations. Within MD, the time evolution of the system is performed

by integrating the equation of motion, where forces are given by the gradient of the potential energy surface. In order to be accurate enough, the time step δt used in the integration must be smaller than typical microscopic time scales (for instance smaller than 10^{-13} s). It follows that a huge number of integration steps n is required in order to explore the dynamics of the system at time scales τ much larger than the integration time step ($n \approx \tau/\delta t$). Therefore, within MD one can study the oscillations of reactants and products around the local minima, but a different method is needed to investigate the transition between them.

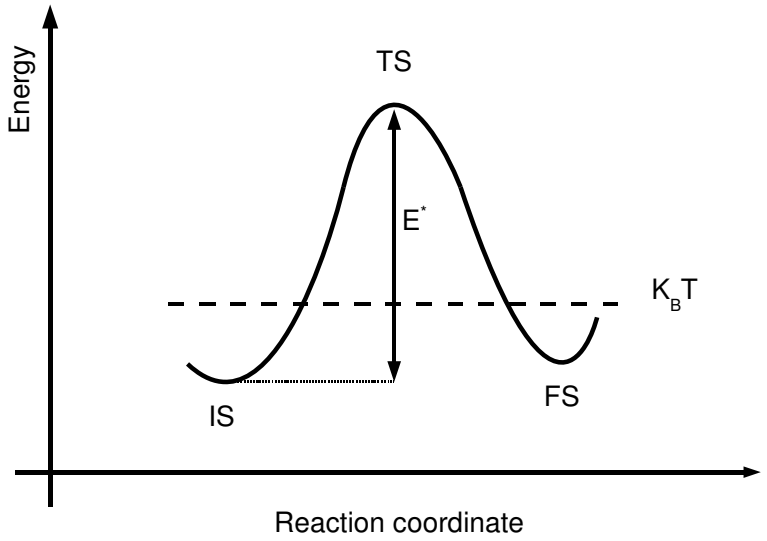

Figure 2.1: *Schematic one-dimensional representation of a potential energy surface. IS: initial state or reactans; FS: final state or products; TS: transition state. Reaction proceeeds via the minimun energy path (MEP) connecting IS to FS. TS is the highest energy configuration along the MEP, and it corresponds to a saddle point (in one-dimensional representation it corresponds to a maximum). E^* is the activation energy. k_BT is the thermal energy of the system.*

A statistical approach to address this kind of problem is adopted in the so-called *Transition-State Theory* (TST). From a statistical point of view,

a chemical reaction is seen as the evolution of IS into FS, which are local minima in the potential energy surface, as schematically shown in Fig. 2.1. In order to study the transformation of IS into FS and vice-versa, the following kinetic equations are usually adopted:

$$\frac{dN_{IS}}{dt} = -k^{\rightarrow}N_{IS} + k^{\leftarrow}N_{FS}, \tag{2.39}$$

$$\frac{dN_{FS}}{dt} = k^{\rightarrow}N_{IS} - k^{\leftarrow}N_{FS}, \tag{2.40}$$

where N_{IS} and N_{FS} are ensemble populations of initial and final states, respectively. $k^{\rightarrow}$ and $k^{\leftarrow}$ represent the probability to cross (from IS to FS and viceversa) the transition state (TS), which is defined as the configuration with highest energy along the reaction pathway. At equilibrium ($dN_{IS}/dt = dN_{FS}/dt = 0$), the populations $N_{\rm IS}$ and $N_{\rm FS}$ are given by the Boltzmann distribution, and the equilibrium constant ($k^{\rightarrow}/k^{\leftarrow} = e^{-(E_{FS}-E_{IS})/k_{\rm B}T}$) does not depend on the activation energy, but only on the energy of the IS and FS.

When the properties of the non-equlibrium system have to be investigated, an estimate of transition rates $k^{\rightarrow}$ and $k^{\leftarrow}$ is needed. TST is based on the assumption that reactants and products are distributed according to the Boltzmann distribution, and that transition from reactants to products occurs without subsequent return. Therefore, the evolution of the reactants is decoupled from the evolution of products, keeping $k^{\leftarrow} = 0$ in eq.(2.39), so that:

$$\frac{dN_{IS}}{dt} = -k^{\rightarrow}N_{IS}, \tag{2.41}$$

where the transition rate $k^{\rightarrow}$ measures the flux of configurations crossing the TS with positive velocity (from IS to FS). In particular, in a one-dimensional representation as shown in Fig. 2.1, we have:

$$k^{\rightarrow} = -\frac{\langle\ \frac{p}{m}\ \theta(p)\ \delta(r - r^{TS})\ \rangle}{\langle\ \theta(r^{TS} - r)\ \rangle}, \tag{2.42}$$

where (r, p) are position and momentum in the phase space, and r^{TS} are the real space coordinates of the TS. The complete derivation of $k^{\rightarrow}$ is omitted here and it can be found in ref. [53]. In a one-dimensional picture and with

the assumption that the PES can be approximated harmonically around the initial state, the final expression for $k^{\rightarrow}$ is:

$$k^{\rightarrow} = \nu(r^{IS})\ e^{-E^*/k_{\mathrm{B}}T}, \tag{2.43}$$

where $\nu(r^{IS}) = \sqrt{E''(r^{IS})/m}$ is the oscillation frequency around the IS, and $E^* = (E^{\mathrm{TS}} - E^{\mathrm{IS}})$ is the so-called activation energy or energy barrier. Eq. (2.43) is the *van't Hoff-Arrhenius* law, and it states that the probability for a rare events to occur depends only on the properties of the potential energy surface at zero temperature, and the temperature dependence of the transition rate is determined by the energy difference between TS and IS. Eq. (2.43) can be generalized to $3N_{\mathrm{at}}$-dimension case, where the prefactor depends on the oscillation frequency around IS and TS. In this thesis we consider thermally activated processes on metal surfaces, and this prefactor can be roughly assumed to be similar when moving from one metal surface to another. Therefore, the transition rate is mainly determined by the exponential-temperature dependent part, and it uniquely depends on the activation energy.

As described in chapter 1, the selectivity, which is the main topic addressed in this thesis, is defined as the percentage of consumed reactants trasformed into the desired product. In other worlds, the selectivity can be defined as the ratio between the rate of formation of desired product and the sum of the rates of all the products. In the specif case of the EO formation from the OMC intermediate, it will be shown in the next chapter that acetaldehyde (Ac) is the undesired product, leading to total combustion, thus reducing the selectivity toward EO. Therefore, taking into account the van't Hoff-Arrhenius law for transition rate as written in eq. (2.43), we can write the selectivity S for EO formation as:

$$S = 1/\left[1 + e^{-(E^*_{Ac} - E^*_{EO})/k_B T}\right], \tag{2.44}$$

where E^*_{Ac} and E^*_{EO} is the activation energy for the Ac and EO synthesis, respectively. Therefore, the selectivity in the ethylene epoxidation is determined by the quantity $\Delta E^* = (E^*_{\mathrm{Ac}} - E^*_{\mathrm{EO}})$, and the more positive is ΔE^*, the higher is the selectivity toward EO.

2.5 Climbing-Image Nudged Elastic Band Method

According to the van't Hoff-Arrhenius law derived in the previous section, the transition rate is mainly determined by the exponential-temperature dependent part, which depends on the energy difference between the TS and IS. The IS and FS are identified with standard minimization algorythms based on PES first derivatives, which converge very well to local minima. Instead, for the location of the TS it is useful to identify the reaction pathway, which is given by the Minimum Energy Path (MEP) between the two local minima. The MEP is characterized by having, at each point, vanishing forces in the direction perpendicular to the path:

$$\mathbf{F}_{\perp} = \mathbf{F} - \hat{\tau}\left[\hat{\tau} \cdot \mathbf{F}\right] = 0, \tag{2.45}$$

where $\hat{\tau}$ is the versor tangent to the path, $\mathbf{F} = -\nabla V$, and V is the potential energy surface.

From the computational point of view, this equation can be addressed discretizing the path into N so-called images (Fig. 2.2, red points), and applying the MEP equation to every image:

$$-\nabla V(\mathbf{x}_i) + \hat{\tau}_i\left[\hat{\tau}_i \cdot \nabla V(\mathbf{x}_i)\right] = 0, \tag{2.46}$$

$$\hat{\tau}_i = \frac{\mathbf{x}_{i+1} - \mathbf{x}_i}{|\mathbf{x}_{i+1} - \mathbf{x}_i|}, \tag{2.47}$$

where $(\mathbf{x}_i)$ are the coordinates of image i, with $i = 1, ..., N$, and a possible approximation of the tangent $\hat{\tau}_i$ is given. One can think to solve this set of coupled equations in an iterative way. In particular, N starting images between IS and FS are choosen, and for each of them $\hat{\tau}_i$, total energy and force orthogonal to the path are calculated. If $\mathbf{F}_{\perp}$ is different from zero, the position of the corresponding image is changed accordingly, until forces are vanishing and the minimun perpendicular to the path is found. By using this algorythm, the convergence toward the MEP would not be achieved, because all the images would collapse into the closest local minima (for instance into IS and FS).

In order to avoid this problem, in the *Nudged Elastic Band* method (NEB) [54] an elastic interaction between nearest neighbour images is introduced,

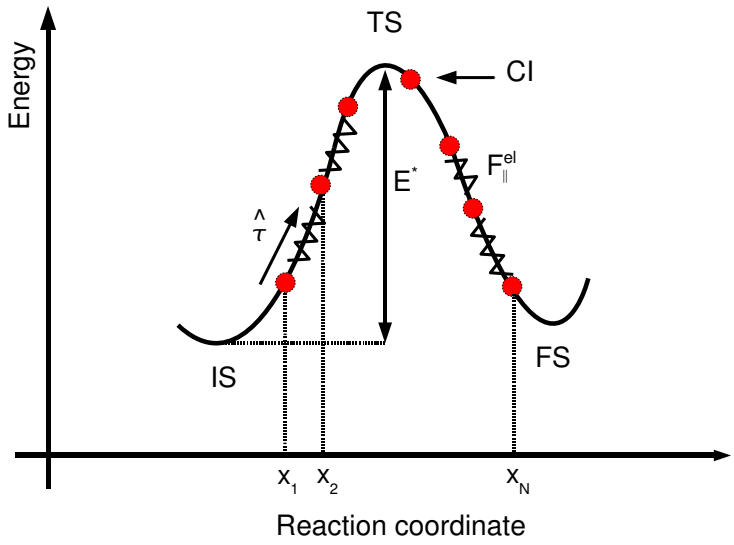

Figure 2.2: *Schematic representation of the methods used to identify MEP and TS, in one-dimensional PES. Red points correspond to N images between IS and FS, connected by springs. CI: climbing image; $\hat{\tau}$: versor tangent to the path; $\mathbf{F}_{\parallel}^{\mathrm{el}}$: elastic force parallel to the path.*

which keeps the images approximately equispaced along the path. Only the component of the elastic force parallel to the path, $\mathbf{F}_{\parallel}^{\mathrm{el}}$ (see Fig. 2.2), is allowed to act on the images, whose dynamics is now determined by a total force $\mathbf{F}$:

$$\begin{aligned}\mathbf{F}(\mathbf{x}_i) = \{-\nabla V(\mathbf{x}_i) + \hat{\tau}_i\,[\hat{\tau}_i \cdot \nabla V(\mathbf{x}_i)]\} + \\ -k\,[(2\mathbf{x}_i - \mathbf{x}_{i+1} - \mathbf{x}_{i-1}) \cdot \hat{\tau}_i]\,\hat{\tau}_i.\end{aligned} \tag{2.48}$$

The first contribution in eq. (2.48) is the force perpendicular to the path due to the potential energy surface, while the second contribution is the elastic force parallel to the path. k is the elastic force constant, and it can be defined such that it is stronger for images closer to the TS, in order to have a higher density of images and a better description of the path around the TS.

Even using a large number of images, usually none of them will be exactly

at the TS, which corresponds to a saddle point along the MEP. For this reason, a variant of the NEB method, called *Climbing Image* (CI) NEB [55], has been introduced. Within the CI-NEB, the image closest to the TS is choosen to climb the hill and to approach the TS (see Fig. 2.2). This image does not feel the elastic force and its dynamics is determined by a force **F**:

$$\mathbf{F}(\mathbf{x}_{C-I}) = -\nabla V(\mathbf{x}_i) + 2\hat{\tau}_i \left[\hat{\tau}_i \cdot \nabla V(\mathbf{x}_i)\right], \tag{2.49}$$

where the component parallel to the path is now reversed. The climbing image therefore moves toward a minimun in the direction perpendicular to the path, and toward a maximun along the path, which corresponds to move exactly toward a saddle point.

In this thesis, the CI-NEB, as implemented in the `Quantum Espresso` distribution [56], has been used.

Chapter 3

Ethylene epoxide and acetaldehyde formation on d-metals

In this chapter, ethylene epoxide (EO) and acetaldehyde (Ac) formation from the OxaMetallaCycle (OMC) intermediate, on (100) and (111) surfaces of IB metals, as well as of on a more reactive model catalyst such as rhodium, is systematically investigated. Two kinds of defective Ag surfaces (Ag adatom on Ag(100) and the stepped Ag(210)), and the effect of high oxygen coverage on Ag(100) have been also investigated. Activation energies are reported, with a structural characterization of initial states (IS), transition states (TS) and final states (FS).

Based on the analysis of our data, we observe that a mild catalyst is required for EO and/or Ac formation, otherwise other competing reactions, in particular those involving C–H bond breaking in the IS, would take place. Still the catalyst must be reactive enough to dissociate oxygen molecule and to form the OMC. Silver, as well as other noble IB metals, fulfill these requirements.

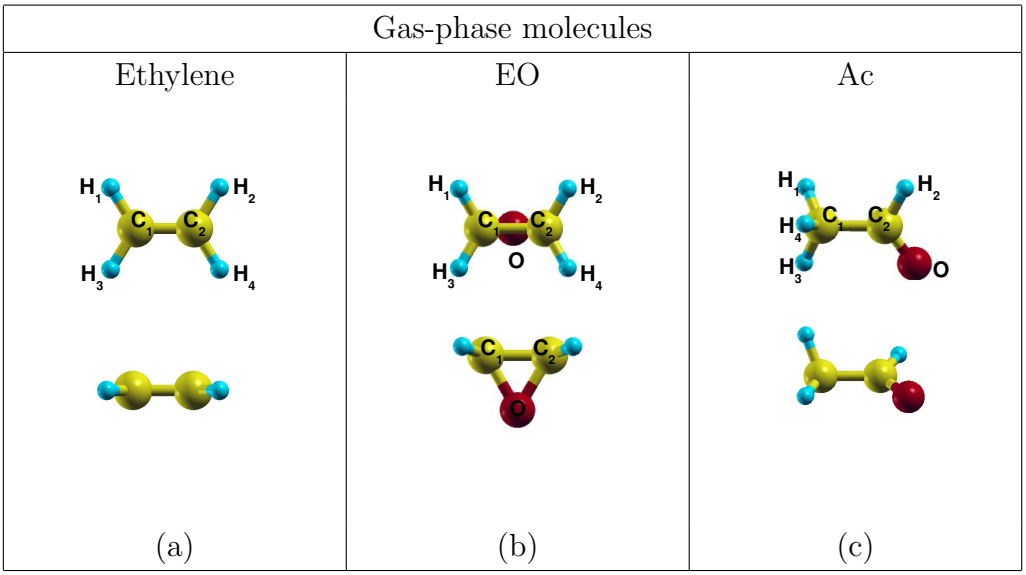

Figure 3.1: *Gas-phase ethylene (a), ethylene epoxide (b) and acetaldehyde (c) molecules.*

3.1 From reactants to products: the reaction pathway

3.1.1 Gas phase molecules

In this section we report the structural characteristics of gas-phase ethylene, ethylene epoxide (EO) and acetaldehyde (Ac), which are involved in the ethylene epoxidation reaction. The ethylene (together with oxygen molecule) represents the reactant, EO is the desired product, while Ac is the undesired product, leading to total combustion. In Fig. 3.1 the geometries of gas-phase ethylene, EO and Ac are shown, and in Tabs. 3.1, 3.2 and 3.3 the main structural parameters obtained in this work are reported, compared with experimental results.

It is worth to notice that the C–C bond distance changes significantly in the considered molecules, and it is elongated from 1.33 Å in ethylene to 1.46 and 1.50 Å in EO and Ac, respectively. Indeed, during the insertion of O atom in the ethylene molecule, to form both EO and Ac, C atoms undergo an sp^2 to sp^3 rehybridization, and the C–C double bond in the ethylene is

	C_1–C_2 (Å)	C_1–H_1 (Å)	$H_1\widehat{C}_1H_3$ (°)	$H_1\widehat{C}_1C_2$ (°)
This work	1.33	1.09	116	122
Exp. [57]	1.34	1.09	117	121

Table 3.1: *Structural parameters of gas-phase ethylene.*

	C_1–C_2 (Å)	C_1–H_1 (Å)	C_1–O (Å)	$H_1\widehat{C}_1H_3$ (°)	$H_1\widehat{C}_1C_2$ (°)	$O\widehat{C}_1C_2$ (°)
This work	1.47	1.09	1.45	116	119	59
Exp. [57]	1.46	1.08	1.42	117	119	59

Table 3.2: *Structural parameters of gas-phase EO.*

	C_1–C_2 (Å)	C_1–H_3 (Å)	C_2–H_2 (Å)	C_2–O (Å)	$H_3\widehat{C}_1H_4$ (°)	$H_2\widehat{C}_2C_1$ (°)	$O\widehat{C}_2C_1$ (°)
This work	1.49	1.09	1.12	1.22	110	115	125
Exp. [57]	1.50	1.09	1.11	1.22	108	117	124

Table 3.3: *Structural parameters of gas-phase Ac.*

transformed into a single bond in EO and Ac.

In the next sections the adsorption energy of EO and Ac on metal surfaces will be reported, and it is calculated as:

$$E_{\text{ads}}^{\text{EO(Ac)}} = E_{\text{sys}} - E_{\text{surf}} - E_{\text{EO(Ac)}}, \tag{3.1}$$

where E_{sys} is the energy of the system, with EO (Ac) adsorbed on the surface, E_{surf} is the energy of clean metal surface, and $E_{\text{EO(Ac)}}$ is the energy of gas-phase EO (Ac). Structural parameters of final states will be omitted, since EO and Ac result to be weakly bound to the considered surfaces, and in practice their geometries correspond to those of gas-phase molecules. The only exception is Ac on Rh(100) and Rh(111), where a chemisorbed state is found and corresponding structural parameters will be reported.

3.1.2 The oxametallacycle intermediate

A minimal sequence of elementary steps of the overall ethylene epoxidation reaction are schematically represented in Fig. 3.2. The rate determining steps are the oxygen molecule dissociation, activated by the metal surface, and the formation of an OMC intermediate, which has been recently established, both theoretically and experimentally, to be an intermediate in the EO synthesis [23, 24, 25, 26, 27, 28, 29]. In the OMC a ring structure is formed by the ethylene fragment, the adsorbed O atom and surface metal atoms. Once the OMC is formed, it reacts to form either EO (selective product) or Ac (undesired product, leading to total combustion). The formation of EO proceeds via the O–C ring closure (path 1 in Fig. 3.2), while during the Ac formation one H atom shifts from the central to the terminal C atom (path 2 in Fig. 3.2). The selectivity in the ethylene epoxidation is controlled by the transformation of the OMC into EO or Ac, and it depends on the difference between the activation energy for Ac and EO formation (see chapter 2, section about thermally activated processes).

The formation of the OMC is an activated process, where the C–C double bond in the ethylene is transformed into a single bond, and O atom is incorporated in the ethylene fragment. Different OMC structures can be identified, depending on the surface sites C and O atoms are bound to. The

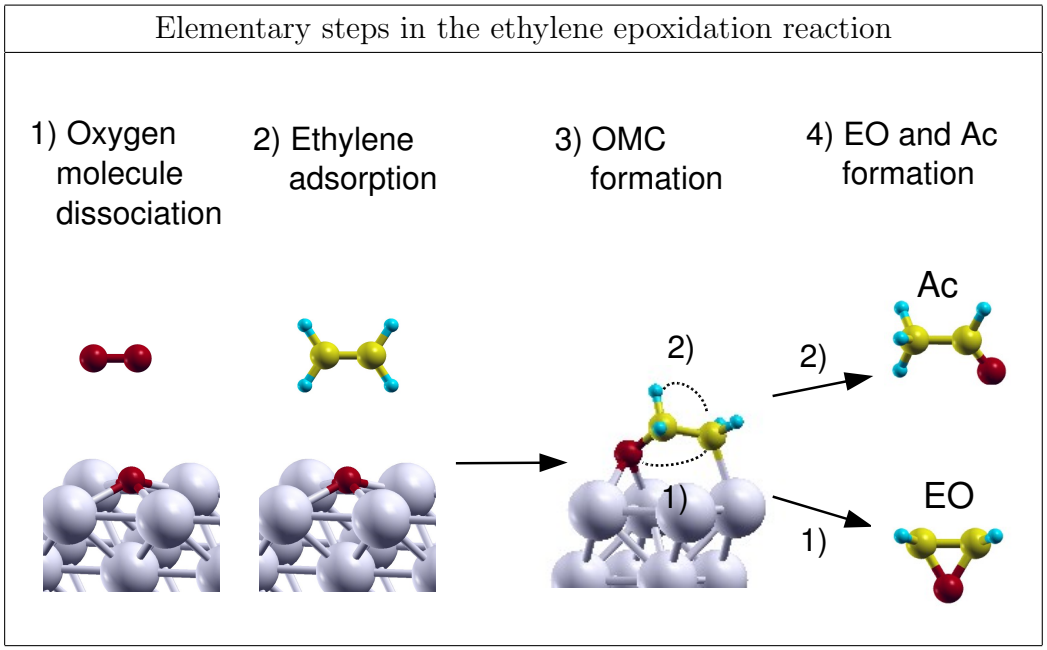

Figure 3.2: *Sequence of elementary steps in the ethylene epoxidation reaction: 1) dissociative adsorption of oxygen molecules; 2) ethylene adsorption, and 3) formation of the OMC intermediate; 4) EO (path 1) and Ac (path 2) formation. Ac is the undesired product, leading to total combustion (omitted in this schematic representation).*

activated adsorption of ethylene has been investigated in detail on atomic oxygen covered Ag(100) surface [58], and in Fig. 3.3 identified OMC structures on Ag(100) are shown. The main structural parameters and adsorption energies are reported. The OMC geometries are labelled as O_xMC_y, where x and y indicate the surface sites O and C atoms bind to. In particular b, t and h stand for bridge, top, and hollow sites, respectively.

The OMC adsorption energy presented in this work is calculated as:

$$E_{\mathrm{ads}}^{\mathrm{OMC}} = E_{\mathrm{syst}} - E_{\mathrm{surf}} - E_{\mathrm{EO}}, \tag{3.2}$$

where E_{syst} is the energy of the system, with the OMC adsorbed on the surface, E_{surf} is the energy of clean metal surface, and E_{EO} is the energy of gas-phase EO. This is not the natural choice to calculate the OMC adsorption energy. Indeed, since the OMC is formed from ethylene and oxygen adsorbed on the surface, the OMC adsorption energy should be calculated with respect

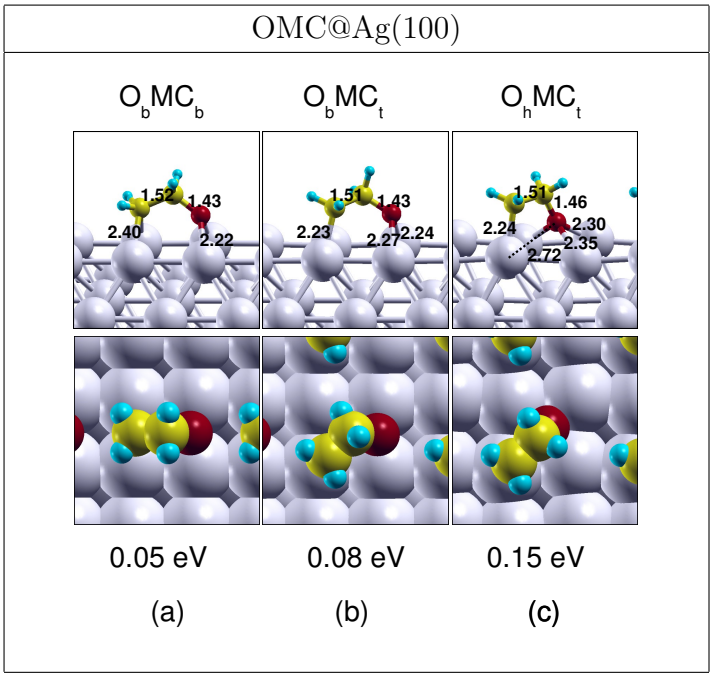

Figure 3.3: *Identified OMC structures on Ag(100): (a)* O_bMC_b*; (b)* O_bMC_t*; (c)* O_hMC_t*. Subscripts b, t and h stand for bridge, top and hollow, and they refer to surface sites where O and C atoms bind to. Structural parameters (Å) and adsorption energy (eV) are reported. Adsorption energy is calculated with respect to EO gas-phase and clean Ag(100) surface.*

to these constituents. However, using this definition, the OMC adsorption energy would include also the energy cost to partially break O–surface bond to incorporate O in the OMC structure. While the transformation of the C–C double bond into single bond in the ethylene can be considered as a constant energy penalty, the energy cost of incorporating O in OMC strongly depends on the local chemical environment. For this reason, we reported the $E_{\text{ads}}^{\text{OMC}}$ as defined in eq. (3.2), which gives a proper description of the interaction of the OMC with the surface. Indeed, this quantity can be seen as opposite to the energy required to remove the OMC from the surface to a given reference state in the gas-phase, that we chose to be EO. In this process, the OMC–surface bonds are broken and a new C–O bond is formed, but the latter is a constant contribution when moving from one metal surface to another. Ac could be also chosen as reference state in the gas-phase. In this case, all the

OMC adsorption energies would be higher by a constant term, since Ac is 1.02 eV more stable than the gas-phase EO.

On Ag(100) three stable OMC structures have been identified: O_bMC_b, shown in Fig. 3.3 (a), which is the most stable, O_bMC_t (b) and O_hMC_t (c). The formation of these three different OMC structures requires a low activation energy, about 0.3 eV, and transfomation between them is found to be facile, due to very low activation energy, about 0.1 eV. The formation of the OMC has been investigated also on the stepped Ag(210) [58], and when the step-edge is fully decorated by oxygen, which is a very stable configuration [59], the barrier for OMC formation increases to 0.5 eV.

A structural characterization of the most stable OMC structures, used as IS for EO and Ac formation on metal surfaces considered in this work, is given in the next section.

3.1.3 EO and Ac formation from the OMC on Ag, Cu, Au and Rh metal surfaces

In this section, results for EO and Ac formation, starting from the OMC intermediate, on Ag, Cu, Au and Rh (100) and (111) unreconstructed surfaces are reported. Two models of defective Ag surfaces have been considered: Ag adatom on Ag(100) and the stepped Ag(210) surface. The effect of high O coverage on Ag(100) is also investigated. All the results are collected in Figs. 3.4–3.9, where reaction pathways are schematically represented, and OMC, TS's, EO and Ac geometries are shown. Activation energies and entalphies of reaction, measured with respect to the OMC energy, are reported, together with OMC and TS structural parameters.

General features. Looking at the figures, one can notice some general properties. For instance, all the OMC structures show a C–C bond distance of around 1.50 Å, longer than the equivalent value in the ethylene gas-phase (1.33 Å), while the C–O is around 1.45 Å. In the TS for Ac formation, the C–C and C–O bonds are around 1.45 and 1.30 Å, respectively, shorter than in the OMC. This TS is characterized by the H shift from the central carbon atom (let's call it C_1) to the terminal one. The C_1–H bond is 1.10 Å in the

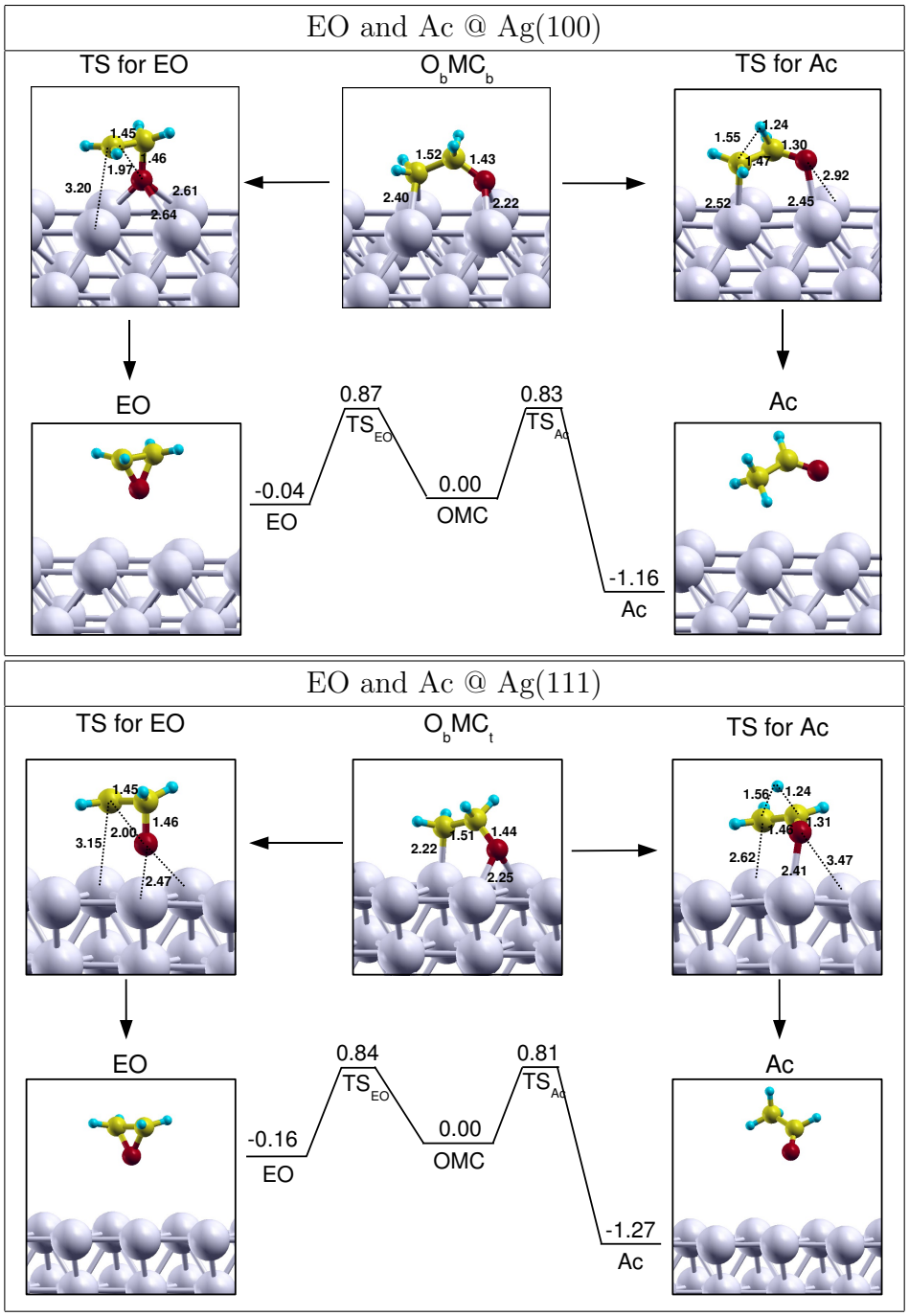

Figure 3.4: *OMC, TS's, EO and Ac on Ag(100) and on Ag(111). Reaction pathways are schematically represented. Distances are in Å and energies in eV, measured with respect to OMC energy.*

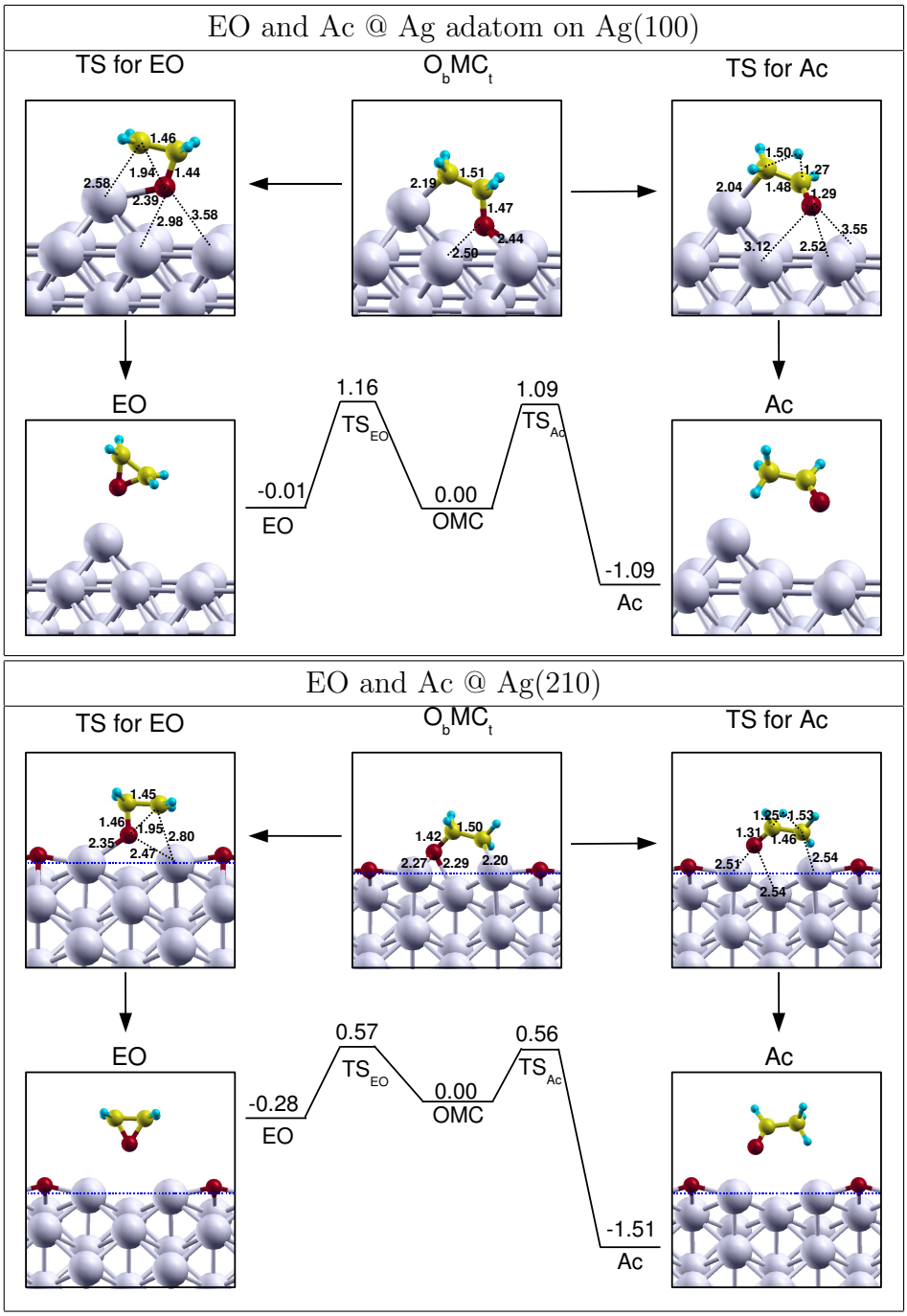

Figure 3.5: *OMC, TS's, EO and Ac on Ag adatom on Ag(100) and on stepped Ag(210) surface. Reaction pathways are schematically represented. Distances are in Å and energies in eV, measured with respect to OMC energy. Blue dashed line shows the step-edge.*

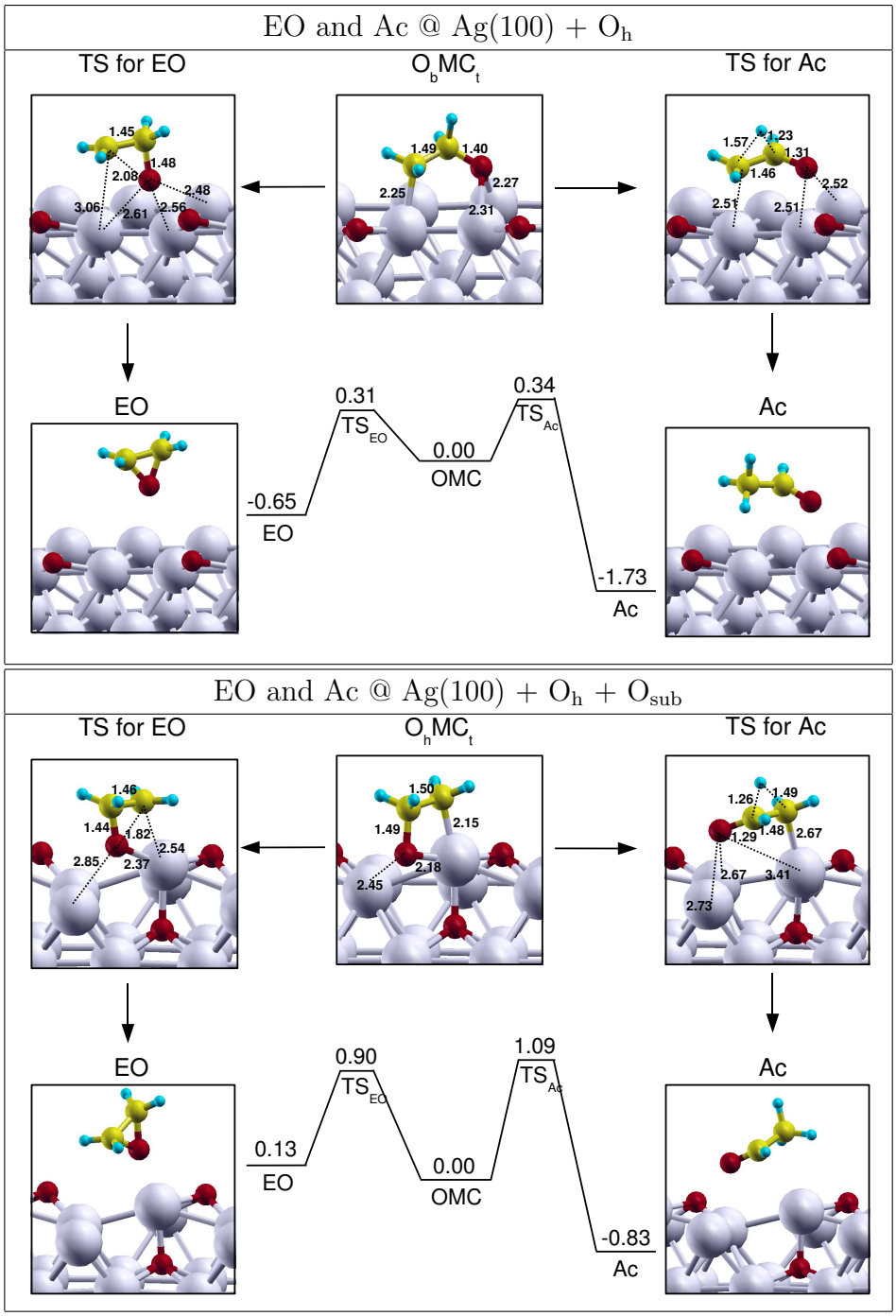

Figure 3.6: *OMC, TS's, EO and Ac on Ag(100) +* O_h *and on Ag(100) +* O_h *+* O_{sub}*. Reaction pathways are schematically represented. Distances are in Å and energies in eV, measured with respect to OMC energy.*

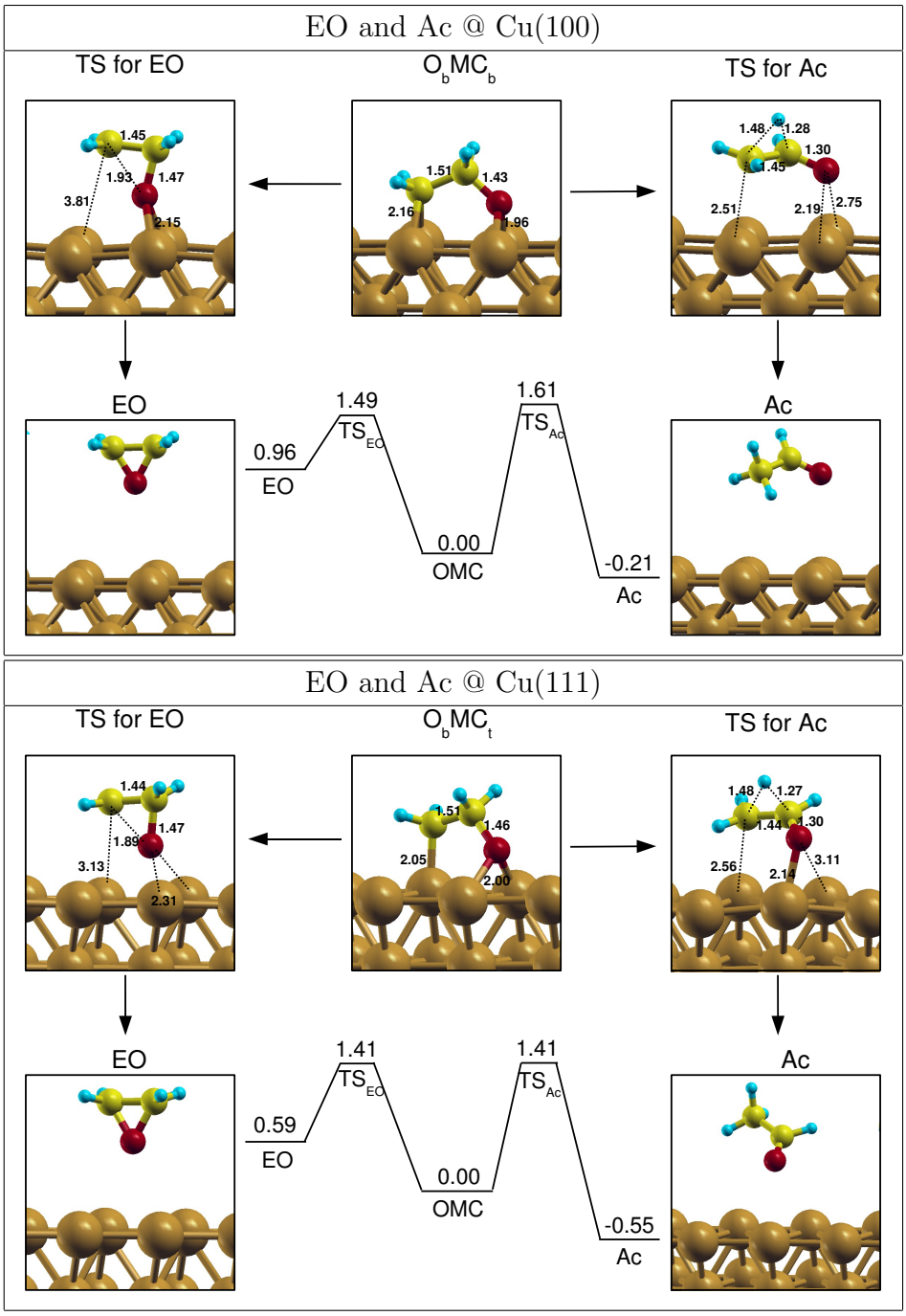

Figure 3.7: *OMC, TS's, EO and Ac on Cu(100) and on Cu(111). Reaction pathways are schematically represented. Distances are in Å and energies in eV, measured with respect to OMC energy.*

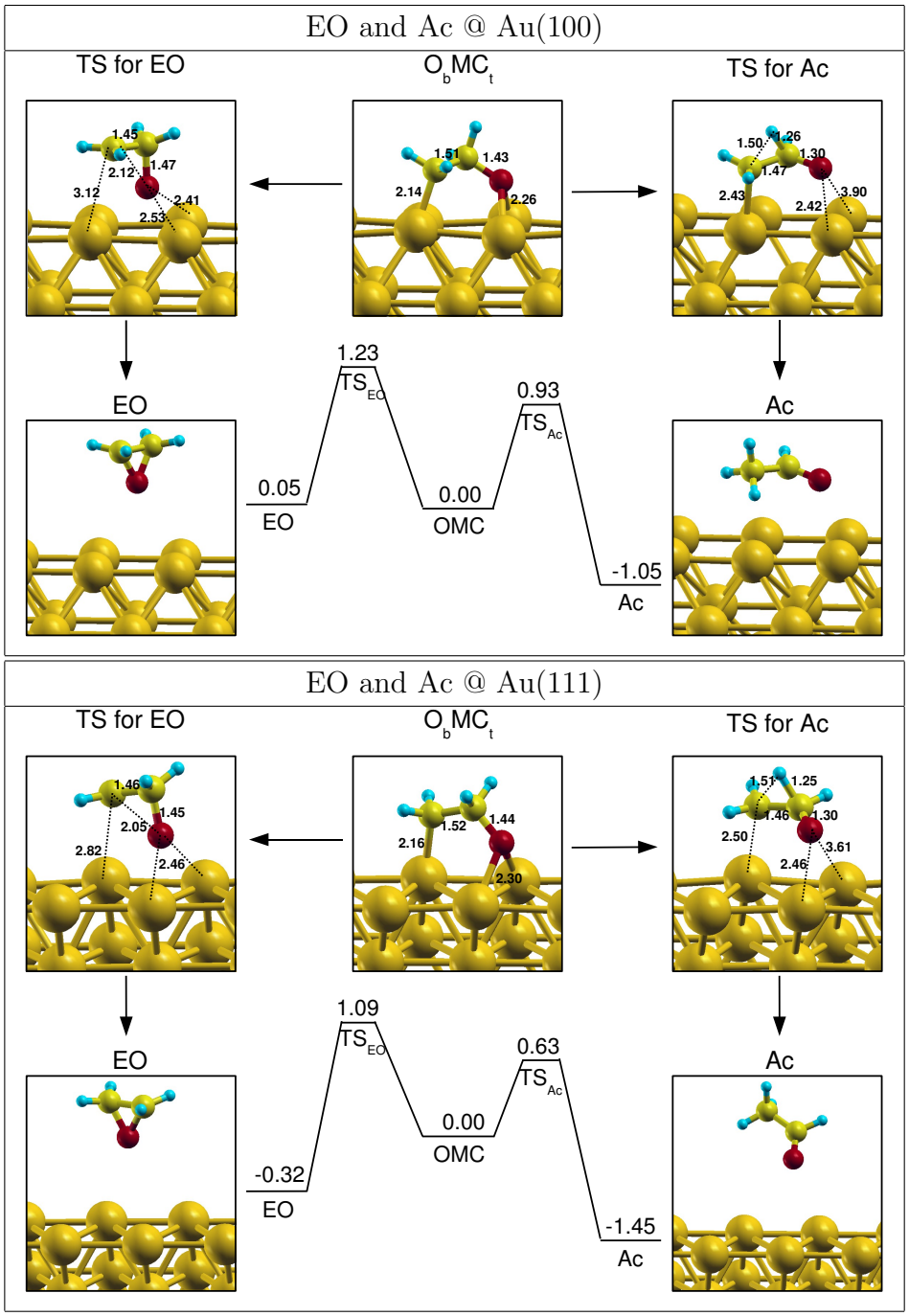

Figure 3.8: *OMC, TS's, EO and Ac on Au(100) and on Au(111). Reaction pathways are schematically represented. Distances are in Å and energies in eV, measured with respect to OMC energy.*

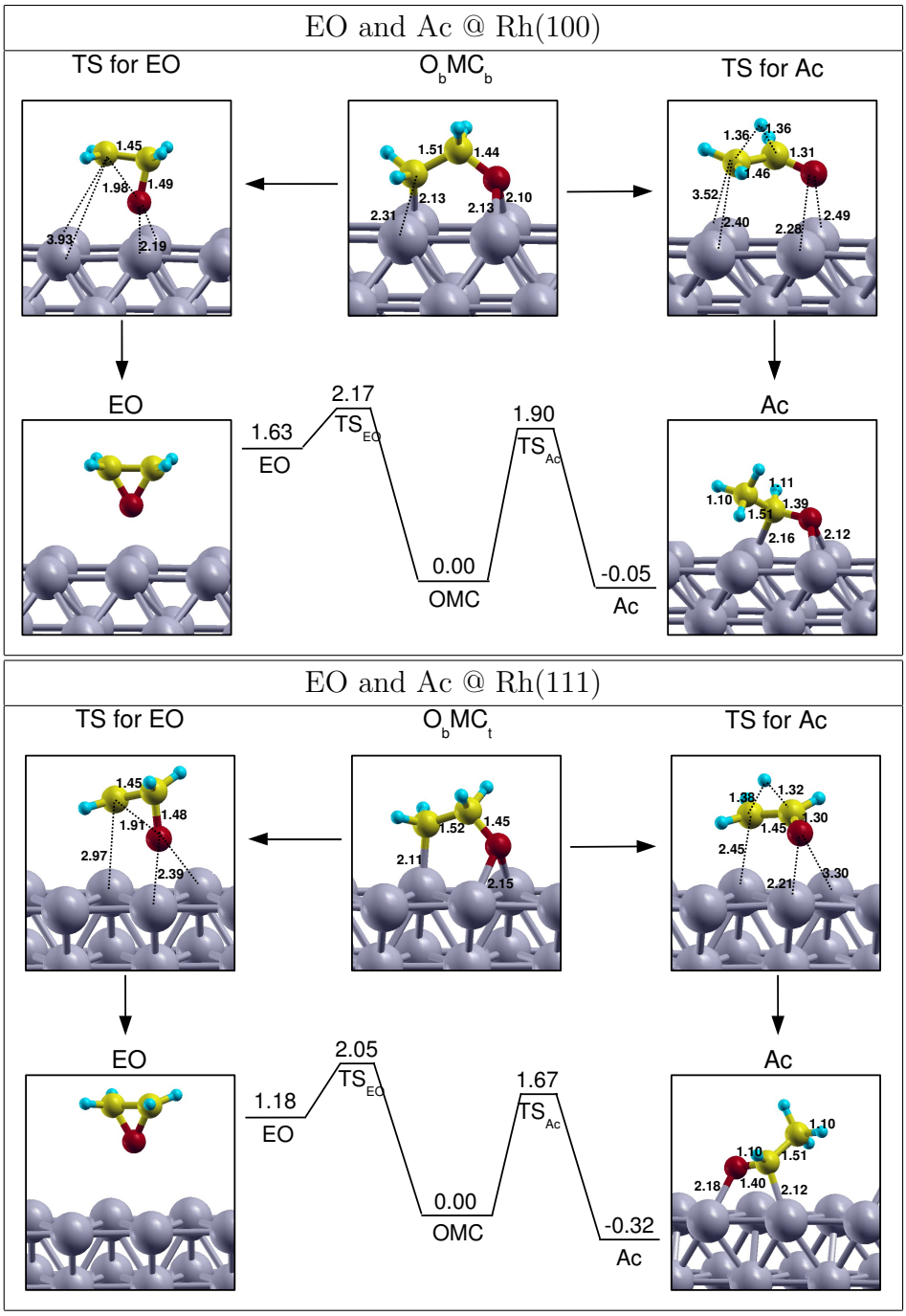

Figure 3.9: *OMC, TS's, EO and Ac on Rh(100) and on Rh(111). Reaction pathways are schematically represented. Distances are in Å and energies in eV, measured with respect to OMC energy.*

ethylene gas-phase and also in the OMC, while in the TS leading to Ac it is elongated to about 1.25 Å. On Rh(100) and (111) surfaces C_1–H is elongated even more, up to 1.36 Å (see Fig. 3.9). Finally, in the TS for EO formation, the C–C bond, for all the considered surfaces, is around 1.45 Å, slightly lower than in the OMC, while C–O bond is around 1.45 Å, not significantly changed with respect to the OMC.

Structural parameters of FS's are not reported, since EO and Ac are weakly bound to the surfaces (the adsorption energy is usually few tenths of eV), and in practice their geometries coincide with those of the corresponding gas-phase molecules. The only exception is the Ac on Rh(100) and Rh(111) surfaces. In these cases, the adsorption energy is higher than half eV, and this is due to the high reactivity of Rh compared to IB metals, which allows the formation of a chemisorbed state, which is an Ac derived oxametallacycle (see Fig. 3.9). Therefore structural parameters are reported for Ac on Rh(100) and Rh(111), since they differ from those of gas-phase Ac. In particular, the C–O bond distance is elongated from 1.22 Å in the gas-phase molecule to around 1.40 Å on the Rh surfaces.

As for the energetics, we notice that Ac final state is more stable than EO for all the considered surfaces. This is due to the fact that Ac gas-phase molecule is about 1 eV more stable than EO. In particular, Ac formation from the OMC is very exothermic on Ag and Au surfaces (more than 1 eV), while EO is slighly exothermic or athermic (see Figs. 3.4 and 3.8). On Cu and Rh surfaces, Ac formation results to be less exothermic with respect to Ag and Au, and EO formation is highly endothermic (see Figs. 3.7 and 3.9). This is due to the stronger interaction of oxygen on Cu and Rh surfaces, with respect to Ag and Au, which lower the energy of the OMC. The high endothermicity found for EO on Cu surfaces is in agreement with previous theoretical results [43].

Ag surfaces: the effect of defects and high O coverage. Our results show that on Ag surfaces with 1/4 ML of OMC coverage, the Ac formation is slightly favored with respect to EO (see Fig. 3.4), accounting for the 40 % selectivity observed for the initial stage of the reaction on unpromoted Ag surfaces [1, 2]. The effect of surface defects on EO and Ac formation has been

investigated on Ag, and two models of defective surface have been considered: Ag adatom on Ag(100) and the stepped Ag(210) surface (see Fig. 3.5). In particular, Ag adatom represents a more reactive adsorption site, due to lower coordination, while the Ag(210) surface has been used to model steps fully decorated by oxygen atoms, since this configuration, where chains of -Ag-O-Ag-O-Ag- are formed, results to be very stable [59]. According to our results, the presence of surface defects does not improve the catalyst selectivity toward EO, and Ac remains favored with respect to EO.

Also the effect of high oxygen coverage has been investigated on Ag(100), and our results are reported in Fig. 3.6. The oxygen coverage in the (100) and (111) surfaces considered in this work is always equal to the ethylene coverage. In particular, we used a (2×2) supercell with 1/4 ML of O adsorbed on the surface, which then reacts with 1/4 ML of ethylene to form the OMC. Starting from this model, we adsorbed an additional O atom per supercell in the hollow site, labelled as O_h, to simulate high on-surface oxygen coverage. To model Ag surface with subsurface O, we adsorbed O_h plus another O atom on subsurface octa site, labelled as O_{sub}. Indeed, it is well established that when O atoms are adsorbed on Ag surfaces at coverage higher than 1/2 ML, they start to adsorb subsurface and to form oxide-like structures [15, 60, 61, 62], which play an important role in the reactivity of metal catalysts under ordinary industrial conditions [5, 6, 7, 8]. In particular, due to the presence of subsurface O atoms, Ag(100) surface results to be more corrugated, because Ag surface atoms above subsurface O are pushed out, resulting in more reactive sites, due to lower coordination [18]. According to our results, shown in Fig. 3.6, the effect of high oxygen coverage, both on-surface and subsurface, makes the EO activation energy lower than the Ac one, improving the catalyst selectivity toward EO formation, compared with Ag with low oxygen coverage (see Fig. 3.4).

Other metal surfaces: Cu, Au and Rh. Among the other considered metal surfaces, Cu is the only one where the selectivity is improved with respect to Ag (see Fig. 3.7). This result is in agreement with previous theoretical studies [43, 44]. The contrary happens on Au and Rh surfaces. Au is the noblest of d-metals, and previous theoretial studies show a catalytic

activity very similar to that of Ag [63]. The main problem in using Au as catalyst for the ethylene epoxidation is the low activity of Au toward dissociation of oxygen molecules. Our results on Au surfaces show that Ac formation is favored with respect to EO, even more than on Ag surfaces (see Fig. 3.8). Also on Rh, which has been chosen as an example of very reactive metal surface, Ac formation results to be highly favored with respect to EO (see Fig. 3.9).

3.2 The effect of supercell dimension

Our results on Cu(111), reported in Fig. 3.7, are obtained using a (2×2) supercell. Since other theoretical studies claim that on Cu(111) the barrier for both EO and Ac depend on cell dimension [43, 44], we repeated these calculations using a (4×4) supercell. It is worth to notice that Cu has the smallest equilibrium bulk lattice parameter among the considered metals, and the (111) surface is more compact than the (100). Therefore, when a molecule is adsorbed on the surface, likely the effect of the supercell dimension on the lateral repulsion between periodic replica, is stronger on Cu(111) than on other metal surfaces considered in this work.

Our results show that going from (2×2) to (4×4) supercell on Cu(111), the activation energy for Ac formation increases from 1.41 to 1.44 eV, while the one for EO formation decreases from 1.41 to 1.27 eV, and selectivity toward EO is improved. This can be partially explained in terms of lateral dipole-dipole interaction, between periodic replica of EO and Ac. Indeed, according to the Brønsted-Evans-Polanyi (BEP) principle described in chapter 1, the activation energy can correlate with the energy of the FS's. Since TS structures for Ac and EO formation are similar to the corresponding FS's (at least from dipole point of view), we calculated the dipoles of EO and Ac molecules, to understand the effect of the supercell dimension on the activation energies. As shown in Fig. 3.10 (a), the EO molecular dipole is approximatively perpendicular to the surface, and the lateral interaction between periodic replica is repulsive. Therefore, increasing the distance between periodic replica, the EO and consequently its TS are stabilized, and the barrier decreases. In the case of Ac, the molecular dipole is approxima-

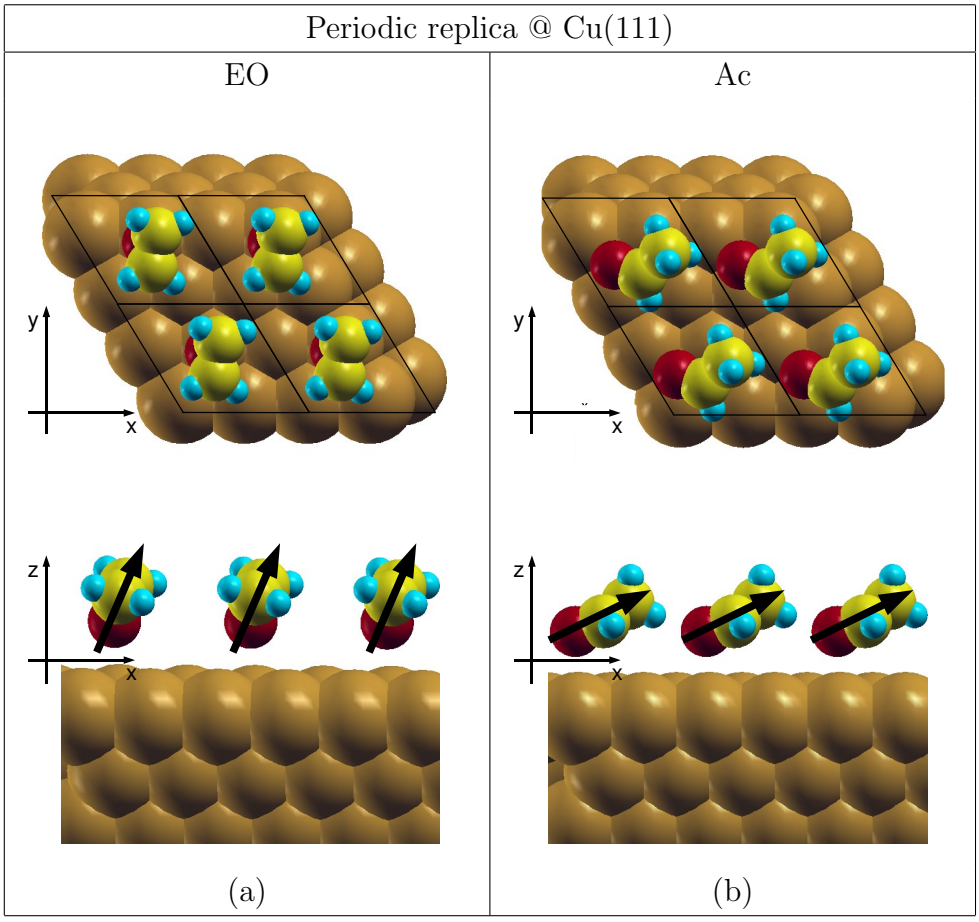

Figure 3.10: *Periodic replica of EO (a) and Ac (b), in the surface plane of Cu(111), from top and side view. Black line: periodic replica of* (2×2) *supercell. Black arrows: molecular dipole, pointing from negative charged O to positive charged C–C fragment.*

tively parallel to the surface, pointing in the x direction (see Fig. 3.10 (b)), and the lateral interaction between periodic replica is attractive along x and repulsive along y direction. Thus, increasing the distance between periodic replica along x direction the Ac is destabilized, while along y it is stabilized. The effect is stronger along x, since Ac molecule is more extended in that direction, and periodic replicas are closer. The overall result is that Ac and its TS are destabilized, and the barrier slightly increases. This observation is supported by the comparison between adsorption energies of EO and Ac, when increasing the distance between periodic replica: going from the (2×2) to (4×4) supercell, the adsorption energy of the EO is enhanced from -0.03 to -0.10 eV, while the adsorption energy of the Ac is weakened from -0.15 to -0.09 eV.

The effect of supercell dimension has been investigated also on Ag(100). Indeed, since the value of the EO adsorption energy on Ag(100), using a (2×2) supercell, is 0.01 eV, one can conclude that a small repulsive interaction between periodic replica of EO in this surface is present. Therefore, all calculations have been also performed on Ag(100) using a (4×3) supercell. Going from (2×2) to (4×3) supercell, on Ag(100) we find that the activation energy for the EO formation does not change, while that for the Ac formation increases by 0.16 eV, thus improving selectivity toward EO. Our findings are at variance with previous theoretical studies, where no dependence on supercell dimension was predicted for Ag surfaces [43]. For Ac and EO on this surface, we don't show the corresponding figures, since the orientation of the molecules in the supercell corresponds to that on Cu(111). Therefore, the above discussion on dipole-dipole interaction between periodic replica can be also applied to Ag(100), to explain the effect of supercell dimension on the activation energies. Indeed, also for Ag(100) we compare the adsorption energy for EO and Ac, when increasing the supercell dimension, and we find the same trend observed on Cu. In particular, the adsorption energy for EO is enhanced from 0.01 to -0.05 eV, while for the Ac it is slightly weakened from -0.09 to -0.06 eV.

3.3 Why is silver special for the ethylene epoxidation reaction?

#	Reaction	E_{act} [eV]	
		Ag(100)	Rh(100)
1	$C_2H_4 + O(a) \rightarrow OMC(a)$	0.33	0.31
2.1	$C_2H_4(a) \rightarrow C_2H_3(a) + H(a)$	>1.41	0.46
2.2	$C_2H_4(a) + O(a) \rightarrow C_2H_3(a) + OH(a)$	1.03	1.45
2.3	$OMC(a) \rightarrow C_2H_3O(a) + H(a)$	>1.55	0.26
3.1	$C_2H_4(a) \rightarrow 2CH_2(a)$	>3.08	1.33
3.2	$OMC(a) \rightarrow CH_2(a) + CH_2O(a)$	>1.69	1.62
4.1	$OMC(a) \rightarrow Ac$	0.83	1.90
4.2	$OMC(a) \rightarrow EO$	0.87	2.17
5	$OMC(a) \rightarrow C_2H_4 + O(a)$	0.68	1.13

Table 3.4: *Activation energies of some representative reactions that ethylene and its oxametallacycle (OMC) may undergo on Ag(100) and Rh(100) surfaces. Energies quoted as lower bounds are estimated from the energy difference between the products and the reactants. (a) means chemisorbed on the surface.*

In order to understand why silver is a special catalyst for the ethylene epoxidation reaction, we compare in Tab. 3.4 activation energies calculated for a number of relevant reactions on Ag(100) and on the more reactive Rh(100). (1: OMC formation; 2: C–H bond breaking; 3: C–C bond breaking; 4: product formation from the OMC intermediate; 5: ethylene formation back from OMC). It is known from experiments that more reactive metals break the C–H bond (and thus burn the ethylene), whereas Ag does not [2]. On Ag it has been suggested that C–H bonds may be activated by chemisorbed oxygen [1, 2, 13]. The results in Tab. 3.4 support these conclusions: on the more reactive Rh surface, ethylene dehydrogenation (2.1) and OMC formation (1) followed by its dehydrogenation (2.3) are by far the most favorable reactions, whereas the formation of EO and Ac, (4.1) and (4.2), are

the least probable. On Ag the most favorable reactions are instead the formation of OMC, (1), and its reverse, (5), followed by the transformation of OMC to EO and Ac, (4.1) and (4.2). Dehydrogenation reactions are less probable and, in particular, C–H bond activations by the metal itself, (2.1) and (2.3), have higher barriers than reaction (2.2) where C–H bond breaking is assisted by chemisorbed oxygen. These results clearly show that a mild catalyst is required for the formation of EO and/or Ac, otherwise other competing reactions, particularly those involving C–H bond breaking, would take place. Still, the catalyst should be reactive enough to form an ethylene OMC. Silver, as well as other noble IB metals, fulfill these requirements [43, 63, 64].

As for the formation of EO and Ac from the OMC intermediate, our results show a similar trend as previously found in a study of IB-metals, on (111) surfaces [43, 63]. Ag displays the smallest barriers for the formation of EO and Ac; the largest barriers occur on Cu, but Cu is intrinsically more selective than Ag [43]: the activation energy for the formation of EO is smaller than for Ac, whereas the opposite is true for Ag and Au, the latter being the least selective for the formation of EO. However, on Cu the formation of EO is endothermic, while the opposite is true on Ag (see Figs. 3.4 and 3.7), and Torres et al. anticipated that short contact times might be required to limit the decomposition of the EO product [43]. Moreover, passive oxide films form on Cu surfaces that inactivate the catalyst [39, 40]. Another problem with Cu is that it is reactive enough for the C–H bond to break significantly, at least on more open surfaces or near surface defects. On Cu(100) the calculated activation energy for OMC dehydrogenation, reaction (2.3), is 1.31 eV, hence lower than for the formation of EO and Ac (1.49 and 1.61 eV, respectively). On the more compact (111) surface this problem would be substantially alleviated. Namely, the latter two relevant activation energies are smaller, 1.27 and 1.44 eV, respectively, whereas the barrier for C–H bond breaking (1.52 eV) is larger than on Cu(100), consistently with the finding that the barrier for dehydrogenation increases with the atomic coordination of the reaction site [65, 66].

In summary, silver is a special catalyst for the ethylene epoxidation reaction because it is reactive enough to dissociate oxygen and to form the OMC intermediate, and mild enough to avoid other competing reactions, such as

C–H bond breaking, in both ethylene and OMC. Other IB metals fulfill these properties, but Ag displays the lowest barrier for the EO formation, which is an exothermic process, and Ac is only slightly favored.

Chapter 4

Factors determining the catalyst selectivity

In this chapter the selectivity of a catalyst in the ethylene epoxidation reaction is addressed. Indeed, in spite of the many computational and experimental studies on ethylene epoxidation, the specific factors which determine the catalyst selectivity are poorly understood.

Based on the results presented in the previous chapter, we propose a simple indicator for the catalyst selectivity, which considerably improves the straight application of the standard Brønsted-Evans-Polanyi (BEP) relation to both ethylene epoxide (EO) and acetaldehyde (Ac) formation reactions. Our indicator is suggested by the inspection of the two corresponding transition states. In particular, we observed that the selectivity is related to the differential bonding affinity of a catalyst toward the C– and O–atom in the OMC structure, and the stronger is OMC's O–metal bond with respect to its C–metal bond, the higher is the selectivity toward the EO formation.

4.1 BEP relation for the Ac and EO formation

In order to understand the factors that determine the catalyst selectivity toward EO synthesis (which at a given temperature mainly depends on the difference between the Ac and EO activation energies, $\Delta E^* = E^*_{\mathrm{Ac}} - E^*_{\mathrm{EO}}$),

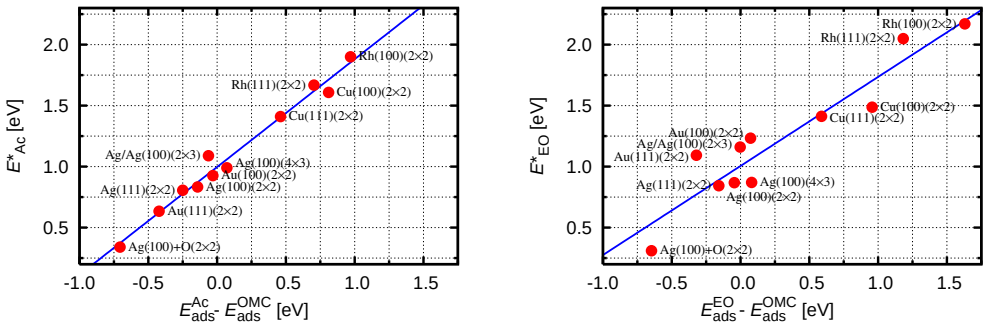

(a) (b)

Figure 4.1: *Correlation between the activation energy, E^*, and the entalphy of reaction, $\Delta H_r = E^{FS}_{ads} - E^{IS}_{ads}$ (BEP relation) for the formation of Ac (a) and EO (b). The rms errors are 0.07 and 0.18 eV for (a) and (b), respectively, whereas the largest error is 0.15 and 0.32 eV, respectively.*

Surface	E^*_{Ac}	E^*_{EO}	ΔE^*	E^{OMC}_{ads}	E^{Ac}_{ads}	E^{EO}_{ads}	$E^{CH_3}_{ads}$	$E^{CH_3O}_{ads}$
Ag(100)	0.83	0.87	−0.04	0.05	−0.09	0.01	−1.03	−1.97
Ag(100)-(4×3)	0.99	0.87	0.12	−0.13	−0.06	−0.05	−1.01	−2.00
Ag(111)	0.81	0.84	−0.03	0.12	−0.13	−0.04	−0.91	−1.74
Cu(100)	1.61	1.49	0.12	−0.98	−0.17	−0.02	−1.27	−2.43
Cu(111)	1.41	1.41	0.00	−0.62	−0.15	−0.03	−1.20	−2.30
Cu(111)-(4×4)	1.44	1.27	0.17	−0.68	−0.09	−0.10	−1.42	−2.39
Au(100)	0.93	1.23	−0.30	−0.08	−0.11	−0.01	−1.37	−1.42
Au(111)	0.63	1.09	−0.46	0.31	−0.12	−0.01	−1.21	−1.04
Rh(100)	1.90	2.17	−0.27	−1.76	−0.79	−0.13	−1.84	−2.41
Rh(111)	1.67	2.05	−0.38	−1.28	−0.58	−0.10	−1.74	−2.22
Ag/Ag(100)	1.09	1.16	−0.07	−0.23	−0.30	−0.24	−1.16	−1.70
Ag(100) + O_h	0.34	0.31	0.03	0.59	−0.12	−0.06	−0.78	−1.75

Table 4.1: *Collection of data obtained in this work and used for fits presented in this chapter. (4×3) and (4×4) represent the supercells used for the corresponding surfaces. All the other results are obtained using a (2×2) supercell. Ag/Ag(100) stands for Ag adatom on Ag(100).*

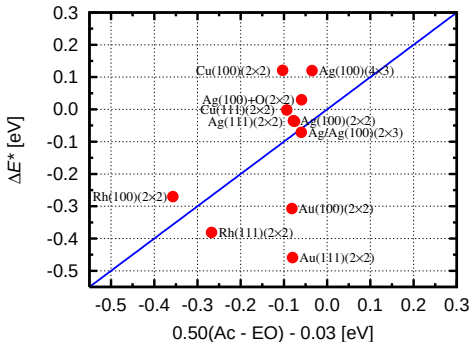

Figure 4.2: *Correlation between* $\Delta E^* = E^*_{\mathrm{Ac}} - E^*_{\mathrm{EO}}$ *and the BEP estimation of* ΔE^**:* $\Delta E^* \propto E^{\mathrm{Ac}}_{\mathrm{ads}} - E^{\mathrm{EO}}_{\mathrm{ads}}$*. The rms and largest errors are 0.19 and 0.38 eV, respectively.*

we have analyzed separately the formation of Ac and EO. In particular, we search for a simple quantity correlating with the activation energies, with the aim of devising an indicator for estimating the catalyst's selectivity. Torres *et al.*[44] recently suggested that the stabilization of the EO product decreases the barrier for the EO formation due to the BEP relation, according to which the activation energy correlates linearly with the entalphy of reaction, ΔH_{r}: $E^* = a + b\Delta H_{\mathrm{r}}$. In Fig. 4.1 we show the BEP fit for the formation of Ac and EO, using data from the main reactions considered in this work (listed in Tab. 4.1). These fits show that the formation of Ac follows remarkably well the BEP relation, whereas the formation of EO does so to a lesser extent (the root-mean-square error (rms) is 0.07 and 0.18 eV for the Ac and EO formation, respectively, the largest error being 0.15 and 0.32 eV, respectively).

Although an approximate magnitude of the activation energies for Ac and EO formation can be determined from the BEP principle, the BEP principle alone is not accurate enough to estimate the selectivity of a catalyst toward the EO formation (see Fig. 4.2). Indeed, since the two barriers are very similar, their difference, ΔE^*, is small, and the error, which is acceptable for the estimation of the activation energies, becomes too high for ΔE^*. Therefore an improvement to BEP relation is needed, and it will be discussed in the next sections.

4.2 Structural features of transition states

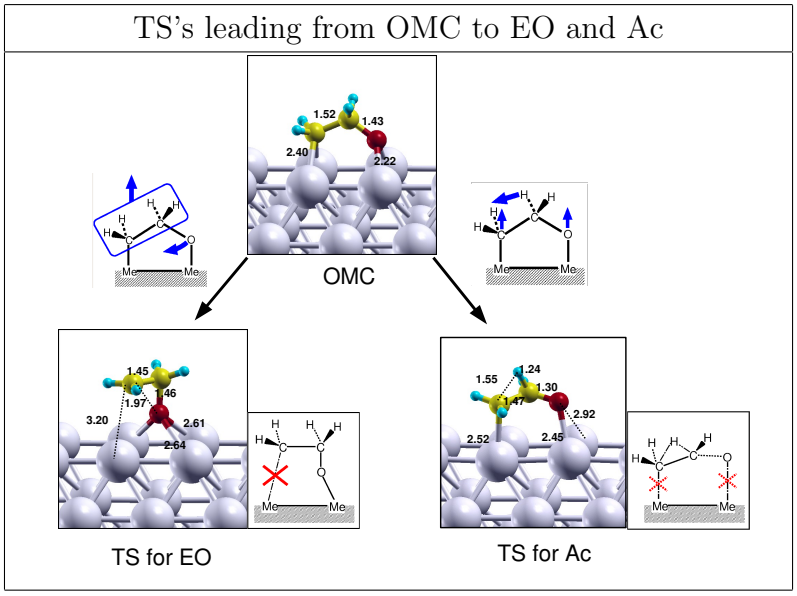

Figure 4.3: *Schematic representations of OMC on Ag(100) and transition states leading to EO (left) and Ac (right). In the TS leading to EO the C–surface bond is broken, whereas in the TS leading to Ac both C– and O–surface bonds are elongated (distances are in Å). During the EO formation the O-atom moves beneath the ethylene fragment, which is concomitantly shifted upward (indicated by blue arrows) and as a consequence the C–metal bond is broken, whereas in the formation of Ac the whole molecule is upshifted during the hydrogen shift, and consequently the C– and O–surface bonds are partially broken.*

In order to identify other important factors that determine the catalyst's selectivity toward the EO formation with respect to Ac, we analysed the structural features of the TS's for both reactions.

In Fig. 4.3 we display and compare the TS's for the EO and Ac formation from OMC on Ag(100), which we label as TS^{EO} and TS^{Ac}, respectively. We can notice that the main difference between the two TS's is that, in TS^{EO} the C–surface bond is fully broken, whereas in TS^{Ac} both C– and O–surface bonds are partially broken. These structural characteristics of the two TS's appear to be general and they can be observed also when reactions occur on

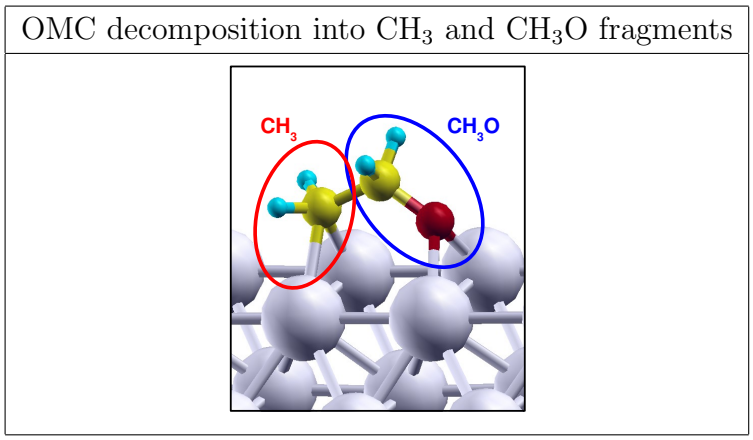

Figure 4.4: *The OMC–surface interaction can be decomposed into C– and O–surface terms, which can be approximated by the interaction of methyl (CH_3) and methoxy (CH_3O) with the surface, respectively.*

the other metal surfaces considered in this work (see chapter 3). In particular, during EO formation, the closure of the epoxy ring is made possible by the oxygen shift beneath the ethylene fragment that is concomitantly pushed upward, thus breaking the C–surface bond. On the other hand, the formation of Ac involves the hydrogen shift from the central to terminal C atom, and the formation of a C=O double bond, thus partially breaking both C– and O–surface bonds.

The comparison between the two TS's described above, indicates that the C– and O–surface bond strengths in the OMC contribute differently to the two activation energies. In particular, the O–surface bond strength in the OMC affects the activation energy for Ac formation, while it does not for EO formation. Indeed, the stronger is this bond, the higher would be the energy cost to partially detach O during the Ac formation, thus increasing the corresponding energy barrier. As for the EO formation, not significant change would be observed for the activation energy, since going from OMC to TS^{EO} the O–surface bond is not broken. On the other side, the C–surface bond strength in the OMC affects both activation energies, since TS^{EO} and TS^{Ac} are characterized by a full and partial breaking of the C–surface bond in the OMC, respectively. Therefore, enhancing this bond would increase both barriers, having a stronger effect on the EO formation, where the C

atom is fully detached.

In summary, we believe that the selectivity is partially related to the differential bonding affinity of a catalyst toward C– and O–atom in the OMC. In particular, we expect that the stronger is the OMC's O–surface bond with respect to C–surface bond, the higher would be the increase of the activation energy for the Ac formation with respect to the EO, and the more selective the substrate will be toward EO formation.

In order to use our observation in the prediction of catalyst's selectivity, these C– and O–surface bond contributions in OMC–surface interaction must be explicitly quantified. As schematically shown in Fig. 4.4, we propose to approximate the C– and O–surface bond contributions in the OMC by the interaction of methyl (CH_3) and methoxy (CH_3O) with the surface, respectively. In this approximation, the strenght of the C– and O–surface bonds are measured by the adsorption energy of CH_3, $E_{\rm ads}^{\rm CH_3}$, and CH_3O, $E_{\rm ads}^{\rm CH_3O}$, respectively. These quantities are calculated from the energy of CH_3 and CH_3O species on the surface, in adsorption configurations which are obtained optimizing methyl and methoxy structures starting from geometries as close as possible to their position in the corresponding OMC. In particular, during the structural optimization one has to pay attention to avoid new contributions to the interaction of CH_3 and CH_3O with the surface, which are not present in the OMC. For instance, methyl may form a peculiar three-center C-H-metal bond, usually referred to as an agostic bond, which is not present in our calculated OMC structures.

4.3 Identification of an indicator for the catalyst selectivity

On the basis of the structural characteristics of the two TS's described in the previous section, we postulate that the activation energies for Ac and EO formation from the OMC can be approximated as follows:

$$E_{\rm Ac}^{*} \simeq \left[\alpha_1 E_{\rm ads}^{\rm CH_3O} + \beta E_{\rm ads}^{\rm CH_3} + \gamma_1 E_{\rm ads}^{\rm Ac}\right] - E_{\rm ads}^{\rm OMC} + C_1, \qquad (4.1)$$

$$E_{\rm EO}^{*} \simeq \left[\alpha_2 E_{\rm ads}^{\rm CH_3O} + \gamma_2 E_{\rm ads}^{\rm EO}\right] - E_{\rm ads}^{\rm OMC} + C_2, \qquad (4.2)$$

where C_1 and C_2 are additive constants.

Both activation energies are written as the energy difference between TS and IS. The energy of the IS is not approximated in the above equations, and it is given by $E_{\mathrm{ads}}^{\mathrm{OMC}}$. As for the energy of the TS, an approximated expression is given and different terms, which contribute differently, are present. In particular, $E_{\mathrm{ads}}^{\mathrm{Ac(EO)}}$ accounts for the standard BEP contribution to the Ac (EO) formation, according to which the activation energy depends linearly on the energy of the final states. Beside the BEP term, in eq. (4.1) for E_{Ac}^{*} the first and second terms account for the energy of the O– and C–metal bonds, which are partially attached in $\mathrm{TS}^{\mathrm{Ac}}$. Instead, in eq. (4.2) for E_{EO}^{*} only the term accounting for the energy of O–metal bond is present, since in $\mathrm{TS}^{\mathrm{EO}}$ the OMC's C–metal bond is fully broken, and C is detached.

A fit to the data from the main reactions considered in this work (listed in Tab. 4.1) gives:

$$E_{\mathrm{Ac}}^{*} \simeq \left[0.17E_{\mathrm{ads}}^{\mathrm{CH_3O}} + 0.30E_{\mathrm{ads}}^{\mathrm{CH_3}} + 0.52E_{\mathrm{ads}}^{\mathrm{Ac}}\right] - E_{\mathrm{ads}}^{\mathrm{OMC}} + 1.58, \quad (4.3)$$

$$E_{\mathrm{EO}}^{*} \simeq \left[0.59E_{\mathrm{ads}}^{\mathrm{CH_3O}} + 0.56E_{\mathrm{ads}}^{\mathrm{EO}}\right] - E_{\mathrm{ads}}^{\mathrm{OMC}} + 2.01. \quad (4.4)$$

Eqs. (4.3) and (4.4) for E_{Ac}^{*} and E_{EO}^{*} are shown in Fig. 4.5 (a) and (b), respectively.

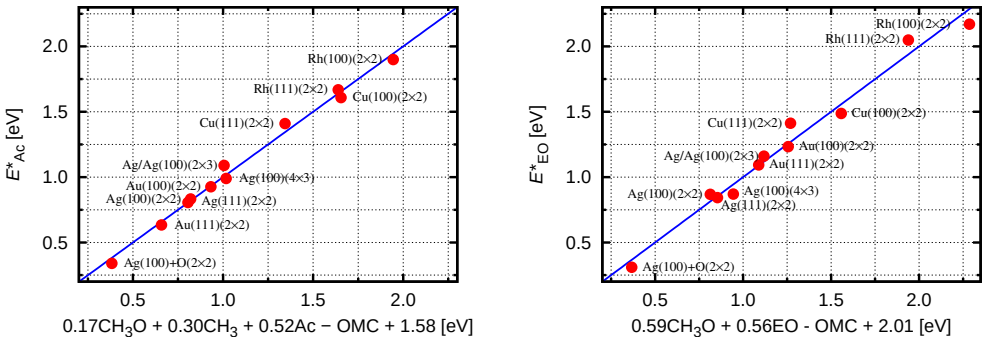

(a) (b)

Figure 4.5: *Fit by eq. (4.3) for E_{Ac}^{*} (a), and by eq. (4.4) for E_{EO}^{*} (b). The rms error is 0.04 and 0.08 eV for (a) and (b), respectively, whereas the largest error is 0.08 and 0.14 eV for (a) and (b), respectively.*

A comparison between the fits from Fig. 4.1, where only BEP contribution is taken into account, and those from Fig. 4.5, where also the C– *vs.*

O–surface bond strenght has been included, shows that a substantial improvement has been achieved in describing both $E^*_{\rm Ac}$ and $E^*_{\rm EO}$. In particular, as for the EO formation, the rms (largest) error decreases from 0.18 (0.32) eV to 0.08 (0.14) eV.

The difference between eq. (4.3) and eq. (4.4) gives an approximation for ΔE^*, which at fixed temperature determines the selectivity, as:

$$\Delta E^* \simeq 0.30 E^{\rm CH_3}_{\rm ads} - 0.42 E^{\rm CH_3O}_{\rm ads} + 0.52 E^{\rm Ac}_{\rm ads} - 0.56 E^{\rm EO}_{\rm ads} - 0.43. \qquad (4.5)$$

Since the coefficients for the various contributions to ΔE^* are similar, we simplify the expression for ΔE^*, reducing the number of parameters, and merging all the contributions to a single one, as:

$$\Delta E^* \simeq \alpha \left[E^{\rm CH_3}_{\rm ads} - E^{\rm CH_3O}_{\rm ads} + E^{\rm Ac}_{\rm ads} - E^{\rm EO}_{\rm ads} \right] + C. \qquad (4.6)$$

From a fit to the data listed in Tab. 4.1, we conclude that to a very good approximation, one has:

$$\Delta E^* \simeq \ 0.39 [E^{\rm CH_3}_{\rm ads} - E^{\rm CH_3O}_{\rm ads} + E^{\rm Ac}_{\rm ads} - E^{\rm EO}_{\rm ads}] - 0.31. \qquad (4.7)$$

Indeed, the quality of the fit for ΔE^* by eq. (4.7) is the same as for a fit done keeping different coefficients for different contributions in ΔE^*.

The expression for ΔE^* as given in eq. (4.7) is a very important quantity. Indeed, it allows to predict the catalysts behaviour in terms of selectivity, without the need to identify the full reaction pathway and to calculate the activation energy, which is very expensive from computational point of view. For this reason, we will refer to this quantity as an indicator for the catalyst selectivity.

In Fig. 4.6 we compare the quality of the fit given by eq. (4.7) with that obtained from the simple BEP relation. Our indicator is able to estimate ΔE^* with an accuracy better than 0.1 eV (the rms and largest errors are 0.05 and 0.07 eV, respectively). Moreover, it shows that two contributions are equally important to determine ΔE^*: (1) the difference between the adsorption energies of CH_3 and CH_3O, representing the differential bonding affinity of the catalyst toward C– and O–surface bonds in the OMC, and (2) the difference between the adsorption energies of the two final states, Ac and EO, which accounts for the standard BEP contribution.

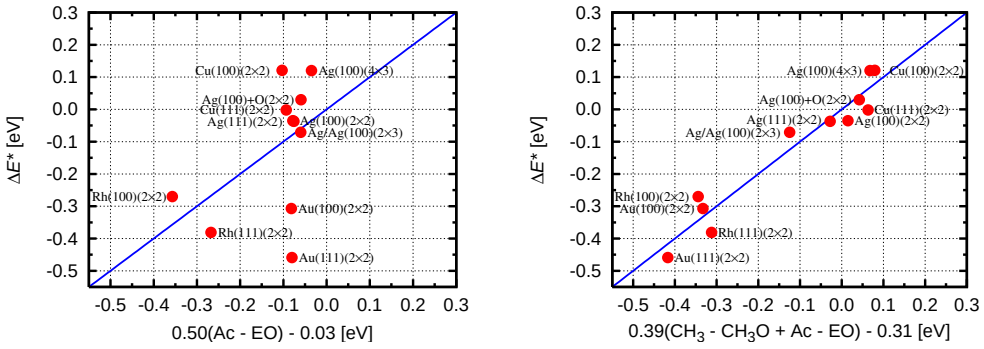

(a) (b)

Figure 4.6: *(a) BEP estimation of* ΔE^**:* $\Delta E^* \propto E_{ads}^{Ac} - E_{ads}^{EO}$*. The rms and the largest errors are 0.19 and 0.38 eV, respectively. (b) Fit of* ΔE^* *by eq. (4.7). The rms and the largest errors are 0.05 and 0.07 eV, respectively.*

4.4 Application of the indicator to Cu surface and Cu/Ag alloy

As discussed in chapter 3, Cu displays a higher selectivity (i.e. ΔE^* more positive) compared to Ag. This fact cannot be simply explained, as suggested by Torres et al. [43], in terms of a different character of the TS^{EO} on the two metal surfaces. In particular, the authors notice that TS^{EO} results to be of early-type (i.e. close to the initial state) on Ag, and of late-type (i.e. close to the final state) on Cu, which results to be more selective than Ag. This observation, together with Hammond postulate, makes them to conclude that the stronger is the OMC–surface interaction, the more favored the EO formation would be with respect to the Ac. Our calculations are at variance with this conclusion. For instance, the OMC adsorption energy on Rh(100) is stronger than on Cu(100), yet ΔE^* is -0.27 eV on Rh(100), lower than its value on Cu(100), 0.12 eV (see Tab. 4.1), meaning that Rh(100) is less selective than Cu(100). Our analysis shows instead that Cu has higher selectivity toward EO formation than the other IB metals because Cu displays the highest "relative" O– *vs.* C–surface bond strength in OMC. In particular, moving from Ag(100) to Cu(100) the $\left[E_{\mathrm{ads}}^{\mathrm{Ac}} - E_{\mathrm{ads}}^{\mathrm{EO}}\right]$ contribution decreases from -0.10 to -0.15 eV, while the $\left[E_{\mathrm{ads}}^{\mathrm{CH_3}} - E_{\mathrm{ads}}^{\mathrm{CH_3O}}\right]$ increases from

0.94 to 1.16 eV. According to our model, the C– *vs.* O–surface bond contribution determines the increase of ΔE^* from -0.04 to 0.12 eV moving from Ag(100) to Cu(100), accounting for the higher selectivity of Cu(100) with respect to Ag(100).

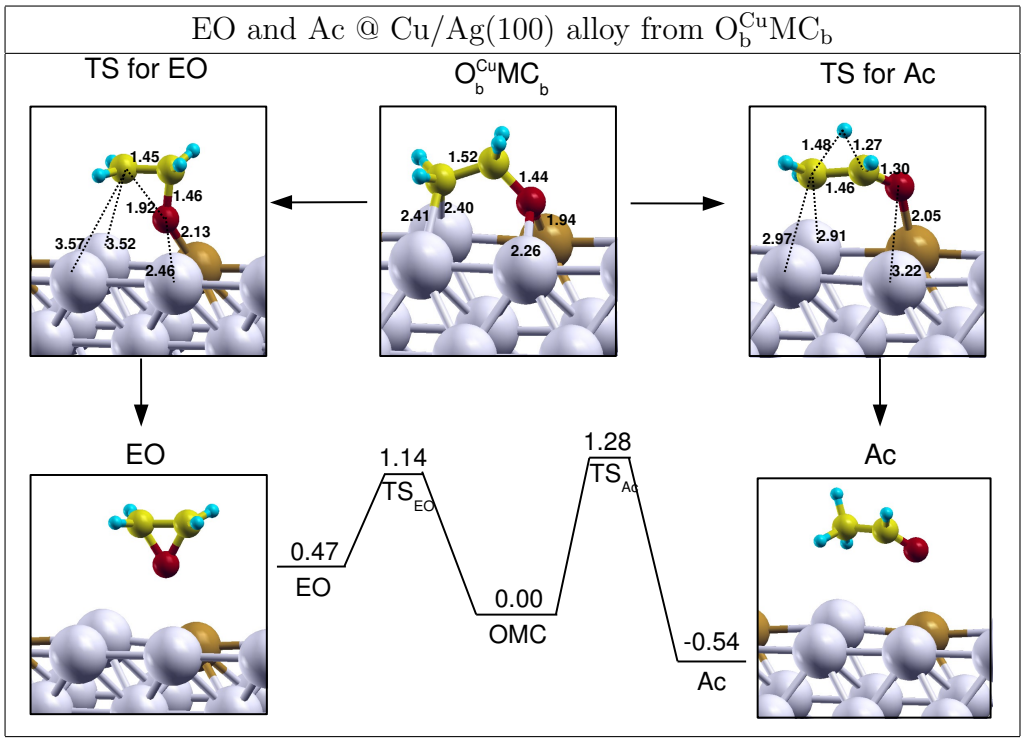

Figure 4.7: *$O_b^{Cu}MC_b$, TS's, EO and Ac on Cu/Ag(100) alloy. Reaction pathways are schematically rapresented. Distances are in Å and energies are in eV, measured with respect to OMC energy.*

Recently, it has been also suggested, based on DFT calculations, that Cu/Ag alloy displays higher selectivity towards EO than pure Ag [45, 46, 47]. Our simple model is able to explain very well why Cu/Ag alloy is more selective than pure Ag. We consider here a Cu/Ag(100) mixed surface, where an Ag atom in the (2×2) cell is replaced by a Cu atom. Cu/Ag surface with Cu concentration of 25% is a good model for the surfaces observed in experiments [46], where Ag catalyst with a Cu loading around 0.2% are used, which are estimated from XPS to have 1/4 ML of surface Cu atoms. In Fig. 4.7 we show the most stable identified OMC on such surface, and TS for both EO and Ac formation. Reaction pathways are schematically

represented. Activation energies and entalphy of reactions are reported, with respect to the OMC energy. In this $O_b^{Cu}MC_b$ configuration, the O atom is on bridge site and it binds to Cu and Ag atoms, while C atom is on bridge site between two Ag atoms. The $O_b^{Cu}MC_b$ adsorption energy is -0.57 eV, and it is higher than the adsorption energy on Ag(100), which is 0.05 eV. This energy difference is mainly due to the O–surface bond in the $O_b^{Cu}MC_b$, which is enhanced by the presence of the more reactive Cu atom. Indeed, according to our picture, going from Ag(100) to our model of Cu/Ag(100), the $E_{ads}^{CH_3O}$ goes from -1.97 to -2.25 eV, while $E_{ads}^{CH_3}$ slightly decreases from -1.03 to -1.05 eV. The adsorption energy of Ac does not change with respect to Ag(100), while the adsorption energy of EO goes from 0.01 to -0.07 eV. The activation energy for EO and Ac formation from $O_b^{Cu}MC_b$ of Fig. 4.7 is 1.14 and 1.28 eV, respectively. Both barriers are higher than the corresponding values on Ag(100), and this is due to the stronger OMC interaction with the surface. However this effect is higher for Ac formation, in agreement with our hypothesis that the stronger is the O–surface bond in the OMC with respect to its C–surface bond, the higher would be the activation energy for Ac with respect to EO. In summary, starting from the most stable $O_b^{Cu}MC_b$, with O atom bound to Cu atom, ΔE^* increases from -0.04 to 0.14 eV. This is due to the $\left[E_{ads}^{CH_3} - E_{ads}^{CH_3O}\right]$ contribution in eq. (4.7), which increases from 0.94 to 1.20 eV, while the BEP contribution increases only from -0.10 to 0.01 eV.

In order to further verify our hypothesis, we considered another, less stable, OMC on Cu/Ag(100) alloy, labelled $O_bMC_t^{Cu}$, where the O is on bridge site between two Ag atoms, while C is on top of a Cu atom. In Fig. 4.8 we show this OMC, and TS for both EO and Ac formation. The $O_bMC_t^{Cu}$ adsorption energy is -0.40 eV, and the energy difference with respect to the O_bMC_b on Ag(100) surface is now due to the C–surface bond, which is enhanced by the interaction with the more reactive Cu atom. The activation energy for EO and Ac formation is 1.21 and 1.12 eV, respectively. Both barriers are higher than on Ag(100), but in this case the effect is stronger for EO formation. Again, this can be easily explained by our model: the C–surface bond in the $O_bMC_t^{Cu}$ is fully broken during EO formation, while it breaks only partially during Ac formation. Thus, enhancing the C–surface

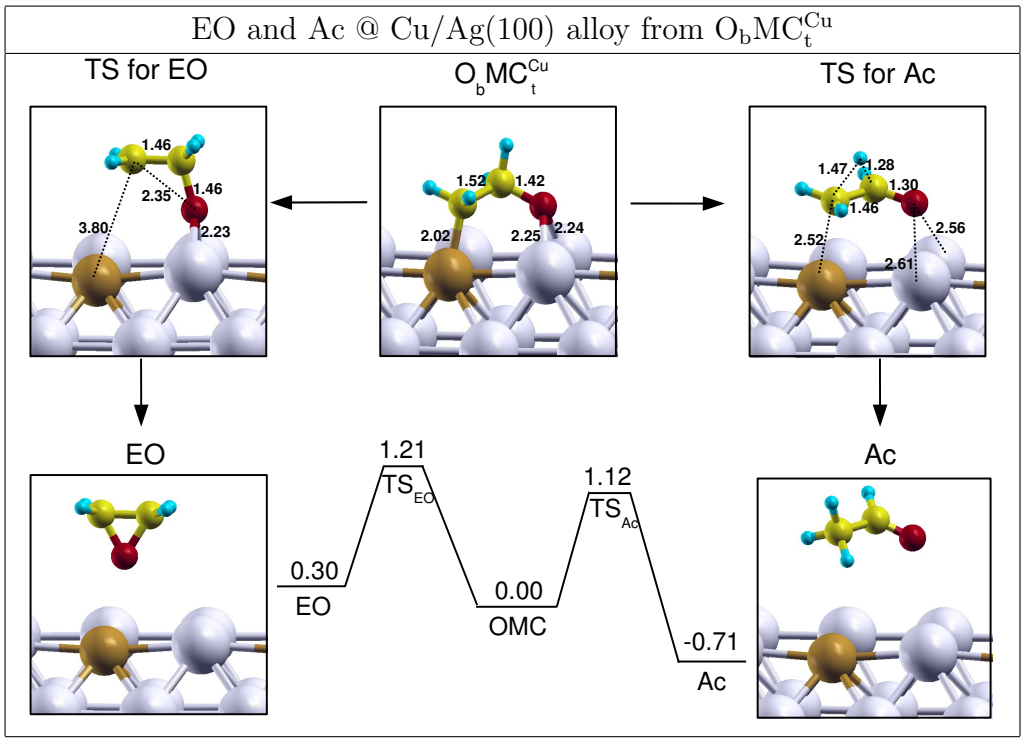

Figure 4.8: *$O_bMC_t^{Cu}$, TS's, EO and Ac on Cu/Ag(100) alloy. Reaction pathways are schematically rapresented. Distances are in Å and energies are in eV, measured with respect to OMC energy.*

bond in the OMC makes the EO formation more unfavored than Ac. Indeed, starting from $O_bMC_t^{Cu}$, ΔE^* decreases to -0.09 eV, which means a lower selectivity towards EO.

In summary, in this chapter we proposed a simple indicator, eq. (4.7), for the catalyst selectivity toward EO, which allows to identify important factors determining the improved selectivity of Cu and Cu/Ag alloy, with respect to Ag. In particular, we suggest that the stronger is the O–metal bond in the OMC, with respect to the C–metal bond, the higher is the selectivity toward EO. Therefore, selectivity is in part determined by a peculiar electronic effect, which is related to the differential bonding affinity of a catalyst toward C– and O–atom in the OMC. We believe that the importance of the differential bonding affinity of a catalyst toward the different atoms of a molecule adsorbed on it, is a general concept, not limited to the ethylene epoxidation reaction shown here, and could play an important role in determining

selectivity also in other branching reactions.

Chapter 5

The role of Cl as promoter in the ethylene epoxidation

In this chapter the role of Cl as promoter in the ethylene epoxidation is addressed. In particular, we investigated the adsorption of Cl on silver surfaces, as a function of Cl coverage, and the feasibility for Cl atoms to be incorporated subsurface. According to our results, Cl adsorption on Ag subsurface sites becomes stable at high coverage ($\Theta \approx 3/4$ ML).

On the basis of these findings, we conclude that the role of subsurface Cl as promoter in the ethylene epoxidation should be revised, and our preliminary results show that on-surface Cl on Ag(111) improves the selectivity toward EO, with respect to unpromoted Ag.

5.1 Chlorine adsorption on silver surfaces

In the ethylene epoxidation reaction, a significant improvement in selectivity toward EO formation, up to 80%, is achieved in presence of promoters, such as Cl [1, 2, 30]. Due to the importance of Cl in the ethylene epoxidation reaction, the interaction of Cl with Ag surfaces have been widely studied by numerical simulations [32, 33] and experiments [34, 35, 36, 37, 38]. Nevertheless, its role as promoter remains still controversial. In particular, experimental studies, where atomic Cl is adsorbed on Ag surface, have shown that selectivity toward EO increases even at low Cl coverage, while at high

coverage the catalyst activity drops to zero [1, 30]. Moreover, it is often assumed that Cl is adsorbed subsurface, and on the basis of this assumption various explanations of its role as promoter in EO synthesis have been suggested [2, 31]. However, the computational studies deal mainly with on-surface Cl adsorption. Therefore, we addressed in this work the feasibility of Cl to adsorb subsurface, to shed some light on the mechanisms for Cl incorporation below the surface. In particular, we investigated the on-surface, subsurface and substitutional adsorption of atomic Cl on Ag(111), which is the majority surface exposed on metal particles. Our main purpose is to determine the critical coverage at which Cl atoms start to adsorb below the surface. We also addressed how the presence of low coordinated defects affects the adsorption of Cl into subsurface. For this purpose, we deliberately chose a very open surface, such as Ag(210), which consists of 1-atom row wide (110) and (100) nanofacets.

5.1.1 Cl adsorption on Ag(111)

In this section we present results about different Cl adsorption geometries on Ag(111) surface, as a function of Cl coverage. We considered pure on-surface, subsurface, and substitutional adsorption as well as the mixed on-surface+subsurface and on-surface+substitutional adsorption. Identified geometries and corresponding chemisorption energies per Cl atom are collected in Figs. 5.1–5.7 and Tabs. 5.1–5.3 and 5.4, where structural parameters are also reported.

The average chemisorption energy for dissociative adsorption of chlorine is calculated as:

$$E_{\text{chem}} = \frac{1}{n}\left[E_{\text{Cl/Ag}} - (E_{\text{Ag}} + \frac{n}{2}E_{\text{Cl}_2})\right], \tag{5.1}$$

where n is total number of Cl atoms adsorbed on Ag surface, $E_{\text{Cl/Ag}}$ is the total energy of adsorption system, E_{Ag} is the total energy of clean Ag surface, and E_{Cl_2} is the energy of the Cl_2 gas-phase molecule.

To facilitate the characterization of Cl/Ag structures, we define a few structural parameters. Upon Cl adsorption, the interlayer distance between the surface and subsurface Ag layers, d_{12}, is calculated as the difference in

height between the average plane of surface Ag atoms and the average plane of subsurface Ag atoms. The relaxation of the surface layer, Δd_{12}, is the difference between the d_{12} and the ideal bulk interlayer spacing.

Under several circumstances, the vertical corrugation of surface Ag atoms can be substantial. As an approximate measure of the corrugation, we define the parameter $h_{\mathrm{Ag}}^{\mathrm{surf}}$ as the difference in height between the highest and lowest Ag atom in the surface layer. The distance between Cl and Ag atoms will be designated as follows: $d_{\mathrm{Cl-Ag}}^{\mathrm{on}}$ ($d_{\mathrm{Cl-Ag}}^{\mathrm{sub}}$, $d_{\mathrm{Cl-Ag}}^{\mathrm{subst}}$) is the average distance between the on-surface (subsurface, substitutional) Cl atoms and nearest neighbor Ag atoms. $\Delta z_{\mathrm{Cl-Ag}}^{\mathrm{on}}$ ($\Delta z_{\mathrm{Cl-Ag}}^{\mathrm{sub}}$, $\Delta z_{\mathrm{Cl-Ag}}^{\mathrm{subst}}$) is the difference between the average height of on-surface (subsurface, substitutional) Cl atoms and the average height of surface silver layer. Other more obvious parameters will be explained when used.

When considering more than one Cl atom per (2×2) supercell, there are two different types of the same site, depending on the relative distance between Cl atoms (for details on adsorption sites see Appendix A). We refer to adjacent sites with label 1nn (first nearest neighbour), and to the second nearest neighbour sites with label 2nn. Unless specified otherwise, we always considered 2nn sites, since we expect a repulsive Cl-Cl interaction, because the Cl display a negative charge (about $0.5e$, as calculated for 1/4 ML).

On-surface adsorption. The results about the on-surface Cl adsorption are reported in Tab. 5.1. The relative stability of high symmetry on-surface sites at 1/4 ML follows the order fcc ≈ hcp > bridge > top. However, at this coverage, the bridge and top sites are not local minima (the corresponding E_{chem} values have been obtained from constrained optimizations for comparison purposes). The difference between chemisorption energies on hollow and bridge sites is quite small, below 0.1 eV, indicating a low diffusion barrier.

At coverage of 1/2 ML, we identified several hexagonal on-surface configurations and some of them are shown in Fig. 5.1. The most stable configuration is the honeycomb structure shown in Fig. 5.1(a), where Cl atoms are adsorbed into fcc and hcp sites. The average chemisorption energy for this structure is −1.13 eV. Our results at coverage up to 1/2 ML are in reasonable agreement with previous GGA studies [32, 33].

Θ_{on} (ML)	Sites	Shown in Figure	E_{chem} (eV)	Δz^{on}_{Cl-Ag} (Å)	d^{on}_{Cl-Ag} (Å)	h_{Ag} (Å)	Δd_{12} (%)
1/16	fcc	-	**−1.53**	2.01	2.66	0.05	−0.9
1/9	fcc	-	**−1.58**	2.00	2.65	0.04	−1.6
1/4	fcc	-	**−1.48**	2.04	2.66	0.10	−1.6
	hcp	-	−1.47	2.04	2.66	0.06	−1.6
	bridge	-	−1.41	2.10	2.58	0.05	−1.6
	top	-	−1.07	2.36	2.40	0.06	−1.6
1/3	fcc	-	**−1.52**	1.98	2.64	0.00	−1.4
	hcp	-	−1.51	1.99	2.64	0.00	−1.2
1/2	fcc/hcp	5.1(a)	**−1.13**	2.01	2.62	0.07	−1.4
	off-fcc/off-hcp	5.1(b)	−1.05	1.99	2.68	0.37	0.4
	fcc/top	5.1(c)	−1.06	2.07	2.50	0.17	−0.9
	hcp/top	5.1(d)	−1.04	2.07	2.52	0.20	−1.2
2/3	fcc/fcc	5.2(a)	**−0.70**	1.96	2.61	0.00	−1.2
3/4	fcc/fcc/hcp	5.2(b)	**−0.75**	2.07	2.54	0.10	−1.1

Table 5.1: *On-surface Cl configurations as a function of coverage,* Θ_{on}*, on Ag(111). Structural parameters and chemisorption energies,* E_{chem}*, in eV/Cl-atom, are reported. For each coverage,* E_{chem} *corresponding to the most stable configuration is reported in bold font. Parameters are defined at the beginning of section 5.1.1. For pure Ag(111)* $\Delta d_{12} = -0.7\%$*.*

By increasing Cl coverage to 2/3 ML, the most stable identified geometry is the honeycomb structure shown in Fig. 5.2(a), where Cl atoms are adsorbed on 1nn fcc sites with an average chemisorption energy of −0.70 eV. A hexagonal adsorbate configuration is preserved even at the larger coverage of 3/4 ML: the most stable identified structure is shown Fig. 5.2(b) with an average chemisorption energy of −0.75 eV. This structure is composed of Cl atoms adsorbed on 2nn fcc and hcp sites forming the structure of Fig. 5.1(a), with an additional Cl atom adsorbed on the top site at the center of the hexagon, so as to minimize the repulsive lateral interaction.

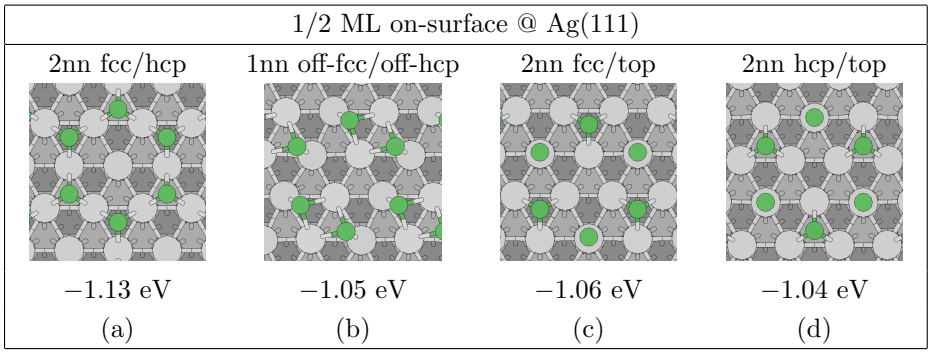

Figure 5.1: *Identified on-surface Cl adsorption configurations on Ag(111), at a total coverage of 1/2 ML, with corresponding average chemisorption energies, E_{chem}. All these structures display a honeycomb pattern. We identified also other structures, which are low-symmetry variants of those presented here.*

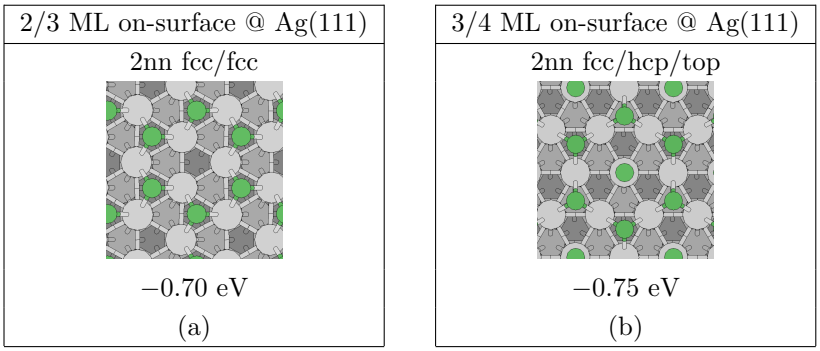

Figure 5.2: *On-surface Cl configurations on Ag(111), at 2/3 ML (a) and 3/4 ML (b), with corresponding average chemisorption energies, E_{chem}.*

Subsurface adsorption. The results about subsurface Cl adsorption on Ag(111) are reported in Tab. 5.2. At low Cl coverage ($\Theta = 1/4$ ML) pure subsurface adsorption is highly disfavored with respect to on-surface adsorption, and it results to be highly endothermic. This endothermicity can be attributed to large distortion of the surface: subsurface Cl atoms push up substantially top silver layer (Δd_{12} and in some cases also h_{Ag} are very high) so as to break the Ag–Ag bonds between the surface and subsurface layer.

By increasing the coverage to 1/3 ML, adsorption into tetra–1 sites remains endothermic, while adsorption into octa and tetra–2 sites is athermic. At this subsurface Cl coverage, Δd_{12} is still very high, while for Cl adsorption

Θ_{sub} (ML)	Sites	E_{chem} (eV)	$\Delta z^{\text{sub}}_{\text{Cl-Ag}}$ (Å)	$d^{\text{sub}}_{\text{Cl-Ag}}$ (Å)	h_{Ag} (Å)	Δd_{12} (%)
1/4	octa	0.76	−2.72	2.96	0.11	101.7
	tetra–1	1.51	−1.45	2.57	1.53	57.0
	tetra–2	**0.75**	−3.06	2.75	0.29	115.5
1/3	octa	0.02	−2.86	3.02	0.00	106.5
	tetra–1	0.22	−2.41	2.88	0.00	106.7
	tetra–2	**0.01**	−2.99	2.75	0.18	110.6
1/2	octa/tetra–2	**−0.17**	−2.91	2.91	0.18	108.8
3/4	octa/tetra–1/tetra–2	**−0.40**	−2.28	2.63	0.07	80.7

Table 5.2: *Subsurface Cl configurations as a function of coverage, Θ_{sub}, on Ag(111). Strutural parameters and chemisorption energies, E_{chem}, in eV/Cl-atom, are reported. For each coverage, E_{chem} corresponding to the most stable configuration is reported in bold font. Parameters are defined at the beginning of section 5.1.1. For pure Ag(111) $\Delta d_{12} = -0.7\%$.*

on octa and tetra–1 sites there is no surface corrugation, due to symmetry imposed by the supercell. These numbers indicate that the subsurface adsorption becomes more stable with increasing coverage. In order to establish a trend, we performed also few calculations at 1/2 and 3/4 ML coverage. At 1/2 ML we considered a geometry with one Cl atom in octa site and the other one in the 2nn tetra–2 site. We choosed this configuration because octa and tetra–2 are the most stable subsurface sites at lower coverage. At 3/4 ML we considered a configuration with the three Cl atoms located into octa, tetra–1, and tetra–2 subsurface sites. The resulting average chemisorption energies, which are −0.17 and −0.40 eV at 1/2 and 3/4 ML, respectively, show that subsurface adsorption at high coverage become exothermic, in agreement with the trend indicated above.

Mixed on-surface+subsurface adsorption. The results about the mixed on-surface+subsurface Cl adsorption are reported in Tab. 5.3. During the geometry optimization, for some of these initial configurations subsurface Cl

Θ_{total} (ML)	Θ_{on} (ML)	Θ_{sub} (ML)	Initial Conf.	Final Conf.	E_{chem} (eV)	$\Theta^{\text{f}}_{\text{on}}$ (ML)	$\Theta^{\text{f}}_{\text{sub}}$ (ML)	$\Delta z^{\text{on}}_{\text{Cl-Ag}}$ (Å)	$\Delta z^{\text{sub}}_{\text{Cl-Ag}}$ (Å)	$d^{\text{on}}_{\text{Cl-Ag}}$ (Å)	$d^{\text{sub}}_{\text{Cl-Ag}}$ (Å)	h_{Ag} (Å)	Δd_{12} (%)
1/2	1/4	1/4	fcc/tetra–1	5.3(b)	−0.61	1/4	1/4	-	-	-	-	2.30	42.8
			fcc/tetra–2	5.3(c)	−0.42	0	1/2	-	-	-	-	3.25	31.3
			hcp/octa	5.3(d)	−0.61	1/4	1/4	-	-	-	-	2.31	42.5
			hcp/tetra–2	5.3(f)	**−0.86**			-	-	-	-	2.32	20.6
2/3	1/3	1/3	fcc/octa	5.4(a)	−0.44	1/3	1/3	1.95	−2.43	2.63	2.98	0.00	94.2
			fcc/tetra–1	5.4(b)	**−0.47**	1/3	1/3	2.09	−2.34	2.48	2.77	1.22	101.3
			fcc/tetra–2	5.4(c)	−0.46	1/3	1/3	1.94	−2.98	2.64	3.64	0.54	113.2
3/4	1/2	1/4	fcc/hcp/octa	5.5(a)	−0.87	0	3/4	-	-	-	-	2.85	28.2
			fcc/hcp/tetra–1	5.5(b)	−0.87	1/4	1/2	-	-	-	-	2.47	23.8
			fcc/hcp/tetra–2	5.5(c)	−0.87	0	3/4	-	-	-	-	2.86	28.0
			fcc/fcc/octa	5.5(d)	**−0.91**	1/4	1/2	-	-	-	-	3.66	67.3
			fcc/fcc/tetra–1	5.5(e)	−0.87	0	3/4	-	-	-	-	2.79	27.6
			fcc/fcc/tetra–2	5.5(f)	−0.74	1/4	1/2	-	-	-	-	3.40	32.8
			hcp/hcp/ octa	5.6(a)	−0.89	1/4	1/2	-	-	-	-	3.15	59.1
			hcp/hcp/tetra–1	5.6(b)	−0.89	1/4	1/2	-	-	-	-	3.17	52.1
			hcp/hcp/tetra–2	5.6(c)	−0.87	0	3/4	-	-	-	-	2.82	27.9
3/4	1/4	1/2	fcc/tetra–1/tetra–2	5.6(d)	−0.44	1/4	1/2	2.03	−2.65	2.61	2.74	0.36	107.5
			hcp/octa/tetra–2	5.6(e)	**−0.46**	1/4	1/2	2.05	−3.27	2.58	3.05	0.75	124.1

Table 5.3: *Mixed on-surface+subsurface Cl configurations as a function of Cl coverage, on Ag(111). Chemisorption energies, E_{chem}, in eV/Cl-atom, are reported. For each coverage, E_{chem} corresponding to the most stable configuration is reported in bold font. Label "Initial Conf." refers to Cl configuration before the structural relaxation, whereas "Final Conf." refers to figure where relaxed configurations is shown. $\Theta^{\text{f}}_{\text{on}}$ ($\Theta^{\text{f}}_{\text{sub}}$) is the coverage of on-surface (subsurface) Cl atoms in the relaxed configuration. Other parameters are defined at the beginning of section 5.1.1. For highly reconstructed structures the evaluation of $\Delta z_{\text{Cl-Ag}}$ and $d_{\text{Cl-Ag}}$ becomes difficult, due to a substantial corrugation of the first two surface layers. For these structures, the two quantities are omitted, and moreover, the $\Theta^{\text{f}}_{\text{on}}$ and $\Theta^{\text{f}}_{\text{sub}}$ are evaluated with respect to the uppermost Ag atom.*

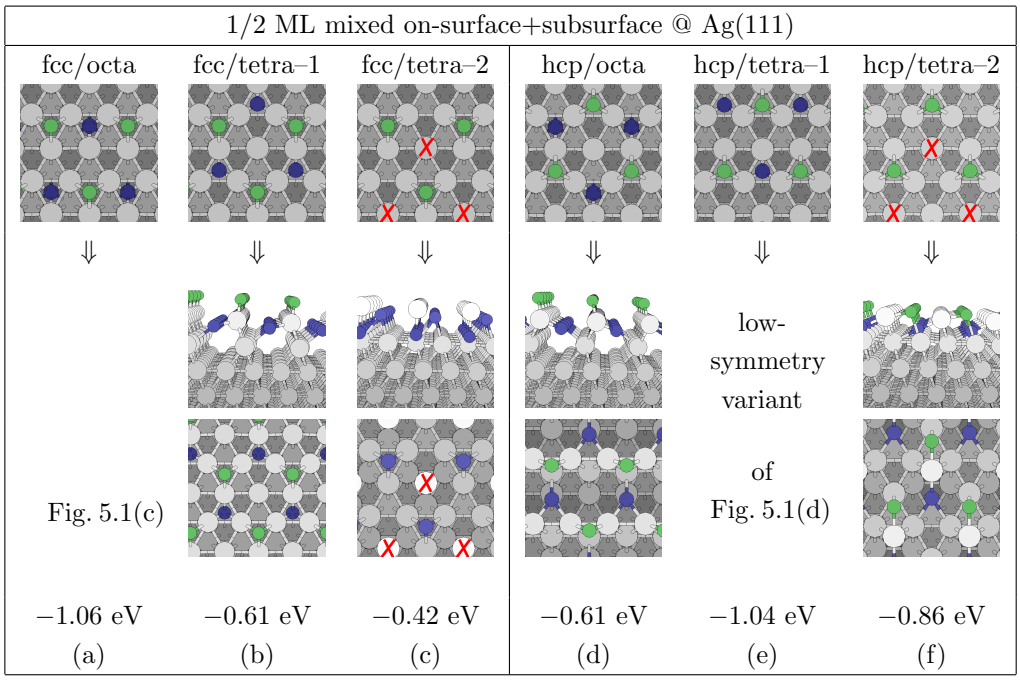

Figure 5.3: *Mixed on-surface+subsurface Cl configurations on Ag(111) at a total coverage of 1/2 ML. Top row: initial configurations; two bottom rows: optimized configurations from side and top view. Corresponding average chemisorption energies are also reported. Tetra–2 sites are located below Ag atoms marked with red cross (×). Green spheres: on-surface Cl atoms. Blue spheres: Cl atoms below the uppermost Ag atoms. During the geometry optimization of the initial fcc/octa and hcp/tetra–1 structures shown in (a) and (e), the subsurface Cl migrates above the surface.*

atoms are shifted on-surface, whereas others structures result in a large restructuring of the surface, such as the formation of steps and Ag adatoms. The relaxation is therefore so substantial that optimized structures have very little or no resemblance with initial Cl configurations. Nevertheless, to facilitate the discussion, in Tab. 5.3 we name all configurations according to their initial configurations, and in Figs. 5.3, 5.4, 5.5 and 5.6 initial (top row) and optimized (two bottom rows, side and top view) configurations are reported. On-surface Cl atoms are green, whereas Cl atoms below the uppermost Ag atoms are blue. Tetra–2 sites are located below Ag atoms marked with red cross (×).

The lowest coverage at which we investigated mixed on-surface+subsurface adsorption of Cl is 1/2 ML: this corresponds to one on-surface and one subsurface Cl atom per (2×2) supercell. At this coverage, we considered all six combinations with the on-surface Cl atom located in the most stable fcc and hcp sites, and the subsurface Cl atom into 2nn tetra–1, tetra–2, and octa sites (see Fig. 5.3). Relaxation of fcc/octa and hcp/tetra–1 configurations results in pure on-surface Cl structures. In particular, the fcc/octa structure after geometry optimization coincides with the fcc/top structure shown in Fig. 5.1(c), whereas the optimized hcp/tetra–1 has an average chemisorption energy of −1.04 eV, and it is a low-symmetry variant of configurations shown in Fig. 5.1(d). For other structures the relaxation results in mixed on-surface+subsurface Cl configurations. The most stable is the hcp/tetra–2 structure (Fig. 5.4(f)) with an average chemisorption energy of −0.86 eV. The least stable mixed configuration is the fcc/tetra–2 (Fig. 5.4(c)) with E_{chem} of −0.42 eV. In this structure the Cl atom initially located in the tetra–2 site, pushes up the surface Ag atom so as to form an Ag ad-atom above itself.

At 2/3 ML we considered configurations with one Cl atom in fcc site, and the other in octa, tetra–1, or tetra–2 subsurface sites. The three resulting configurations are shown in Figs. 5.4(a), (b) and (c), respectively. Due to $(\sqrt{3}\times\sqrt{3}R30^\circ)$ supercell geometry, configurations fcc/tetra–1 and fcc/tetra–2 can only be 1nn. In the final configurations of these three mixed on-surface+subsurface structures (Figs. 5.4(a), (b) and (c), two bottom rows) the top Ag layer is substantially shifted up due to subsurface Cl atoms. All the three resulting structures display similar average chemisorption energies.

At coverage of 3/4 ML we considered initial configurations with 1/2 ML of on-surface and 1/4 ML of subsurface Cl. This choice is suggested by the fact that at 1/2 ML of coverage pure on-surface adsorption is the most stable. In particular, we investigated on-surface structures involving 2nn fcc/hcp, 1nn fcc/fcc, and 1nn hcp/hcp sites, combined with the octa, tetra–1, and tetra–2 subsurface sites. Since the number of possible combinations is too large, we explored nine configurations (shown in Figs. 5.5, and 5.6 (a)–(c), top row), chosen such that the subsurface Cl is as far as possible from the two on-surface Cl atoms in the initial structure. Relaxation of these configurations involves large restructuring of surface, and optimized structures are shown

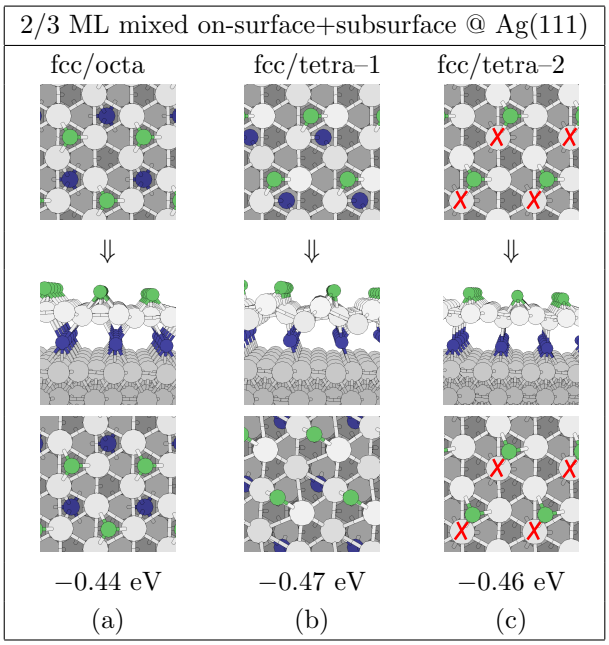

Figure 5.4: *Mixed on-surface+subsurface Cl configurations on Ag(111) at a total coverage of 2/3 ML. Top row: initial configurations; two bottom rows: optimized configurations from side and top view. Corresponding average chemisorption energies are also reported. Tetra–2 sites are located below Ag atoms marked with red cross (×). Green spheres: on-surface Cl atoms. Blue spheres: Cl atoms below the uppermost Ag atoms.*

in Fig. 5.5 and 5.6 (a)–(c), two bottom rows. The average chemisorption energy is about −0.90 eV, in the most stable structures. Therefore these configurations are more stable than the one shown in Fig. 5.2(b), which is the most stable identified purely on-surface configuration at 3/4 ML, indicating that at this coverage the mixed on-surface+subsurface adsorption is more stable than the pure on-surface one.

Interestingly, the optimized structures shown in Fig. 5.5 (a), (c), (e), and 5.6 (c), involve larger amount of subsurface Cl than anticipated above. In particular, in these structures all Cl atoms are below the uppermost Ag atoms, whereas in the others only 1/4 ML of on-surface Cl is present. For this reason we also investigated two structures with majority of subsurface Cl in the initial configuration, i.e., 1/2 ML of subsurface and 1/4 ML of on-surface Cl atoms. In particular we considered fcc/tetra–1/tetra–2 and

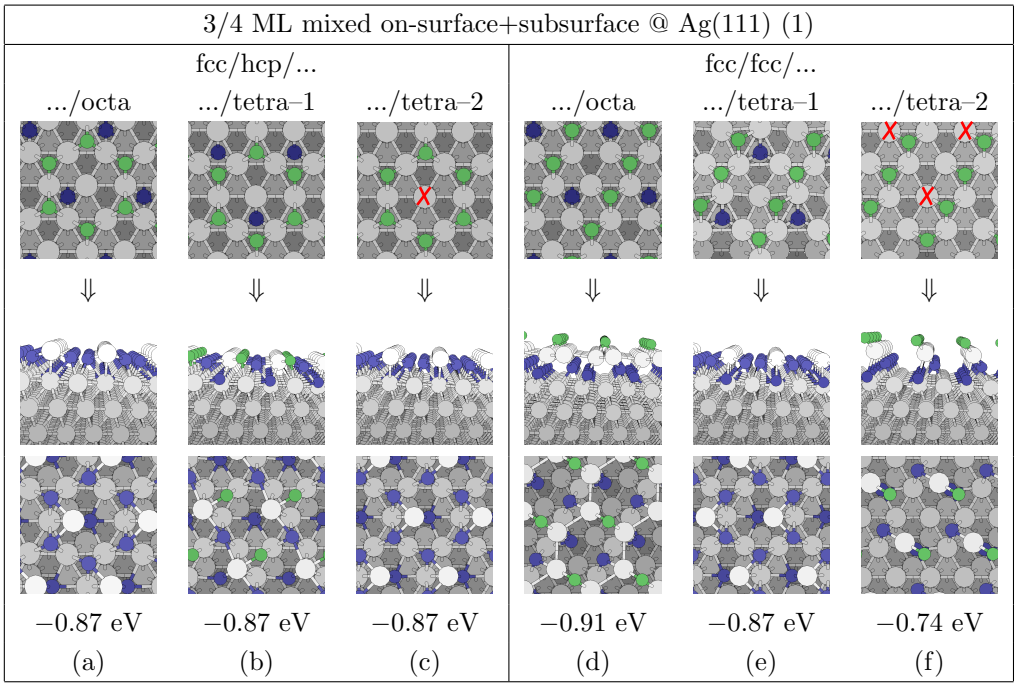

Figure 5.5: *Mixed on-surface+subsurface Cl configurations on Ag(111) at a total coverage of 3/4 ML. Top row: initial configurations; two bottom rows: optimized configurations from side and top view. Corresponding average chemisorption energies are also reported. Tetra–2 sites are located below Ag atoms marked with red cross (×). Green spheres: on-surface Cl atoms. Blue spheres: Cl atoms below the uppermost Ag atoms.*

hcp/octa/tetra–2 structures, because in these structures Cl atoms are as far apart as possible (Figs. 5.6(d) and (e), top row, respectively). In the resulting optimized structures, the on-surface and sub-surface coverage is unchanged (Figs. 5.6(d) and (e), two bottom rows, respectively), and the average chemisorption energy is −0.44 and −0.46 eV, respectively. Hence these two structures are less stable than the other mixed configurations at 3/4 ML, because the surface Ag layer is substantially less corrugated, but completely detached from the subsurface Ag layer: the two layers are linked together only trough the subsurface Cl atoms.

According to our results for mixed on-surface+subsurface configurations, large amount of adsorbed Cl ($\Theta \geq 1/2$ ML) induces large surface restructuring, which is in agreement with experimental findings [1, 36, 37, 38]. Based

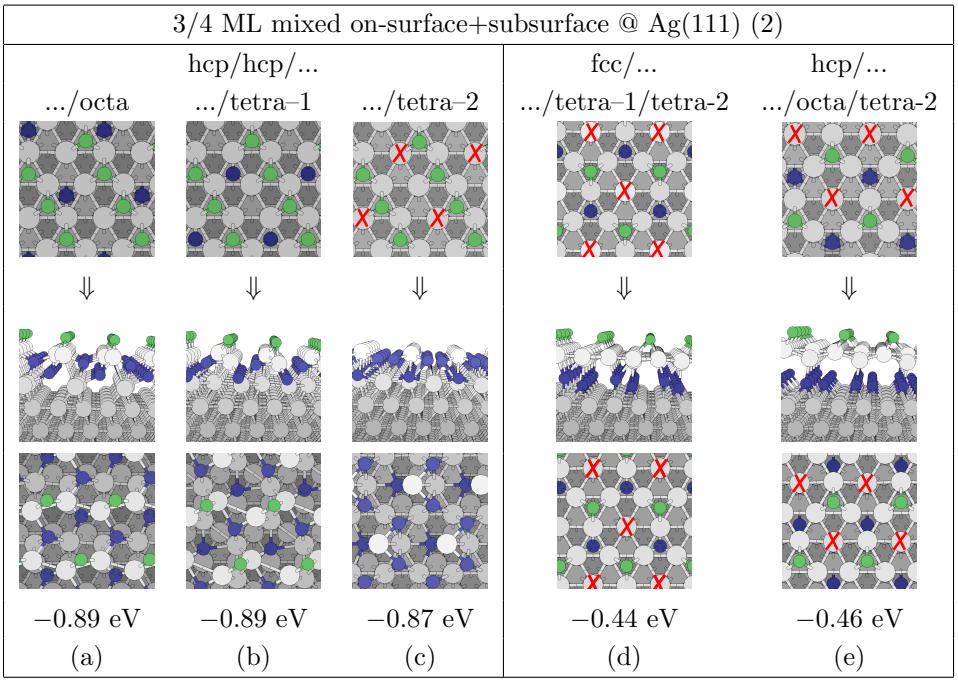

Figure 5.6: *Mixed on-surface+subsurface Cl configurations on Ag(111) at a total coverage of 3/4 ML. Top row: initial configurations; two bottom rows: optimized configurations from side and top. Corresponding average chemisorption energies are also reported. Tetra–2 sites are located below Ag atoms marked with red cross (×). Green spheres: on-surface Cl atoms. Blue spheres: Cl atoms below uppermost Ag atoms.*

on our results presented in this section, we note that relaxations of initial mixed on-surface+subsurface configurations produce three types of adsorption structures: (1) Cl atoms adsorbed solely on-surface [Figs. 5.3(a) and (e)]; (2) structures involving large restructuring/corrugation of the surface [Figs. 5.3(b)–(d) and (f), Fig. 5.5, Fig. 5.6(a)–(c)]; and (3) on-surface+subsurface Cl configurations with less corrugated surface than type-2 structures [Figs. 5.4(a)–(c), and Fig. 5.6(d) and (e)].

In general, corrugated type-2 structures are more stable than "flat" type-3. This may be attributed to the following: type-3 structures involve so substantial relaxation of the surface layer, Δd_{12}, that all direct surface-to-subsurface metal bonds are broken (see Figs. 5.4(a)–(c) and Fig. 5.6(d) and (e)). At variance, not all surface-to-subsurface metal bonds are broken when

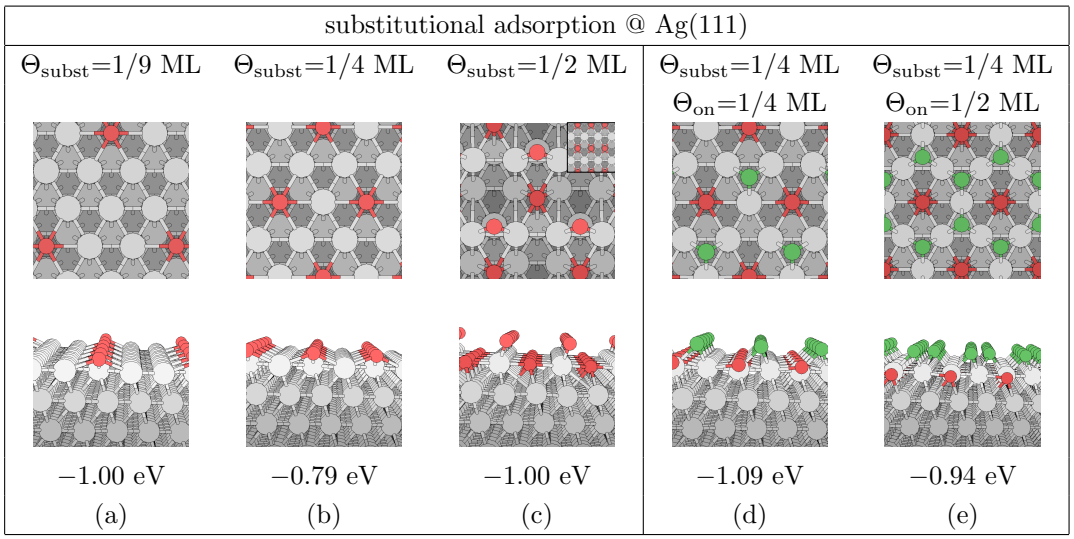

Figure 5.7: *(a–c): Optimized substitutional Cl configurations on Ag(111) at coverages 1/9, 1/4, and 1/2 ML. The inset in (c) shows the corresponding initial structure. (d,e): Optimized mixed on-surface+substitutional Cl adsorption structures on Ag(111) at a total coverage of 1/2 and 3/4 ML. The average substitutional chemisorption energy,* $E_{\text{chem}}^{\text{subst}}$*, is also reported.* Θ_{on} *(*Θ_{subst}*) is the coverage of on-surface (substitutional) Cl. Red spheres: substitutional Cl atoms. Green spheres: on-surface Cl atoms.*

large corrugation of the surface layer takes place, and correspondingly the Δd_{12} relaxation is also substantially smaller. Less stable type-3 structures basically arise under two circumstances, which are both related to symmetry: (i) when the initial structure is chosen such that it does not allow for an easy corrugation, and (ii) when the supercell is too small and the corrugation is not possible due to symmetry constraints.

Although we have studied relatively large set of structures, there may be other mixed on-surface+subsurface more stable configurations wich have been not identified. Nevertheless, as for mixed on-surface+subsurface we believe we have captured the main trends.

Substitutional adsorption. Substitutional adsorption can be seen as adsorption into a vacancy, which is one of the possible surface defects and therefore a realistic adsorption site. Moreover substitutional adsorption can

Θ_{tot} (ML)	Θ_{on} (ML)	Θ_{subst} (ML)	Vacancy-layer	Shown in Fig.	E^{subst}_{chem} (eV)	E^{vac}_{chem} (eV)	Δz^{on}_{Cl-Ag} (Å)	Δz^{subst}_{Cl-Ag} (Å)	d^{on}_{Cl-Ag} (Å)	d^{subst}_{Cl-Ag} (Å)	h_{Ag} (Å)	Δd_{12} (%)
1/9	0	1/9	1st	5.7(a)	**−1.00**	−1.54	-	0.95	-	3.10	0.05	−1.36
			2nd	-	0.17	−0.36	-	−2.50	-	2.94	0.12	1.0
1/4	0	1/4	1st	5.7(b)	**−0.79**	−1.38	-	1.06	-	3.13	0.00	−3.5
			2nd	-	0.32	−0.27	-	−2.65	-	2.84	0.06	0.8
1/2	0	1/2	1st	5.7(c)	−1.00	−1.44	-	0.95	-	2.66	0.00	−3.6
	1/4	1/4	1st	5.7(d)	**−1.09**	−1.38	1.94	0.47	2.60	2.98	0.00	−1.4
3/4	1/2	1/4	1st	5.7(e)	**−0.94**	−1.14	1.94	−0.11	2.58	2.88	0.00	0.5

Table 5.4: *Substitutional and mixed on-surface+substitutional Cl configurations as a function of coverage, on Ag(111). Chemisorption energy, E^{subst}_{chem}, and gross chemisorption energy on pre-formed vacancies, E^{vac}_{chem}, in eV/Cl-atom, are reported. For each coverage, E^{subst}_{chem} corresponding to the most stable configuration is reported in bold font. Θ_{tot} is the total Cl coverage; Θ_{on} (Θ_{subst}) is the coverage of on-surface (substitutional) Cl. "Vacancy-layer" is the Ag layer containing the vacancies, which is either surface (1st) or subsurface (2nd). Other parametrs are defined at the beginning of section 5.1.1. For pure Ag(111) $\Delta d_{12} = -0.7\%$.*

Θ_{vac} (ML)	$\mathrm{E_f}$ (eV/vac)	$\mathrm{h_{Ag}}$ (Å)	$\Delta\mathrm{d_{12}}$ (%)
1/9	0.54	0.03	−2.0
1/4	0.59	0.00	−3.7
1/2	0.44	0.00	−6.6

Table 5.5: *Vacancy formation energy, E_{f}, as a function of vacancy coverage, Θ_{vac}, on Ag(111). h_{Ag} is the difference in height between the highest and lowest surface Ag atoms. Δd_{12} is the relaxation of the surface layer. For pure Ag(111) $\Delta d_{12} = -0.7\%$.*

be a possible route for incorporation of Cl atoms below the surface. The results about the substitutional Cl adsorption are reported in Tab. 5.4.

The substitutional chemisorption energy, per Cl atom, of n Cl atoms into n vacancy on Ag(111) is given by:

$$E_{\mathrm{chem}}^{\mathrm{subst}} = \frac{1}{n}\left[E_{\mathrm{Cl/vac}} + nE_{\mathrm{bulk}} - E_{\mathrm{slab}} - \frac{n}{2}E_{\mathrm{Cl_2}}\right], \tag{5.2}$$

where $E_{\mathrm{Cl/vac}}$ is the total energy of the substitutional adsorption system, E_{bulk} is the energy of an Ag atom in the bulk, and E_{slab} is the total energy of the slab without the vacancy. This definition of chemisorption energy includes the vacancy formation energy, which is given by:

$$E_{\mathrm{f}} = \frac{1}{n}\left[E_{\mathrm{vac}} + nE_{\mathrm{bulk}} - E_{\mathrm{slab}}\right], \tag{5.3}$$

where E_{vac} is the total energy of the Ag slab with n vacancies. The surface vacancy formation energy has been calculated for different coverages, and values are reported in Tab. 5.5.

In the case of mixed on-surface+substitutional adsorption, the chemisorption energy is calculated as:

$$E_{\mathrm{chem}}^{\mathrm{subst}} = \frac{1}{m}\left[E_{\mathrm{Cl/vac}} + nE_{\mathrm{bulk}} - E_{\mathrm{slab}} - \frac{m}{2}E_{\mathrm{Cl_2}}\right], \tag{5.4}$$

where m is the total number of Cl atoms, and n the number of vacancies and substitutionally adsorbed Cl atoms. Note that $m \geq n$.

We also define the gross chemisorption energy of n Cl atoms into n preformed vacancies as:

$$E_{\mathrm{chem}}^{\mathrm{vac}} = \frac{1}{n}\left[E_{\mathrm{Cl/vac}} - E_{\mathrm{vac}} - \frac{n}{2}E_{\mathrm{Cl_2}}\right]. \tag{5.5}$$

Optimized geometries, corresponding to Cl substitutional adsorption into the surface layer at 1/9 and 1/4 ML, are shown in Figs. 5.7(a) and (b), respectively. Substitutional Cl atoms are represented with red spheres. According to our results, at 1/9 ML the Cl binds similarly to vacancies and fcc sites (E_{chem} is -1.54 eV and -1.58 eV, respectively), This trend is in agreement with the result of Leeuw et al. [33]. At 1/9 and 1/4 ML, we also investigated Cl substitutional adsorption into the second Ag layer, which results to be substantially less stable than that for the surface layer.

At 1/2 ML of substitutional Cl, the initial structure is composed of alternative Cl and Ag rows in the surface layer (see the inset of Fig. 5.7(c)). However, during the structural optimization one Cl atom is pushed toward the bridge site and a honeycomb Cl configuration forms. The average substitutional chemisorption energy is -1.00 eV. At 1/2 ML we also investigated a mixed on-surface+substitutional configuration, where 1/4 ML of Cl is substitutional and the other 1/4 ML is adsorbed on the 2nn fcc sites (Fig. 5.7(d)). The resulting average chemisorption energy is -1.09 eV, and it is very close to the average chemisorption energy of pure on-surface adsorption at this coverage (-1.13 eV). This result suggests that, by increasing Cl coverage, mixed on-surface+substitutional adsorption may become a competitive or even preferred mode of adsorption.

For this reason, we investigated at 3/4 ML a configuration shown in Fig. 5.7(e), which is derived from the most stable on-surface configuration at 1/2 ML (Fig. 5.1(a)) such that the Ag atom in the center of the hexagon is substituted by Cl. This configuration has an average substitutional chemisorption energy of -0.94 eV, and is therefore more stable than the pure on-surface adsorption ($E_{\text{chem}} = -0.75$ eV) and comparable to mixed on-surface+subsurface adsorption ($E_{\text{chem}} = -0.91$ eV). These findings suggest that, at high Cl coverages, substitutional adsorption represent a possible way for Cl atoms to penetrate on the bulk.

5.1.2 Cl adsorption on Ag(210)

The role of surface defects on Cl subsurface adsorption is addressed considering the stepped Ag(210) surface. Step edges are often more reactive than

Θ_{total} (ML)	Θ_{on} (ML)	Θ_{sub} (ML)	Initial Conf.	Final Conf.	E_{chem} (eV)	$\Theta^{\text{f}}_{\text{on}}$ (ML)	$\Theta^{\text{f}}_{\text{sub}}$ (ML)
1/4	1/4	0	A	5.8(a)	**−1.78**	1/4	0
			B	5.8(b)	−1.59	1/4	0
	0	1/4	octa	5.8(c)	−1.51	1/4	0
1/2	1/2	0	A/A	5.9(a)	**−1.69**	1/2	0
			A/B	5.9(b)	−1.61	1/2	0
	1/4	1/4	A/octa	5.9(c)	−1.53	1/2	0
3/4	3/4	0	A/A/B	5.10(a)	**−1.38**	3/4	0
	2/4	1/4	A/A/octa	5.10(b)	−1.37	2/4	1/4
1	1	0	A/A/B/B	5.11(a)	**−1.26**	1/4	3/4
	3/4	1/4	A/A/B/octa	5.11(b)	−1.24	1/4	3/4

Table 5.6: *Cl adsorption configurations as a function of coverage, on Ag(210). Chemisorption energies, E_{chem}, in eV/Cl-atom, are reported. For each coverage, E_{chem} corresponding to the most stable configuration is reported in bold font. Initial Conf. refers to configurations before relaxation. Final Conf. refers to figure where configuration after relaxation is shown. Θ_{total} is the total Cl coverage, calculated as the ratio between total number of Cl atoms and surface Ag atoms. Θ_{on} and Θ_{sub} is the initial coverage of on-surface and subsurface Cl atoms, respectively. $\Theta^{\text{f}}_{\text{on}}$ and $\Theta^{\text{f}}_{\text{sub}}$ is the is the coverage of on-surface and subsurface Cl atoms in the relaxed configuration.*

flat surfaces, due to lower coordination, and for this reason it is interesting to investigate if such defects facilitate Cl subsurface adsorption. In this respect, we choose the Ag(210) surface, which is among the most open and reactive stepped surfaces. In Tab. 5.6 we show the chemisorption energies per Cl atom at different Cl coverages, on Ag(210).

At Cl coverage of 1/4 ML, three possible adsorption sites on Ag(210) have been investigated (for details on Ag(210) surface sites see Appendix A). In Fig. 5.8 we show initial structures (top row) and optimized structures (bottom row). The most stable adsorption site is site A above the steps, Fig. 5.8(a), with a chemisorption energy of −1.78 eV. Cl adsorption above steps results to be more stable than adsorption on fcc sites and on pre-formed

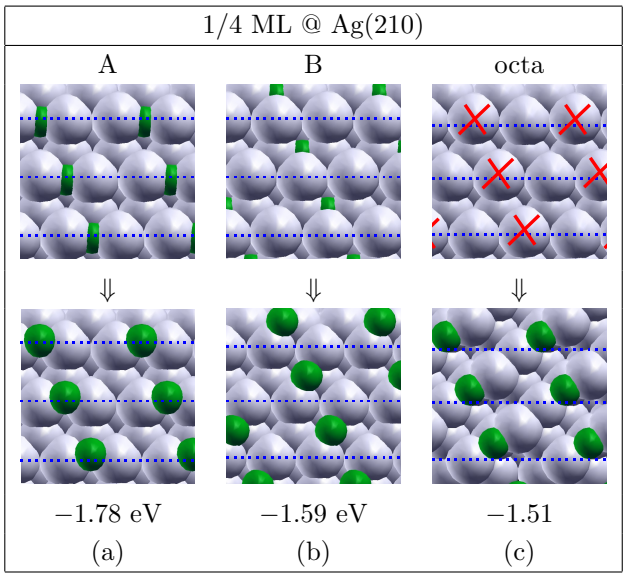

Figure 5.8: *Identified Cl adsorption configurations on Ag(210), with corresponding chemisorption energy, at a total coverage of 1/4 ML. Top row: initial configurations; bottom row: optimized configurations. Blue dashed line indicates step direction. Octa sites are located below Ag atoms marked with red cross (×).*

vacancies. This trend is in agreement with results of de Leeuw et al.[33]. The adsorption in the subsurface octa site (located below Ag atoms marked with red cross (×)) results to be unstable and Cl atom moves on-surface, with a chemisorption energy of −1.51 eV.

At coverage of 1/2 ML, we considered three different initial structures with 1/4 ML of Cl adsorbed always above the step in site A (which is the most stable adsorption site at low coverage). These are the A/A, A/B, and A/octa configurations, shown in Fig. 5.9, top row. Among them, the most stable is the A/A configuration, Fig. 5.9(a), with Cl atoms adsorbed exclusively into A sites, thus fully decorating the step-edge. This configuration has an average-chemisorption energy of −1.69 eV. It is worth to notice that the step-edge decoration, where Cl atoms form the –Ag–Cl–Ag–Cl–Ag– chains, is less stable than the configuration A, Fig. 5.8(a), with "isolated" Cl above the step. This is at variance with chemisorption of oxygen on Ag(210), where the step-edge decoration is a particularly stable configuration [59]. The relaxation of the

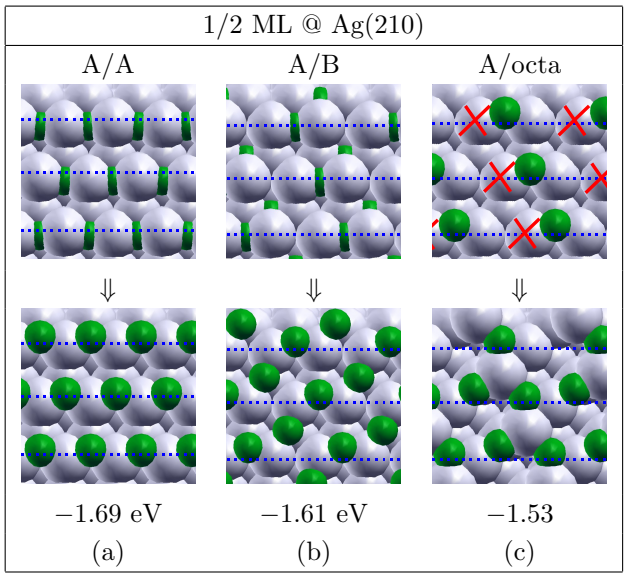

Figure 5.9: *Identified Cl adsorption configurations on Ag(210), with corresponding chemisorption energy, at a total coverage of 1/2 ML. Top row: initial configurations; bottom row: optimized configurations. Blue dashed line indicates step direction. Octa sites are located below Ag atoms marked with red cross (×).*

A/octa structure results in pure on-surface configuration with large surface restructuring (see Fig. 5.9(c)).

Increasing the coverage up to 3/4 ML, we considered two geometries, derived from the most stable A/A configuration at 1/2 ML with and additional Cl atom/supercell either in B or in octa site, Figs. 5.10(a) and (b) top row, respectively. During optimization both configurations change substantially. In particular, in structure of Fig. 5.10(a) all Cl atoms remain on the surface. As for the configuration A/A/octa, the step decoration is perturbed, but the octa Cl atom remains subsurface (blue spheres). The A/A/B and A/A/octa configurations are almost degenerate, with an average chemisorption energy of −1.38 and −1.37 eV, respectively, showing that only at this high coverage mixed on-surface+subsurface adsorption mode becomes competitive with respect to pure on-surface.

Finally, at 1 ML of Cl coverage on Ag(210) we investigated the A/A/B/B and A/A/B/octa configurations, shown in Fig. 5.11(a) and (b) top row, re-

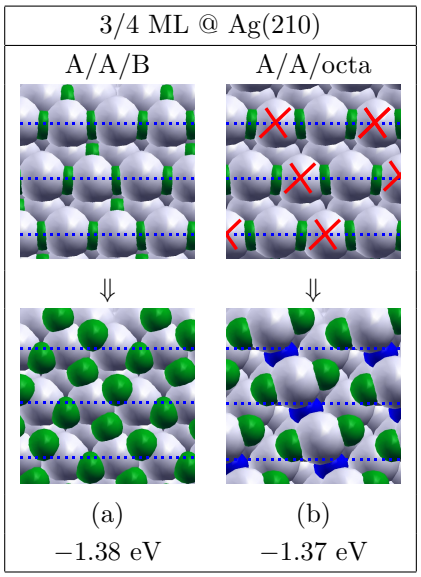

Figure 5.10: *Identified Cl adsorption configurations on Ag(210), with corresponding chemisorption energy, at a total coverage of 3/4 ML. Top row: initial configurations; bottom row: optimized configurations. Blue dashed line indicates step direction. Octa sites are located below Ag atoms marked with red cross (×). Blue spheres: subsurface Cl atoms.*

spectively. Both structures change substantially during optimization, leading both to mixed on-surface+subsurface configurations, with an average chemisorption energy of −1.26 and −1.24 eV, respectively.

In conclusion, according to our results even in presence of very open surface defects, such as Ag(210) step-edges, mixed on-surface+subsurface Cl adsorption becomes competitive with respect to pure on-surface only at high coverages ($\Theta \geq 3/4$ ML), as found for flat Ag(111) surface.

5.2 Does Cl go subsurface on Ag?

In Fig. 5.12 we display the trend of the average chemisorption energy of Cl on Ag(111), as a function of coverage and adsorption type, up to a 3/4 ML of coverage. Only the most stable structures of each adsorption type at a given coverage are considered. According to our results, the adsorption of Cl as a function of coverage can be classified into three regions:

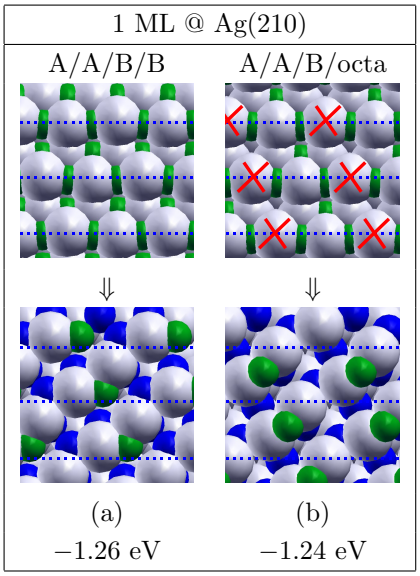

Figure 5.11: *Identified Cl adsorption configurations on Ag(210), with corresponding chemisorption energy, at a total coverage of 1 ML. Top row: initial configurations; bottom row: optimized configurations. Blue dashed line indicates step direction. Octa sites are located below Ag atoms marked with red cross (×). Blue spheres: subsurface Cl atoms.*

(i) $\Theta \leq 1/3$ ML: the on-surface adsorption is the most stable adsorption mode, and it is approximately independent on the coverage;

(ii) $1/3 \leq \Theta \leq 1/2$ ML: the on-surface adsorption mode remains the most stable, but the magnitude of on-surface chemisorption energy decreases with increasing coverage (roughly linearly up to the highest considered coverage), and mixed on-surface+subsurface and substitutional adsorption modes become competitive at coverage about 1/2 ML;

(iii) $\Theta > 1/2$ ML: the mixed adsorption modes become more stable than pure on-surface.

In conclusion, Cl subsurface adsorption mode is stabilized increasing the coverage. In particular, our results show that mixed adsorption (on-surface+subsurface and on-surface+substitutional) becomes the preferred one at Cl coverage between 1/2 and 3/4 ML. Moreover, these findings suggest that substitutional adsorption mode is a possible way for Cl atoms to

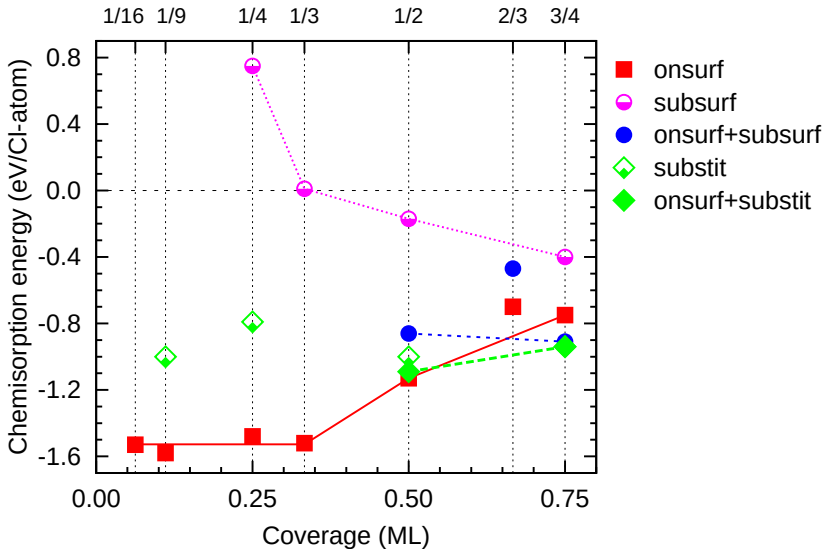

Figure 5.12: *Average chemisorption energy of Cl adsorbed on Ag(111), as a function of coverage and adsorption type. The most stable on-surface, subsurface, mixed on-surface+subsurface, substitutional and mixed on-surface+substitutional adsorption structures are considered (designated as "onsurf", "subsurf", "onsurf+subsurf", "substit", and "onsurf+substit", respectively). Lines in the plot are drawn to guide the eye.*

penetrate subsurface. We also demonstrate that the presence of very open surface defects, such as the Ag(210) stepped surface, does not facilitate Cl subsurface penetration at low Cl coverage.

Our findings on Cl adsorption on Ag(111) surface, indicate that the role of subsurface Cl as promoter in the ethylene epoxidation should be revised. Indeed, the fact that subsurface Cl is present only at high Cl coverages, togheter with experimental results showing zero catalyst activity at high Cl coverage, leads to the conclusion that on-surface Cl, at low coverage, could be the Cl species active as promoter in the ethylene epoxidation. This conclusion is supported by our preliminary results on EO and Ac formation on Ag(111), with 1/4 ML of on-surface Cl, which show an improved selectivity with respect to unpromoted Ag. In particular, on Ag(111) $\Delta E^* = (E^*_{\mathrm{Ac}} - E^*_{\mathrm{EO}})$, which determines the catalyst selectivity at a given temperature, increases from -0.03 to 0.21 eV when 1/4 ML of on-surface Cl is added.

Conclusions

Ethylene epoxidation reaction is one of the most important oxidation processes based on heterogeneous metallic catalysis. The selective product is the ethylene epoxide (EO), which is an important chemical used as intermediate in the production of plastics, while the main undesired product is CO_2. The overall reaction is composed of different elementary steps: dissociative adsorption of oxygen molecules, adsorption of ethylene to form with preadsorbed O an intermediate OxaMetallaCycle (OMC) chemisorbed state, and transformation of the OMC into desired EO or into Acetaldehyde (Ac), which is the path leading to total combustion. In this process, Ag displays unique catalytic properties, with selectivity from 40% for unpromoted Ag surfaces, up to 80% in presence of promoters such as Cs and Cl. Theoretical and experimental studies have also shown that Cu catalysts and Ag/Cu alloys display higher intrinsic selectivity toward EO, as compared to Ag.

Despite the large interest in this chemical reaction, and the many theoretical and experimental studies on the subject, the factors determining the catalyst selectivity toward EO remain understood to a lesser extent.

In this thesis we investigated, using ab-initio methods based on Density Functional Theory (DFT), the EO and Ac formation from the OMC intermediate. Reaction pathways and activation energies for the two competing reactions have been systematically calculated on different metal surfaces, to provide an extensive set of data, whose analysis allowed us to understand the reaction mechanisms operating at atomic level that determine the catalyst selectivity. In particular, in our study we used as model catalysts the (100) and (111) surfaces of IB metals (Cu, Ag, Au) as well as those of the more reactive Rh. Since Cl is a well known promoter in ethylene epoxidation reaction, Cl adsorption on Ag(111) has been also investigated.

The main result of this work comes from a structural analysis of the transition states (TS) leading to EO and Ac formation from the OMC intermediate. In particular, we noticed that in the TS for the EO formation only the OMC's C–surface bond is broken, while during Ac formation both C– and O–surface bonds are partially broken. These characteristics result to be general, since we observed them for all the TS on the different metal surfaces considered in this work.

The above observation, allowed us to introduce the concept of differential bonding affinity of the catalyst toward the C– and O–atom in the OMC. Indeed, depending on the strenght of the OMC's C–surface bond with respect to its O–surface bond, the preference of the catalyst to transform the OMC into EO or Ac will be determined. In particular, we claim that the stronger is the O–surface bond with respect to the C–surface one in the OMC–surface interaction, the higher will be the activation energy for Ac formation with respect to the one for EO, thus improving the catalyst selectivity.

In order to make this analysis more quantitative, first of all we proposed a simple approximation for the OMC's C– and O–surface bond strenght. In particular, we used methyl (CH_3) and methoxy (CH_3O) to represent the C– and O– fragments in the OMC, respectively. Then, the OMC's C– and O–surface bond strenght has been approximated by the adsorption energy of CH_3 ($E_{\mathrm{ads}}^{\mathrm{CH_3}}$) and CH_3O ($E_{\mathrm{ads}}^{\mathrm{CH_3O}}$), respectively.

The introduction of the above quantities led us to the next step, that is the description of the activation energies for Ac and EO formation from the OMC, in terms of methyl and methoxy adsorption energies, in addition to a standard Brønsted-Evans-Polanyi (BEP) term, proportional to the energy of products. In particular, we found that both $E_{\mathrm{ads}}^{\mathrm{CH_3}}$ and $E_{\mathrm{ads}}^{\mathrm{CH_3O}}$ contribute to the energy of the TS leading to Ac formation. Indeed, according to our model, they represent the OMC's C– and O–surface bonds which are only partially broken in the TS leading to Ac. On the contrary, only $E_{\mathrm{ads}}^{\mathrm{CH_3O}}$ term contributes to the energy of the TS for EO formation, where the C–surface bond is fully broken and only the O–surface bond is present. As a result of multi-parameter fits for the activation energies for Ac and EO formation, which we have calculated on different metal surfaces, we show that our model provide a substantial improvement, with respect to the BEP term alone, in

describing the Ac and EO formation from the OMC.

Once a good description of Ac and EO activation energies has been achieved, we proceeded to the study of the catalyst selectivity, which depends, at fixed temperature, on the difference between Ac and EO activation energies, $\Delta E^* = E^*_{\rm Ac} - E^*_{\rm EO}$. Using the expression for $E^*_{\rm Ac}$ and $E^*_{\rm EO}$ we got on the basis of our model, we found that the differential bonding affinity of the catalyst toward the C– and O–atom in the OMC structure gives an important contribution in describing selectivity. In particular, we propose a simple indicator for the catalyst selectivity, where:

$$\Delta E^* \propto \left(E^{CH_3}_{ads} - E^{CH_3O}_{ads}\right) + \left(E^{Ac}_{ads} - E^{EO}_{ads}\right). \tag{5.6}$$

The second term in eq. (5.6) represents the BEP contribution, where $E^{\rm Ac(EO)}_{\rm ads}$ is the adsorption energy of Ac (EO) on the surface. Instead, the first term accounts for our predicted C– *vs.* O–surface bond strenght contribution to the selectivity. This term is important to explain selectivity. Indeed, we can show that the higher selectivity in the ethylene epoxidation reaction of Cu surface and Ag/Cu alloy with respect to pure Ag, can be explained precisely in terms of the higher affinity of Cu toward the O atom in the OMC, with respect to the C one.

The main result of this work, represented by eq. (5.6), has two important consequences: (1) the indicator we propose, whose evaluation requires resonable computational effort, provides a useful tool for the rational search of more selective catalysts; (2) our indicator is based on the new concept of differential bonding affinity of a catalyst toward different atoms in the OMC structure, and we demonstrated that it has an important role in explaining the observed improved selectivity of Cu and Cu/Ag alloys in ethylene epoxidation. We believe that this concept is not limited to the ethylene epoxidation reaction, but it can provide basic understanding of catalyst selectivity also in other branching reactions.

Appendix A

Computational details

All calculations are performed in the framework of Density-Functional Theory, as implemented in the `Quantum ESPRESSO` distribution [56] using the generalized gradient approximation of Perdew-Burke-Ernzerhof [48]. We used the pseudopotential method with ultrasoft pseudopotentials [52, 67]. Kohn-Sham orbitals were expanded in a plane-wave basis set up to a kinetic energy E_{cut} of 27 Ry (216 Ry for the charge-density energy E_{cutrho}).

Metal surfaces have been modeled by periodically repeated slabs. In particular, results about the formation of OMC, EO and Ac on perfect Ag(100) surfaces, presented in chapter 3, have been obtained using slabs consisting of five layers, with molecules adsorbed on both sides (Fig. A.1(a)), and relaxing all degrees of freedom. The same calculations have been also performed using three layers slabs, with molecules adsorbed on one side (Fig. A.1(b)), keeping bottom layer fixed to the bulk position, and optimizing all the other degrees of freedom. A comparison between results obtained using the two different surface models displays small energy differences. For this reason, all others results on (100) and (111) metal surfaces presented in chapter 3 have been obtained using three layers slabs, which results to be computationally less expensive.

Results about the formation of OMC, EO and Ac on stepped Ag(210) surfaces, presented in chapter 3, have been obtained using slabs consisting of fortheen layers, with molecules adsorbed on both sides, and relaxing all degrees of freedom. Even for this surface, calculations have been repeated us-

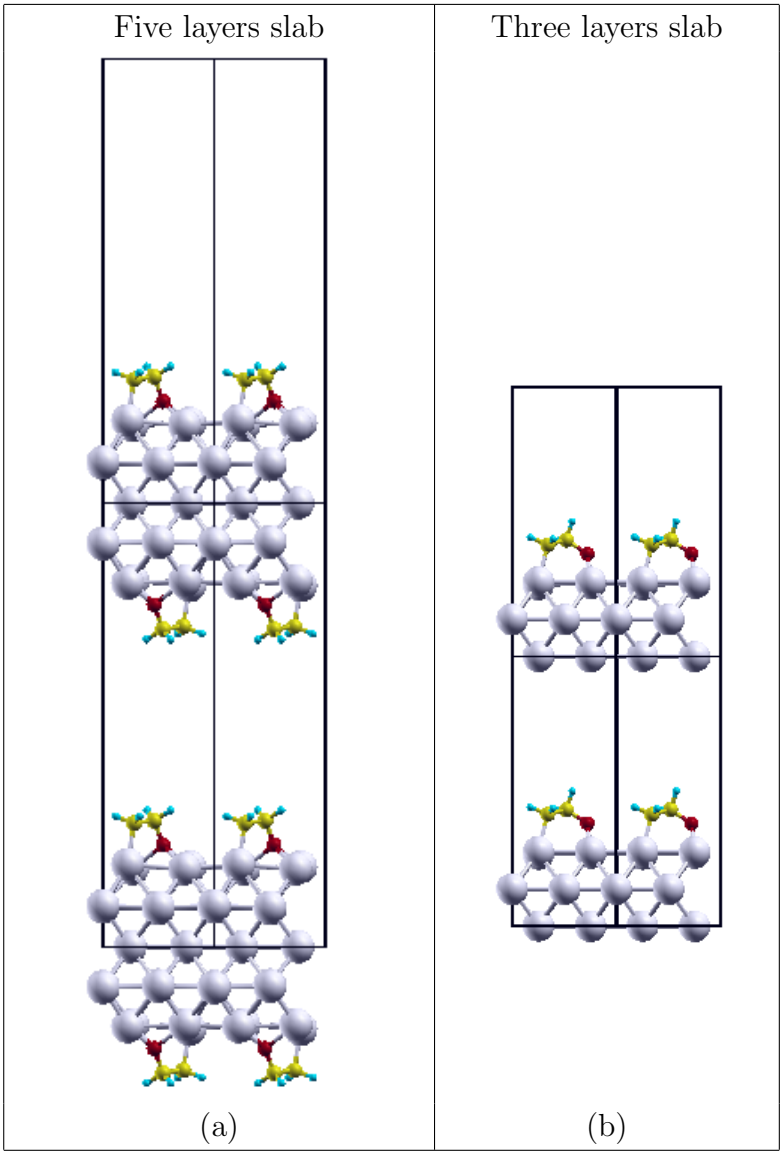

Figure A.1: *Example of periodically repeated slab: (a) OMC on Ag(100)-(2 × 2) surface, modeled with five layers slab and molecules adsorbed on both sides; (b) OMC Ag(100)-(2 × 2) surface, modeled with three layers slab and molecules adsorbed on one side.*

ing seven layers slabs, one side adsorption, fixing the two bottom layers, and optimizing all other degrees of freedom. Again, small energy diferences are obtained, and for computational efficiency, all other calculations on Ag(210) presented in this work have been performed using seven layers slabs.

Cl adsorption on Ag(111), presented in chapter 5, has been performed modeling Ag surfaces with four layers slabs, one side adsorption and bottom layer fixed to bulk position. Four layers instead of three layers slabs are needed since subsurface Cl adsorption is investigated. Dipole correction, to cancel out the fictitious dipole created perpendicular to the surface, is checked. The energy difference between calculations with and without dipole correction is small. For this reason we performed all calculations about Cl adsorption on Ag(111) without dipole correction, which results to be computationally less expensive.

Since several configurations of Cl on Ag surfaces at various coverages are investigated, in order to facilitate the discussion, in Fig. A.2 we show different supercells and sites used for modeling the adsorption of Cl on Ag(111) (a) and Ag(210) (b). In particular, as for (111) surface, for 1/16 ML we used (4×4) supercell (Fig. A.2 (a), red line), whereas 1/4, 1/2, and 3/4 ML were modeled by (2×2) supercell (Fig. A.2 (a), blue line). For 1/3 and 2/3 ML we used ($\sqrt{3}\times\sqrt{3}R30°$) supercell (Fig. A.2 (a), black line). On-surface and subsurface adsorption sites are also shown in Fig. A.2 (a) (therein the lateral position of the sites above and below the surface is labeled as *on-surface*|*subsurface*). There are four different on-surface adsorption sites: fcc, hcp, bridge, and top. As for the adsorption below the top Ag(111) layer, we considered Cl atoms adsorbed into octahedral (labelled as octa) and two tetrahedral sites, labelled as tetra–1 and tetra–2. The octa site is located below an fcc site between the surface and the first subsurface layer. Analogously, the tetra–1 site is located below an hcp site, whereas the tetra–2 site is located beneath the surface Ag atom and above three Ag atoms of the first subsurface layer.

On Ag(210), all calculations were done using (2×1) supercell (Fig. A.2 (b), yellow line). In particular, we considered three different sites: site A located just above the step (coordinated by three Ag atoms), site B located below the step (this is the four-fold hollow site on the terrace), and octa site located below the step Ag atom.

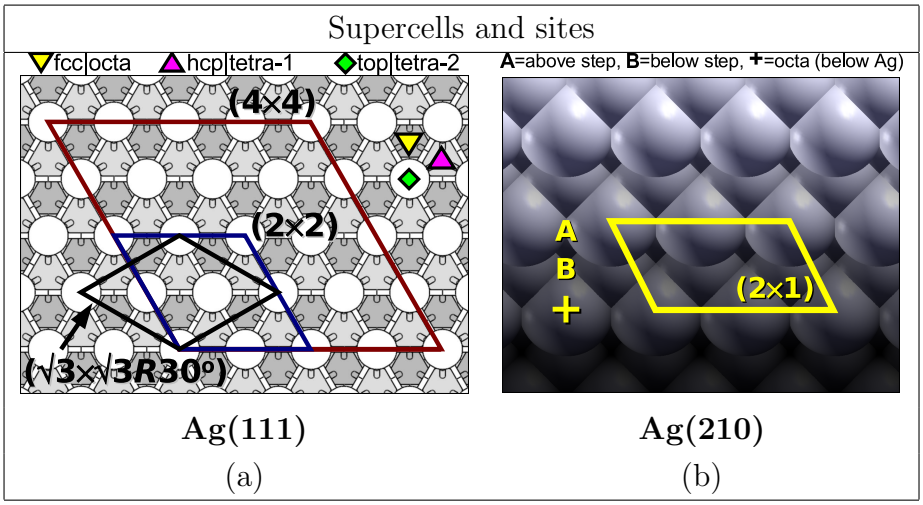

Figure A.2: *Representation of different supercells and sites used in this work for modeling the adsorption on Ag(111) (a) and Ag(210) (b) surfaces: Ag(111) has been modeled by (4×4), (2×2), and* $(\sqrt{3} \times \sqrt{3})R30°$ *supercells that are drawn with red, blue, and black lines, respectively, whereas (2×1) supercell was used for Ag(210). Sites on Ag(111): yellow triangle – lateral position of fcc and the subsurface octahedral (octa) site beneath it (labeled as fcc|octa). Two different tehtrahedral sites are labeled as tetra–1 and tetra–2. Tetra–1 is located beneath the hcp site (magenta triangle, hcp|tetra–1) and tetra–2 is located beneath the surface Ag atom (green diamond, top|tetra–2). Sites on Ag(210): A – above the step, B – below the step, and the octa site located beneath the step Ag atom (marked by +).*

All structures are relaxed until forces on atoms are less than 0.02 eV/Å. The thickness of vacuum region (i.e. the distance along z direction between molecules and the adjacent slab) is set to be 10 Å or more. The in-plane lattice spacing in surface calculations was determined from the calculated equilibrium bulk lattice parameter, which is 3.86, 3.67, 4.16, and 4.17 Å for Rh, Cu, Ag, and Au, respectively.

When calculating average value of a function f in the Brillouin Zone (BZ), a sum over a finite number N_k of k points is done:

$$\bar{f} = \sum_{i=1}^{N_{\mathbf{k}}} w_{\mathbf{k}_i}\, \theta(\epsilon_F - \epsilon(\mathbf{k}_i))\; f(\mathbf{k}_i) \tag{A.1}$$

where ϵ_F is the Fermi energy, $w_{\mathbf{k}_i}$ is the weight of the k points in the Brillouin zone, and $\theta(x)$ is the step-function ($\theta(x) = 0$ if $x < 0$ and $\theta(x) = 1$ if $x \geq 0$). Electronic structure calculations for metals show a certain numerical instability in the self-consistent calculations. This is due to the fact that for small variations in $\epsilon(\mathbf{k}_i)$ or ϵ_F a certain k point can move across the Fermi surface, producing variations in the $\bar{f}$. To avoid this problem, BZ integrations have been performed with the Gaussian-smearing special-point technique [68], where the step-function $\theta(x)$ is replaced by a continuos function $\bar{\theta}(\sigma, x)$, which is written as an integral of a gaussian function (possibly multiplied by a polinomial function) whose amplitude is determined by the parameter σ (smearing). In the limit of $\sigma \rightarrow 0$, $\bar{\theta}(\sigma, x)$ reproduces the step-function $\theta(x)$. In this work we used the $\bar{\theta}(\sigma, x)$ function as proposed by Methfessel and Paxton [69]. The convergence of calculations can be tested varying the value of σ. Usually for high values of σ, few $\mathbf{k}$ points are needed for convergence, but low accuracy is obtained for the results. Decreasing the value of σ, results are closer to the correct one, but a higher number of $\mathbf{k}$ points is needed.

All results presented in this work are obtained using a smearing parameter of 0.03 Ry. As for the Ag(111) surface, for (2×2), $(\sqrt{3} \times \sqrt{3}R30°)$, (2×3), (4×3) and (4×4) supercells the BZ integrations were performed using $(4 \times 4 \times 1)$, $(4 \times 4 \times 1)$, $(4 \times 3 \times 1)$, $(2 \times 3 \times 1)$ and $(2 \times 2 \times 1)$ uniform shifted k-points mesh, respectively. For the stepped Ag(210) surface, a (2×1) supercell is used with a $(4 \times 7 \times 1)$ uniform shifted k-points mesh.

Transition states have been located as the configurations of largest energy along the minimum-energy paths (MEP) connecting the reactants with the products. MEP's have been identified using the climbing-image nudged-elastic band (CI-NEB) method [54, 55], described in chapter 2, whereas the precise location of the TS therein has been validated by verifying that the magnitude of the atomic forces was below a threshold of 50 meV/Å. Several paths have been guessed for each of the reactions discussed in this paper, based on our chemical intuition. Some of them would converge to the same MEP. For those which do not, we report and discuss the MEP corresponding to the minimum calculated activation energy.

All molecular graphics shown in this thesis were produced by the `XCRYSDEN`

graphical package [70].

Appendix B

Overview of other works by the author

The work presented in this thesis is the subject of three papers (one accepted for publication on Journal of Physical Chemistry C, one in revision, one in preparation). This Appendix will give a short presentation of other works that I contributed to as a Ph. D. student at S.I.S.S.A./I.S.A.S.

Direct methane-to-methanol conversion: insight from first-principles
Guido Fratesi, Paola Gava and Stefano de Gironcoli;
accepted for publication in Journal of Physical Chemistry C.
Abstract:
A simple direct mechanism for methane to methanol conversion has been investigated by first-principles on a series of oxygen precovered transition metal surfaces. Energy barriers and reaction paths have been determined, by the CI-NEB algorithm, for three competing elementary processes: 1) methanol formation from methane and oxygen; 2) dehydrogenation of methane to form methyl and hydrogen; 3) dehydrogenation of methane assisted by oxygen, to form methyl and hydroxil radical. Indicators of reactivity towards each elementary step have been identified, providing significant insight for a rational search for a suitable catalyst. Based on this analysis, we suggest that upon suitable conditions, O-dosed Ag surfaces could display considerable reactivity toward direct methane to methanol conversion.

Further steps toward low temperature methane-to-methanol synthesis on transition metal surfaces

Paola Gava and Stefano de Gironcoli;

in preparation.

Abstract:

According to the results obtained for the direct methane-to-methanol conversion, O precovered Ag surfaces, upon suitable O coverage conditions, can favor the direct formation of methanol with respect to methane dehydrogenation assisted by oxygen. Nevertheless, on O-dosed Ag surface methanol results to be unstable, since O assisted dehydrogenation to form methoxy has a very low activation energy (0.21 eV), and methoxy dehydrogenation to formaldehyde is almost barrier-less and highly exothermic. Therefore, Ag surfaces under high O coverage conditions do not represent a good candidate as catalyst for the direct methanol formation, and low O coverage conditions result to be necessary. In this context, in addition to the search of a better catalyst for the direct methanol synthesis, one can also investigate the methanol formation via a multi-steps reaction. For that reason, activation energies and reaction pathways have been investigated for different competing reactions on Rh, Pd, and Ag(111) surfaces. In particular, the following reactions have been considered: 1) methanol formation from methyl and hydroxil radical; 2) methyl dehydrogenation, and its dehydrogenation assisted by O or OH; 3) methoxy formation from methyl and O; 4) methoxy dehydrogenation assisted by O to form formaldehyde; 5) methanol formation from methoxy and hydrogen. From an analysis of the TSs of each reaction step on the considered metal surfaces, we try to understand the reaction mechanisms and factors which determine the surface selectivity toward different products. Indicators for activation energies of the different steps are also identified, to facilitate the search of a suitable catalyst for the multi-steps methanol synthesis.

Bibliography

[1] J. G. Serafin, A. C. Liu, and S. R. Seyedmonir. Surface science and the silver-catalyzed epoxidation of ethylene: an industrial perspective. *Journal of Molecular Catalysis A*, 131:157, 1998.

[2] R. A. van Santen. *in Handbook of Heterogeneous Catalysis*, volume 5, chapter 4.6.1–Epoxidation Catalysis Using Heterogeneous Catalysts, pages 2244–2252. Wilet-VCH, Weinheim, Germany, 1997.

[3] P. Hohenberg and W. Kohn. Inhomogeneous electron gas. *Physcal Review*, 136:B864, 1964.

[4] W. Kohn and L. Sham. Self-consistent equations including exchange and correlation effects. *Physcal Review*, 140:A1133, 1965.

[5] W. X. Li, C. Stampfl, and M. Scheffler. Insight into the function of silver as an oxidation catalyst by ab initio atomistic thermodynamics. *Physical Review B*, 68:165412, 2003.

[6] W. X. Li, C. Stampfl, and M. Scheffler. Why is a noble metal catalytically active? The role of the O-Ag interaction in the function of silver as an oxidation catalyst. *Physical Review Letters*, 90(25):256102, 2003.

[7] J. Schnadt, A. Michaelides, J. Knudsen, R. T. Vang, K. Reuter, E. Laegsgaard, M. Scheffler, and F. Besenbacher. Revisiting the structure of the p(4 x 4) surface oxide on Ag(111). *Physical Review Letters*, 96(14):146101, 2006.

[8] M. Schmid, A. Reicho, A. Stierle, I. Costina, J. Klikovits, P. Kostelnik, O. Dubay, G. Kresse, J. Gustafson, E. Lundgren, J. N. Andersen,

H. Dosch, and P. Varga. Structure of Ag(111)-p(4 x 4)-O: No silver oxide. *Physical Review Letters*, 96(14):146102, 2006.

[9] B. Hammer and J. K. Norskov. Theoretical surface science and catalysis–calculations and concepts. *Advances in Catalysis*, 45:71, 2000.

[10] B. Hammer and J. K. Norskov. Electronic factors determining the reactivity of metal surfaces. *Surface Science*, 343:211, 1995.

[11] G. S. Hammond. A correlation of reaction rates. *Journal of American Chemical Society*, 77:334, 1955.

[12] V. I. Bukhtiyarov, A. I. Nizoskii, H. Bluhm, M. Hävecker, E. Kleimenov, A. Knop-Gericke, and R. Schlögl. Combined in situ XPS and PTRMS study of ethylene epoxidation over silver. *Journal of Catalysis*, 238:260, 2003.

[13] R. B. Grant and R. M. Lambert. A single crystal study of the silver-catalysed selective oxidation and total oxidation of ethylene. *Journal of Catalysis*, 92:364, 1985.

[14] P. J. van de Hoek, E. J. Baerends, and R. A. van Santen. Ethylene epoxidation on Ag(110): the role of subsurface oxygen. *Journal of Physical Chemistry*, 93:6469, 1989.

[15] W. X. Li, C. Stampfl, and M. Scheffler. Subsurface oxygen and surface oxide formation at Ag(111). *Physical Review B*, 67:045408, 2003.

[16] Y. Xu, J. Greeley, and M. Mavrikakis. Effect os subsurface oxygen on the reactivity of the Ag(111) surface. *Journal of American Chemical Society*, 127:12823, 2005.

[17] A. Kokalj, A. Dal Corso, S. de Gironcoli, and S. Baroni. Co-adsorption of ethylene and oxygen on the Ag(001) surface. *Surface Science*, 532-535:191, 2003.

[18] A. Kokalj, A. Dal Corso, S. de Gironcoli, and S. Baroni. DFT study of a weakly π-bonded C_2H_4 on oxygen -covered Ag(100). *Journal of Physical Chemistry B*, 110:367, 2006.

[19] G. S. Jones, M. Mavrikakis, and M. A. Barteau J. M. Vhos. First synthesis, experimental and theoretical vibrational spectra of an oxametallacycle on a metal surface. *Journal of American Chemical Society*, 120:3196, 1998.

[20] J. W. Medlin, M. A. Barteau, and J. M. Vohs. Oxametallacycle formation via ring-opening of 1-epoxy-3-butene on Ag(110): a combined experimental/theoretical approach. *Journal of Molecular Catalysis A*, 163:129, 2000.

[21] S. Linic, J. W. Medlin, and M. A. Barteau. Synthesis of oxametallacycles from 2-Iodoethanol on Ag(111) and the structure dependence of their reactivity. *Langmuir*, 18:5197, 2002.

[22] A. Klust and R. J. Madix. Partial oxidation of higher olefins on Ag(111): Conversion of styrene to styrene oxide, benzene, and benzoic acid. *Surface Science*, 600:2025, 2006.

[23] M. Mavrikakis, D. J. Doren, and M. A. Barteau. Density functional theory calculations for simple oxametallacycles: Trends across the periodic table. *Journal of Physical Chemistry B*, 102:294–399, 1998.

[24] S. Linic and M. A. Barteau. Construction of a reaction coordinate and a microkinetic model for ethylene epoxidation on silver from DFT calculations and surface science experiments. *Journal of Catalysis*, 214:200–212, 2003.

[25] S. Linic and M. A. Barteau. Control of ethylene epoxidation selectivity by surface oxametallacycles. *Journal of American Chemical Society*, 125:4034, 2003.

[26] M. L. Bocquet, A. Michaelides, D. Loffreda, P. Sautet, A. Alavi, and D. A. King. New insights into ethene epoxidation on two oxidized Ag{111} surfaces. *Journal of American Chemical Society*, 125:5620, 2003.

[27] M. L. Bocquet and D. Loffreda. Ethene epoxidation selectivity inhibited by twisted oxametallacycle: A DFT study on Ag surface-oxide. *Journal of American Chemical Society*, 127:17207–17215, 2005.

[28] S. Linic and M. A. Barteau. Formation of a stable surface oxametallacycle that produces ethylene oxide. *Journal of American Chemical Society*, 124:310, 2002.

[29] S. Linic, H. Piao, K. Adib, and M. A. Barteau. Ethylene epoxidation on Ag: Identification of the crucial surface intermediate by experimental and theoretical investigation of its electronic structure. *Angewandte Chemie International Edition*, 43:2918, 2004.

[30] C. T. Campbell and M. T. Paffett. The role of chlorine promotrs in catalytic ethylene epoxidation over the Ag(110) surface. *Applications of Surface Science*, 19:28, 1984.

[31] S. Linic and M. A. Barteau. On the mechanism of Cs promotion in ethylene epoxidation on Ag. *Journal of American Chemical Society*, 126:8086, 2004.

[32] K. Doll and N. M. Harrison. Theoretical study of chlorine adsorption on the ag(111) surface. *Physical Review B*, 63(16):165410, Apr 2001.

[33] N. H. de Leeuw, C. J. Nelson, C. R. A. Catlow, P. Sautet, and W. Dong. Density-functional theory calculations of the adsorption of Cl at perfect and defective Ag(111) surfaces. *Physical Review B*, 69:045419, 2004.

[34] G. M. Lamble, R. S. Brooks, S. Ferrer, and D. A. King. Surface structural determination for a weakly ordered and disordered phase of Cl on Ag(111). *Physical Review B*, 34:2975, 1986.

[35] A. G. Shard and V. R. Dhanak. Chlorine adsorption on silver (111) at low temperatures. *Journal of Physical Chemistry B*, 104:2743, 2000.

[36] E. R. Frank and R. J. Hamers. Chlorine-induced resctructuring of Ag(111) films observed by scanning tunneling microscopy. *Journal of Catalysis*, 172:406, 1997.

[37] H. Piao, K. Adib, and M. A. Barteau. A temperature-programmed X-ray photoelectron spectroscopy (TPXPS) study of chlorine adsorption and diffusion on Ag(111). *Surface Science*, 557:13, 2004.

[38] M. Atkins, J. Couves, M. Hague, B. H. Sakakini, and K. C. Waugh. On the role of Cs, Cl and subsurface O in promoting selectivity in $Ag/\alpha - Al_2O_3$ catalysed oxidation of ethene to ethene epoxide. *Journal of Catalysis*, 235:103, 2005.

[39] J. J. Cowell, A. K. Santra, R. Lindsay, R. M. Lambert, A. Baraldi, and A. Goldoni. Bonding and reactivity of styrene on Cu(110): heterogenous alkene epoxidation without the use of silver. *Surface Science*, 437:1, 1999.

[40] A. K. Santra, J. J. Cowell, and R. M. Lambert. Ultra-selective epoxidation of styrene on pure Cu{111} and the effects of Cs promotion. *Catalysis Letters*, 67:87, 2000.

[41] R. L. Cropley, F. J. Williams, O. P. H. Vaughan, A. J. Urquhart, M. S. Tikhov, and R. M. Lambert. Copper is highly effective for the epoxidation of a "difficult" alkene, whereas silver is not. *Surface Science*, 578:L85, 2005.

[42] D. Torres, N. Lopez, F. Illas, and R. M. Lambert. Low-basicity oxygen atoms: a key in the search for propylene epoxidation catalysts. *Angewandte Chemie International Edition*, 46:2055, 2007.

[43] D. Torres, N. Lopez, F. Illas, and R. M. Lambert. Why copper is intrinsically more selective than silver in alkene epoxidation: Ethylene oxidation on Cu(111) versus Ag(111). *Journal of American Chemical Society*, 127:10774, 2005.

[44] D. Torres, N. Lopez, and F. Illas. A theoretical study of coverage effects for ethylene epoxidation on Cu(111) under low oxygen pressure. *Journal of Catalysis*, 243:404, 2006.

[45] S. Linic, J. Jankowiak, and M. A. Barteau. Selectivity driven design of bimetallic ethylene epoxidation catalysts from first principles. *Journal of Catalysis*, 224:489, 2004.

[46] J. T. Jankowiak and M. A. Barteau. Ethylene epoxidation over silver and copper-silver bimetallic catalysts: I. Kinetics and selectivity. *Journal of Catalysis*, 236:366, 2005.

[47] J. T. Jankowiak and M. A. Barteau. Ethylene epoxidation over silver and copper-silver bimetallic catalysts: II. Cs and Cl promotion. *Journal of Catalysis*, 236:379, 2005.

[48] J. P. Perdew, K. Burke, and M. Ernzerhof. Generalized gradient approximation made simple. *Physical Review Letters*, 77:3865, 1996.

[49] D. R. Hamann, M. Sclüter, and C. Chiang. Norm conserving pseudopotentials. *Physical Review Letters*, 43:1494, 1979.

[50] G. B. Bachelet, D. R. Hamann, and M. Sclüter. Pseudopotentials that work: from H to Pu. *Physical Review B*, 26:4199, 1982.

[51] L. Kleinman and D. M. Bylander. Efficacious form for model pseudopotentials. *Physical Review Letters*, 48:1425, 1982.

[52] D. Vanderbilt. Soft self-consistent pseudopotentials in a generalized eigenvalue formalism. *Physical Review B*, 41:7892, 1990.

[53] C. Sbraccia. *Computer simulation of thermally activated processes*. PhD thesis, S.I.S.S.A./I.S.A.S., February 2005, available on-line at http://www.sissa.it/cm.

[54] H. Johnsson, G. Mills, and K. W. Jacobsen. Nudged elastic band method for finding minimum energy paths of transitions. In B. J. Berne, G. Ciccotti, and D. F. Coker, editors, *Classical and quantum dynamics in condensed phase simulations*, chapter 16, pages 385–404. World Scientific, Singapore, 1998.

[55] G. Henkelman, B. P. Uberuaga, and H. Jónsson. A climbing image nudged elastic band method for finding saddle points and minimum energy paths. *Journal of Chemical Physics*, 113:9901, 2000.

[56] S. Baroni, A. Dal Corso, S. de Gironcoli, P. Giannozzi, C. Cavazzoni, G. Ballabio, S. Scandolo, G. Chiarotti, P. Focher, A. Pasquarello, K. Laasonen, A. Trave, R. Car, N. Marzari, and A. Kokalj. Quantum espresso: open-source package for research in electronic structure, simulation, and optimization. http://www.quantum-espresso.org/, 2005.

[57] D. R. Lide. *CRC Handbook of Chemistry and Physics*. CRC Press, Boca Raton, Florida, USA, 74th edition, 1993.

[58] A. Kokalj, P. Gava, S. de Gironcoli, and S. Baroni. Activated adsorption of ethylene on atomic-oxygen covered Ag(100) and Ag(210): a formation of an oxametallacycle. (accepted for publication in Journal of Physical Chemistry C, 2007).

[59] N. Bonini, A. Kokalj, A. Dal Corso, S. de Gironcoli, and S. Baroni. Structure and dynamics of oxygen adsorbed on Ag(100) vicinal surfaces. *Physical Review B*, 69:195401, 2004.

[60] M. Todorova, W. X. Li, M. V. Ganduglia-Pirovan, C. Stampfl, K. Reuter, and M. Scheffler. Role of subsurface oxygen in oxide formation at transition metal surfaces. *Physical Review Letters*, 89(9):096103, 2002.

[61] M. Gajdoš, A. Eichler, and J. Hafner. Ab initio density functional study of O on the Ag(001) surface. *Surface Science*, 531:272, 2003.

[62] A. Kokalj, N. Bonini, A. Dal Corso, S. de Gironcoli, and S. Baroni. On-surface and subsurface adsorption of oxygen on stepped Ag(210) and Ag(410) surfaces. *Surface Science*, 566-568:1107, 2004.

[63] D. Torres and F. Illas. On the performance of Au(111) for Ethylene Epoxidation: A density functional study. *Journal of Physical Chemistry B*, 110:13310, 2006.

[64] S. Rojluechai, S. Chavadej, J. W. Schwank, and V. Meeyoo. Activity of ethylene epoxidation over high surface area alumina support Au-Ag catalysts. *Journal of Chemical Engineering of Japan*, 39:321, 2006.

[65] A. Kokalj, N. Bonini, C. Sbraccia, S. de Gironcoli, and S. Baroni. Engineering the reactivity of metal catalysts: a model study of methane dehydrogenation on Rh(111). *Journal of American Chemical Society*, 126:16732, 2004.

[66] A. Kokalj, N. Bonini, S. de Gironcoli, C. Sbraccia, G. Fratesi, and S. Baroni. Methane dehydrogenation on Rh@Cu(111): A first-principles study of a model catalyst. *Journal of American Chemical Society*, 128:12448, 2006.

[67] Ultrasoft pseudopotentials for H, C, Cu, Ag, Au, Rh, Cl and Cs were taken from the *PWscf Pseudopotential Download Page*: `http://www.pwscf.org/pseudo.htm` (files: `H.pbe-rrkjus.UPF`, `C.pbe-rrkjus.UPF`, `Cu.pbe-d-rrkjus.UPF`, `Ag.pbe-d-rrkjus.UPF`, `Au.pbe-nd-rrkjus.UPF`, `Rh.pbe-nd-rrkjus.UPF`, `Cl.pbe-n-van.UPF` and `Cs.pbe-mt-bw.UPF`). For the oxygen atom the ultrasoft pseudopotentials is from *Physical Review B*, 64:235118, 2001.

[68] H. J. Monkhorst and J. D. Pack. Special points for brillouin zone integrations. *Physical Review B*, 13:5188, 1976.

[69] M. Methfessel and A. T. Paxton. High-precision sempling for brillouin-zone integration in metals. *Physical Review B*, 40:3616, 1989.

[70] A. Kokalj. Computer graphics and graphical user interfaces as tools in simulations of matter at the atomic scale. *Computational Materials Science*, 28:155, 2003. Code available from: http://www.xcrysden.org/.

Acknowledgments

At the end of this manuscript, I want to thank important people who have been around me for these years in Trieste, and not only.

First of all, I thank Lorena, Marina, Radikkio, and all members of SISSA administration, for their efficiency.

Then, thanks to professor Marco Bernasconi for having accepted to be my external examiner, and for having read my thesis.

Thanks to Erio Tosatti, head of the condensed matter sector in SISSA, for having driven me in the right direction. Thanks to Stefano Baroni, for the precious time he dedicated to discuss about my work.

Thanks to my supervisors, Stefano de Gironcoli and Tone Kokalj. I thank them for the knowledges they passed down to me, for the useful and funny discussions @ Elettra about my work, for their patience when I was stressful. But in particular, I thank them for the pleasant working enviroment they have created, which has reinforced my passion for research. And finally, I also thank them for having made me a pretty good meeting organizer...I don't know how many mails I sent to plan our meetings (including Stefano Baroni!), but I think enough to consider me expert in it :)

Thanks to all my collegues, who made my staying in Sissa a special experience. In particular, I thank Guido for scientific discussions, and Adriano, for having been always and immediatly available when I was in trouble with computer.

Thanks to my dear girls Mary, Taty, Alice, Carlotta, and all the others... hoping to find such special feminist-female friends in Paris, to go on with our "all girls meeting" tradition. And hoping to see you soon there. I will miss you a lot.

Special thanks to Chiara and Alisia, my "triestinian family", whose strong

friendship and affection transformed my weekend loneliness into home warmth.

Thanks to Dominique and Francois, for their practical and moral support in these last months. I think I'm very lucky to have met their family.

This PhD is the end of a very long studying journey... lasted something more than 20 years. Along this period, there has been one positive constant, my mother, and I thank her for always having been there. She did half of the work. Thanks also to Remo and Domenico, for their contribution to make me arrive at this point.

Thanks to Patrick, my happy present and future. Trying to be the same for you.

Finally, a kiss to my sweet friends Rudy and Manon.